





**LIBRARY  
Michigan State  
University**

This is to certify that the  
thesis entitled

EXPERIMENTAL DESIGN AND TECHNIQUES FOR  
MEASUREMENT OF CVD DIAMOND FILM THERMAL  
CONDUCTIVITY USING INFRARED THERMOGRAPHY  
presented by

SCOTT ALLEN HERR

has been accepted towards fulfillment  
of the requirements for

MASTERS degree in MECHANICAL ENGINEERING

  
Major professor

Date Oct. 12, 1993

**PLACE IN RETURN BOX to remove this checkout from your record.  
TO AVOID FINES return on or before date due.**

<b>DATE DUE</b>	<b>DATE DUE</b>	<b>DATE DUE</b>
_____	_____	_____
_____	_____	_____
_____	_____	_____
_____	_____	_____
_____	_____	_____
_____	_____	_____
_____	_____	_____

**MSU Is An Affirmative Action/Equal Opportunity Institution**

c:\crl\datadue.pm3-p.1

**EXPERIMENTAL DESIGN AND TECHNIQUES FOR  
MEASUREMENT OF CVD DIAMOND FILM THERMAL  
CONDUCTIVITY USING INFRARED THERMOGRAPHY**

By

Scott Allen Herr

**A Thesis**

Submitted to  
Michigan State University  
in partial fulfillment of the requirements  
for the degree of

**MASTER OF SCIENCE**

Department of Mechanical Engineering

1993

## **ABSTRACT**

### **EXPERIMENTAL DESIGN AND TECHNIQUES FOR MEASUREMENT OF CVD DIAMOND FILM THERMAL CONDUCTIVITY USING INFRARED THERMOGRAPHY**

By

Scott Allen Herr

Experimental design and techniques were developed for the measurement of the thermal conductivity of doped CVD diamond films. Three solutions were derived, one each for one dimensional, two dimensional and radial heat flow. A sensitivity analysis revealed that the radial heat flow model was most sensitive to the measurement of the thermal conductivity. Sample parameters such as characteristic length, thickness of doped diamond and resistivity were chosen from the model to reduce convective effects, obtain the desired temperature rise and minimize the uncertainty in the estimation of the thermal conductivity.

Two diamond film samples were made according to the specifications determined by the analytical analysis. Both samples consisted of doped and nondoped layers on the topside and were chemically etched from the backside, leaving a free standing diamond diaphragm 3 mm in diameter. The thickness of the doped and nondoped films were approximately 5.6  $\mu\text{m}$  and 1.0  $\mu\text{m}$ , respectively, for both samples.

A new experimental setup was designed and constructed. An infrared imaging temperature acquisition system was implemented to improve on the spatial, temporal and mechanical limitations of contact sensors such as thermocouples and resistance thermometers.

Preliminary results for the thermal conductivity of a semiconducting diamond film were obtained from five experiments using the method of least squares to minimize the error between the measured temperatures recorded by the infrared temperature acquisition system and the calculated temperatures determined by the optimal radial heat flow model. The thermal conductivity along with the experimental uncertainty was determined to be  $249 \pm 13$  W/m K.

These are the first reported values for a semiconducting diamond film. The mean value falls within the range reported for undoped diamond films (190-1350 W/m K). The experimental uncertainty for this method (approximately 5%) is also the first to be determined utilizing uncertainties in all measured experimental parameters.

**to my parents Jack and Jan**

# Acknowledgments

I would like to thank my co-advisors, Professor J. V. Beck and Professor J. J. McGrath for their guidance in the present work. I am grateful for the opportunity to learn from their example as both researchers and engineers.

I would like to personally thank Professor J. V. Beck for the opportunities he has extended to me as his research assistant in the Thermal Properties Measurement Laboratory over the past two years. This opportunity has presented several rewarding experiences; one of which was working with Dr. Bertrand Garnier from Laboratoire de Thermocinetique-ISITEM, Nantes, France. Dr. Garnier's creative thinking, meticulous explanations and exceptional experimental talents have been an important influence in my own laboratory techniques.

I would also like to thank Professor C. W. Somerton for his review of the present work. I believe Professor Somerton to be an exceptional teacher and consider the time spent in his classroom to be an accelerated learning experience.

Many thanks go out to Professor M. Aslam and S. Sahli for their expertise in diamond deposition and microstructural fabrication; their help was crucial in designing the optimal diamond semiconductor for our experiments. I wish to also thank C. Mindock for her involvement in the chemical etching process.

A special thanks goes out to my undergraduate advisor and friend Professor H. M. Dixon who's inspiration throughout the years has elevated my understanding of physics

and engineering. Professor Dixon is a most remarkable scientist and educator and I am grateful for his continual interest and involvement in my education.

Last but not least, I want to thank my family for the support and encouragement they have given me throughout my life.

# Table of Contents

<i>List of Tables</i>	x
<i>List of Figures</i>	xi
<i>Nomenclature</i>	xv

## Chapter

<b>1</b>	<b>Introduction</b>	1
	1.1 Objectives	3
<b>2</b>	<b>Background and Literature Review</b>	4
	2.1 CVD Diamond Films	5
	2.2 General Experimental Methods Determining Thermal Properties	8
	2.3 Special Experimental Methods for CVD Diamond Films	9
<b>3</b>	<b>Problem Description</b>	21
	3.1 Mathematical Modeling	21
	3.1.1 One Dimensional Heat Conduction Model	25
	3.1.2 Two Dimensional Heat Conduction Model	28
	3.1.3 Radial Heat Conduction Model	32

<b>4</b>	<b>Design of the Diamond Film Sample</b>	<b>35</b>
4.1	Determining the Best Experimental Model	36
4.2	Special Requirements for the Desired Temperature Rise	50
4.2.1	Volumetric Heat Generation in Diamond	50
4.2.2	Doping Requirements for the Diamond Film	52
4.3	Limiting Natural Convection	56
4.4	Analytical Results	61
4.5	Topside Sample Fabrication	63
4.6	Bottomside Sample Fabrication	69
<b>5</b>	<b>Experimental Techniques</b>	<b>73</b>
5.1	The Data Acquisition System	73
5.1.1	The Inframetrics Model 600L IR Imaging Radiometer	74
5.1.2	Thermal Image Processing System	77
5.1.3	The Omega 880 Digital Multimeter	78
5.2	System Calibration Check	79
5.3	Experimental Setup	84
5.3.1	Preparation of the Sample Setup	84
<b>6</b>	<b>Procedures and Results for One Dimensional Radial Experiments</b>	<b>86</b>
6.1	Determining the Emissivity	86
6.2	Measuring the Electrical Power	89
6.3	Radiometer Settings	91

6.4	Surface Temperature Measurements	93
6.4.1	Capturing Images Using the Thermal Image Processor	93
6.4.2	Temperature Acquisition	98
6.5	Measurement of the Thermal Conductivity	98
6.5.1	The Simplified Experimental Model	99
6.5.2	Estimation of the Thermal Conductivity	100
6.6	Experimental Uncertainty	111
<b>7</b>	<b>Summary and Conclusions</b>	<b>115</b>
	<i>Suggestions for future work</i>	118
	<b>List of References</b>	<b>120</b>
	<b>Appendices</b>	<b>123</b>
Appendix A	Calibration of the Inframetrics 600L Radiometer for Rapid Transient Thermal Events	123
Appendix B	Temperature Distribution for Experiments 1-5	132
Appendix C	Program NLIN	137
Appendix D	NLIN Output File for Experiment #5	143

## **List of Tables**

<b>Table 2.1:</b>	<b>Thermal conductivity of diamond film evaluated at different thicknesses at room temperature (Morelli et al., 1988).</b>	<b>11</b>
<b>Table 2.2:</b>	<b>Thermal conductivity parallel to the film surface as a function of film thickness (Graebner et al., 1992).</b>	<b>14</b>
<b>Table 4.1:</b>	<b>Optimum sample design parameters assuming a thermal conductivity of 1000 W/m K.</b>	<b>62</b>
<b>Table 6.1:</b>	<b>Temperature vs. resistance for sample A.</b>	<b>90</b>
<b>Table 6.2:</b>	<b>The thermal conductivity estimated by NLIN for each of the five experiments at different power levels.</b>	<b>110</b>
<b>Table 6.3:</b>	<b>Experimental parameters, their uncertainties and the corresponding contributions to the uncertainty of the thermal conductivity.</b>	<b>112</b>

## **List of Figures**

Figure 2.1:	The diamond cubic unit cell.	5
Figure 2.2:	Schematic of a deposited diamond film sample.	6
Figure 2.3:	Microscopic view of CVD diamond film prepared by the hot filament method.	7
Figure 2.4:	Microscopic view of CVD diamond film prepared by the microwave method.	7
Figure 2.5:	Thermal conductivity parallel and perpendicular to the film surface.	10
Figure 2.6:	A block diagram of the type of experimental setup used by Albin, Winfree and Crews (1990) to determine thermal diffusivity.	18
Figure 2.7:	Schematic of the experimental setup for the photothermal laser beam deflection technique (Machlab et al., 1991).	19
Figure 3.1:	Ratio of the diamond film thickness to the silicon substrate thickness in the z direction.	24
Figure 3.2:	Schematic of the one dimensional model.	26
Figure 3.3:	Schematic of the two dimensional diamond film sample etched from the backside.	29
Figure 3.4:	Schematic of the two dimensional model.	30
Figure 3.5:	One of the symmetric quadrants for the two dimensional model.	31
Figure 3.6:	Schematic of the radial heat conduction model.	33
Figure 4.1:	The non-dimensional sensitivity coefficient as a function of characteristic length for different film thicknesses, 1D case.	39
Figure 4.2:	The non-dimensional sensitivity coefficient as a function of characteristic length for different temperature rises, 1D case.	40
Figure 4.3:	The non-dimensional sensitivity coefficient as a function of characteristic length for different film thicknesses, 2D case.	42

Figure 4.4:	Comparison of the non-dimensional sensitivity coefficient between the one dimensional and two dimensional cases at the same characteristic length.	43
Figure 4.5:	The non-dimensional sensitivity coefficient as a function of characteristic length for different temperature rises, 2D case.	44
Figure 4.6:	The non-dimensional sensitivity coefficient as a function of characteristic length for sample widths of 1.0, 0.50 and 0.25 cm, 2D case.	45
Figure 4.7:	The non-dimensional sensitivity coefficient as a function of diameter for different film thicknesses, radial case.	47
Figure 4.8:	The non-dimensional sensitivity coefficient as a function of diameter for different temperature rises, radial case.	48
Figure 4.9:	Comparison of the non-dimensional sensitivity coefficient as a function of characteristic length between the 1D, 2D and radial cases.	49
Figure 4.10:	Schematic of a sample with a doped diamond film, a layer of SiO <sub>2</sub> and a silicon substrate.	51
Figure 4.11:	Schematic of a sample with doped and undoped diamond films, a layer of SiO <sub>2</sub> and a silicon substrate.	51
Figure 4.12:	Schematic of the electrical circuit.	53
Figure 4.13:	Temperature rise as a function of applied voltage for different film thicknesses.	55
Figure 4.14:	The non-dimensional sensitivity coefficient as a function of ( $m_r$ * characteristic length) for the 1D, 2D and radial cases.	57
Figure 4.15:	Ratio of natural convection to the total heat generated in the doped film as a function of diameter for different film thicknesses.	59
Figure 4.16:	The non-dimensional sensitivity coefficient as a function of diameter for different doped and undoped film thicknesses.	60
Figure 4.17:	Photograph of the hot filament CVD diamond deposition chamber.	65
Figure 4.18:	Thickness of the undoped film on sample A measured in Å by the SEM.	65
Figure 4.19:	Thickness of the undoped film on sample B measured in Å by the SEM.	66
Figure 4.20:	Thickness of the doped film on sample A measured in Å by the SEM.	68
Figure 4.21:	Thickness of the doped film on sample B measured in Å by the SEM.	69
Figure 4.22:	The front side of sample A.	70

<b>Figure 4.23:</b>	<b>The diamond mask patterned on the back side of sample A.</b>	<b>71</b>
<b>Figure 5.1:</b>	<b>Schematic of the data acquisition system.</b>	<b>74</b>
<b>Figure 5.2:</b>	<b>The 600L Infrared Radiometer.</b>	<b>75</b>
<b>Figure 5.3:</b>	<b>The 6" close-up lens and the 3x telescope lens used to increase the spatial resolution of the radiometer.</b>	<b>77</b>
<b>Figure 5.4:</b>	<b>The Omega 880 Digital Multimeter.</b>	<b>79</b>
<b>Figure 5.5:</b>	<b>Corrected temperature of the thermocouple as a function of measured temperature of the radiometer.</b>	<b>80</b>
<b>Figure 5.6:</b>	<b>Heater surface temperature as a function of surface location.</b>	<b>83</b>
<b>Figure 5.7:</b>	<b>Schematic view of the sample after experimental preparation.</b>	<b>85</b>
<b>Figure 5.8:</b>	<b>Photograph of the sample after experimental preparation.</b>	<b>85</b>
<b>Figure 6.1:</b>	<b>Setup used to determine the emissivity of the diamond film for sample A.</b>	<b>87</b>
<b>Figure 6.2:</b>	<b>The relationship between the temperature measured by the radiometer and the temperature measured by the thermocouple at an emissivity setting of 0.63.</b>	<b>88</b>
<b>Figure 6.3:</b>	<b>Sample setup viewed from the front side.</b>	<b>94</b>
<b>Figure 6.4:</b>	<b>Sample setup viewed from the back side.</b>	<b>95</b>
<b>Figure 6.5:</b>	<b>Image 1 from experiment #1 at 0.40 watts.</b>	<b>97</b>
<b>Figure 6.6:</b>	<b>Image 2 from experiment #2 at 0.62 watts.</b>	<b>97</b>
<b>Figure 6.7:</b>	<b>Image 3 from experiment #3 at 0.88 watts.</b>	<b>97</b>
<b>Figure 6.8:</b>	<b>Image 4 from experiment #4 at 0.40 watts.</b>	<b>97</b>
<b>Figure 6.9:</b>	<b>Image 5 from experiment #5 at 0.88 watts.</b>	<b>97</b>
<b>Figure 6.10:</b>	<b>Measured and calculated temperature distribution for experiments 1, 2 and 3.</b>	<b>102</b>
<b>Figure 6.11:</b>	<b>Measured and calculated temperature distribution for experiments 4 and 5.</b>	<b>102</b>
<b>Figure 6.12:</b>	<b>Residual distribution for experiment #1, 107 pts.</b>	<b>103</b>
<b>Figure 6.13:</b>	<b>Residual distribution for experiment #2, 107 pts.</b>	<b>104</b>
<b>Figure 6.14:</b>	<b>Residual distribution for experiment #3, 107 pts.</b>	<b>104</b>

<b>Figure 6.15:</b>	<b>Residual distribution for experiment #4, 121 pts.</b>	<b>105</b>
<b>Figure 6.16:</b>	<b>Residual distribution for experiment #5, 121 pts.</b>	<b>105</b>
<b>Figure 6.17:</b>	<b>Sequential estimation of the thermal conductivity for experiment #1, 107 pts.</b>	<b>107</b>
<b>Figure 6.18:</b>	<b>Sequential estimation of the thermal conductivity for experiment #2, 107 pts.</b>	<b>107</b>
<b>Figure 6.19:</b>	<b>Sequential estimation of the thermal conductivity for experiment #3, 107 pts.</b>	<b>108</b>
<b>Figure 6.20:</b>	<b>Sequential estimation of the thermal conductivity for experiment #4, 121 pts.</b>	<b>108</b>
<b>Figure 6.21:</b>	<b>Sequential estimation of the thermal conductivity for experiment #5, 121 pts.</b>	<b>109</b>
<b>Figure A.1:</b>	<b>Setup used to calibrate the infrared radiometer to record transient events.</b>	<b>124</b>
<b>Figure A.2:</b>	<b>Vertical refresh signals resembling legitimate line scans.</b>	<b>129</b>
<b>Figure A.3:</b>	<b>Thermocouple temperature as a function of radiometer voltage for the six different calibration runs.</b>	<b>130</b>
<b>Figure A.4:</b>	<b>Radiometer voltage recorded in fast line scan mode during calibration.</b>	<b>131</b>

## Nomenclature

<b>k</b>	<b>Thermal Conductivity</b>	<b>[W/m K]</b>
<b><math>\epsilon</math></b>	<b>Emissivity</b>	
<b><math>\alpha</math></b>	<b>Thermal Diffusivity</b>	<b>[m<sup>2</sup>/sec]</b>
<b><math>c_p</math></b>	<b>Specific Heat</b>	<b>[J/Kg K]</b>
<b><math>\rho</math></b>	<b>Density</b>	<b>[kg/m<sup>3</sup>]</b>
<b>T</b>	<b>Temperature</b>	<b>[°C]</b>
<b><math>\delta_d</math></b>	<b>Thickness of Doped Film</b>	<b>[m]</b>
<b><math>\delta_u</math></b>	<b>Thickness of Undoped Film</b>	<b>[m]</b>
<b>h</b>	<b>Convection Coefficient</b>	<b>[W/m<sup>2</sup> K]</b>
<b><math>\Delta T</math></b>	<b>Temperature Difference</b>	<b>[°C]</b>
<b><math>\theta</math></b>	<b>Relative Temperature Rise</b>	<b>[°C]</b>
<b>A</b>	<b>Area</b>	<b>[m<sup>2</sup>]</b>
<b>Vol</b>	<b>Volume</b>	<b>[m<sup>3</sup>]</b>
<b>S</b>	<b>Least Squares Function</b>	
<b>X</b>	<b>Sensitivity Coefficient Matrix</b>	<b>[°C<sup>2</sup>-m/W]</b>
<b>V</b>	<b>Voltage</b>	<b>[V]</b>
<b>R</b>	<b>Electrical Resistance</b>	<b>[<math>\Omega</math>]</b>
<b><math>R_{[\zeta]}</math></b>	<b>Thermal Resistance</b>	<b>[W/K]</b>
<b>t</b>	<b>Time</b>	<b>[sec]</b>
<b>g</b>	<b>Volumetric Heat Generation</b>	<b>[W/m<sup>3</sup>]</b>
<b><math>m_f</math></b>	<b>Convective Fin Term</b>	<b>[1/m]</b>
<b><math>\beta</math></b>	<b>Eigenvalue</b>	
<b>r</b>	<b>Cylindrical Coordinate</b>	<b>[m]</b>

<b>b</b>	<b>Radius</b>	<b>[m]</b>
<b><math>\gamma</math></b>	<b>Nondimensional Sensitivity Coefficient</b>	
<b>L</b>	<b>Length</b>	<b>[m]</b>
<b><math>\ell</math></b>	<b>Characteristic Length</b>	<b>[m]</b>
<b><math>\rho</math></b>	<b>Resistivity</b>	<b>[<math>\Omega</math>-cm]</b>
<b><math>\sigma</math></b>	<b>Stefan-Boltzmann Constant</b>	<b>[W/m<sup>2</sup> K<sup>4</sup>]</b>
<b>E</b>	<b>Emissive Power</b>	<b>[W/m<sup>2</sup>]</b>
<b>q</b>	<b>Heat Flux</b>	<b>[W/m<sup>2</sup>]</b>
<b><math>w_\theta</math></b>	<b>Uncertainty in the Relative Temperature Rise</b>	<b>[°C]</b>
<b><math>w_k</math></b>	<b>Uncertainty in the Thermal Conductivity</b>	<b>[W/m K]</b>
<b><math>Y_j</math></b>	<b>Measured Temperature</b>	<b>[°C]</b>
<b><math>T_j</math></b>	<b>Calculated Temperature</b>	<b>[°C]</b>
<b>W</b>	<b>Width</b>	<b>[m]</b>
<b><math>\sigma_k</math></b>	<b>Standard Deviation of Thermal Conductivity</b>	<b>[W/m K]</b>
<b><math>\sigma_t</math></b>	<b>Standard Deviation of Temperature</b>	<b>[°C]</b>
<b><math>t_{1-\alpha/2}(n-p)</math></b>	<b>t statistic</b>	
<b>Pr</b>	<b>Prandtl Number</b>	
<b>Ra</b>	<b>Rayleigh Number</b>	
<b>Hz</b>	<b>Hertz</b>	<b>[cycles/sec]</b>
<b>Å</b>	<b>Angstroms</b>	<b>[10<sup>-10</sup> m]</b>
<b><math>\mu\text{m}</math></b>	<b>Micrometer</b>	<b>[10<sup>-6</sup> m]</b>
<b>A/D</b>	<b>Analog to Digital Conversion</b>	

## Subscripts / Superscripts

<b>eff</b>	<b>Effective</b>
<b>rad</b>	<b>Radiation</b>
<b>x,y,z</b>	<b>Directions</b>
<b>∞</b>	<b>Surroundings</b>
<b>m,n,j</b>	<b>Variable Indices</b>
<b>corr</b>	<b>Corrected</b>
<b>meas</b>	<b>Measured</b>
<b>hcap</b>	<b>Heat Capacity</b>
<b>b</b>	<b>Boundary</b>
<b>cond</b>	<b>Conduction</b>
<b>c</b>	<b>Cross-Sectional</b>
<b>act</b>	<b>Actual</b>
<b>  </b>	<b>Parallel</b>
<b>⊥</b>	<b>Perpendicular</b>

# **Chapter 1**

## **Introduction**

For centuries the diamond has captivated both spectator and scientist alike. From its brilliant sparkle and unequalled hardness, the diamond has long been a symbol of strength and perfection. Though desirable and intriguing in its physical makeup, nature alone held the secret to its existence, and its rarity limited its use. However, with recent discoveries in chemical vapor deposition (CVD), diamond has been transformed from its rare jewel status into a promising engineering material.

Diamonds are used in a wide variety of applications such as cutting and grinding tools, bearings and gears, biological prostheses, speakers, amplifiers, telecommunications systems, lasers, computer hard disks, integrated circuits, and transducers. Since diamond has the highest known thermal conductivity of 2600 W/m-K, six times that of copper and eight times that of gold, it also makes an ideal heat sink. For example, diamond would provide a means of dissipating large amounts of potentially damaging heat generated when integrated circuit chips are mounted in a dense configuration. Higher density integrated circuit configurations could form the basis for computers operating four orders of magnitude faster than the present-day types (Spehar, 1991).

Through its unique semiconduction capabilities and its "second-to-none" structural

integrity, significant contributions could also potentially be found in thermal sensors. Since diamond will resist corrosion, oxidation, diffusion, adhesion, chemical attacks, intense pressures and extreme temperatures, it makes a suitable sensor for temperature measurements in the harshest environments. In fact, only hot carbide-forming metals or strong oxidizing agents such as molten sodium nitrate will affect it. Applications might also be in hypersonic flight, nuclear reactors, and high temperature industrial processes.

In order for diamond to become a semiconductor, however, it must be doped with a material such as boron during synthesis. Boron allows the diamond crystals to become charge carriers and the doping levels can be varied depending on the desired resistivity. Since the added impurities can affect the behavior of diamond, the thermal properties of doped diamond films must be determined to insure the proper performance for the particular application.

However, doped diamond films pose several problems to traditional experimental methods used to determine thermal conductivity. Its micro-structural size and rapid thermal response limit both the thermocouple and the resistance thermometer as reliable temperature measurement devices. As a result, we turn to an infrared thermography temperature acquisition system which can image microstructures and track rapid thermal responses to obtain the necessary surface temperature data to estimate the thermal conductivity.

## **1.1 Objectives:**

The general objective of this research was the development of analytical tools and experimental methods which would allow thermal analysis of micro-structures. The primary objective of this work was to utilize these methods to determine the thermal conductivity of doped diamond films, which were manufactured by the Micro-Structures Laboratory at Michigan State University. In particular the objectives were:

- 1) to determine which experimental model yields the optimal estimation of the thermal conductivity,
- 2) to utilize analytical tools to determine the optimal design of the diamond specimens,
- 3) to prepare at least one "masked" diamond film specimen which corresponded to the optimal design specifications,
- 4) to design a suitable experimental set-up for accurate temperature measurements,
- 5) to implement the infrared thermography and high resolution image processing system to image the surface temperature of the film and determine the relative temperature rise,
- 6) to extract temperature data from the resulting thermal images and estimate the thermal conductivity ( $k$ ) of a doped CVD diamond film sample.

## **Chapter 2**

### **Background and Literature Review**

Perhaps the area of greatest potential for diamond films is in commercial and military electronics. With its remarkably high thermal conductivity, diamond films have already become an attractive material for applications as heat sinks and heat spreaders for various electronic components. In these applications, diamond films are used to alleviate the damaging effects of self-heating. They can deliver manufacturers of telecommunications, computers, and integrated circuit chips a much improved means of dissipating heat, boosting both component reliability and performance. A diode laser, for example, producing a beam which gives a line heat source a few microns wide can be cooled effectively by mounting it against a diamond heat spreader (Graebner et al. 1992). In addition to being an "ideal" heat spreader for high energy density lasers, diamond has the potential itself to become a laser. A diamond laser core would withstand extreme high thermal stress due to its ability to efficiently conduct heat, decreasing heat expansion and ultimately increasing laser efficiency (Spehar 1991). However, defining the limits of applicability for diamond films has required an understanding of the thermophysical characteristics of the material.

## 2.1 CVD Diamond Films

Diamond films, like the diamond gem, consists of carbon atoms bonded together in strong sigma type covalent bonds. The atomic orbitals are  $sp^3$  and the bonds formed are very strong. The carbon atoms are arranged in a tetrahedral formation resulting in the diamond cubic unit cell seen in Figure 2.1.

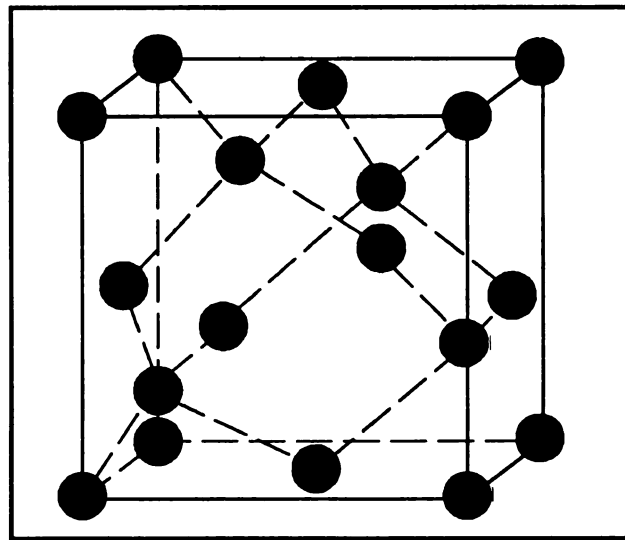
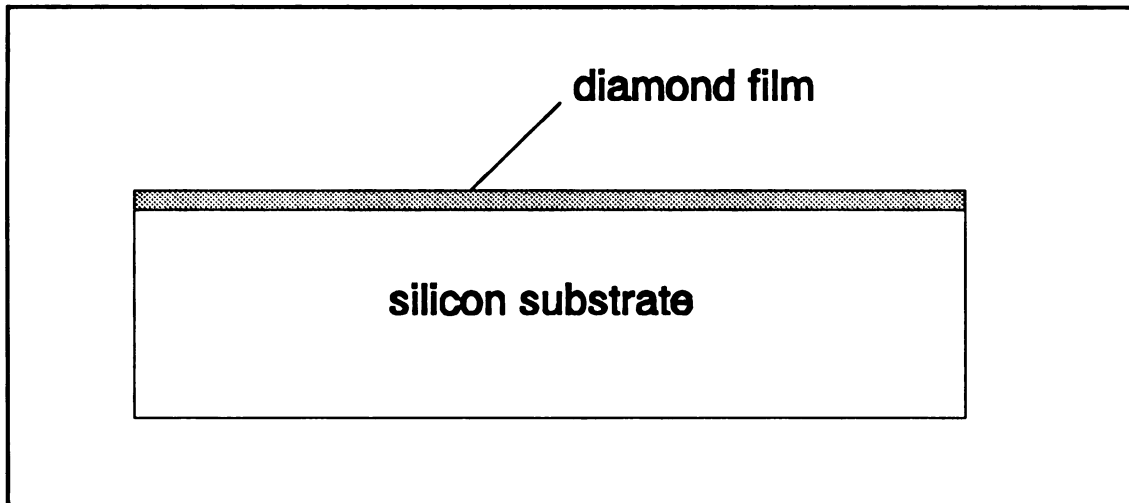


Figure 2.1. The Diamond Cubic Unit Cell

The structure of diamond gives rise to extreme hardness with the ability to withstand pressures of over 900,000 lbs/in<sup>2</sup>. The stiffness of these unique molecular bonds also contribute to diamond's high thermal conductivity. In nonmetallic materials, heat conduction occurs primarily through a phonon to phonon transfer phenomenon. This mechanism, which is dependent on the molecular vibrational energy within a material, is most efficient when atomic bonds are stiff and is dampened when bonds are elastic.

Through a process known as chemical-vapor deposition (CVD), polycrystalline diamond films can be deposited on non-diamond substrates, such as silicon, from carbon enriched gas mixtures, see Figure 2.2. The two most commonly used CVD methods for



**Figure 2.2.** Schematic of deposited diamond film sample.

heating the surface of the substrate to induce diamond growth are known as the hot-filament assisted method, which uses electrically resistive heating, and the plasma enhanced microwave method. The hot-filament heating provides higher quality diamond films but at low deposition rates, between 0.5-1.0  $\mu\text{m/hr}$ . A photograph of the surface of a diamond film prepared by the hot-filament method is viewed in Figure 2.3. On the other hand, the microwave heating method provides a higher deposition rate, usually between 1-4  $\mu\text{m/hr}$ , but at a lower quality film. A photograph of the surface of a diamond film prepared by the microwave heating method is seen in Figure 2.4.

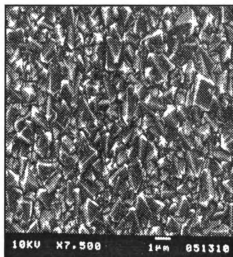


Figure 2.3. Microscopic view of CVD diamond film prepared by the hot filament method.

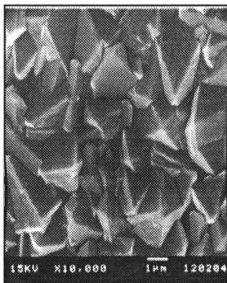


Figure 2.4. Microscopic view of CVD diamond film prepared by the microwave method.

However, even when using the best CVD system one must be aware that a certain amount of impurities and defects normally are present as a result of this process. Although research into the CVD process over the past few years has increased the quality of the diamond, impurities still have a major effect on the physical properties of diamond, especially the thermal conductivity. For example, Baba et al. (1991) reported that by increasing the methane ( $\text{CH}_4$ ) concentration from 1% to 5% the thermal conductivity decreased from 1200 W/mK to 200 W/mK. This reduction was assumed to be the result of phonon scattering due to the hydrogen impurity found in the films. The thermal conductivity can also be severely affected by the structural defects of the film. Bad grain boundaries can result in poor thermal contact within the films. Since CVD diamond films are prone to impurities and small defects, its application as a heat sink could be quite restrictive without experimentally determining the thermal conductivity.

## **2.2 Experimental Methods Determining Thermal Properties**

Generally, methods of determining the thermophysical characteristics of materials are divided into three groups: steady state methods, quasi-stationary methods, and transient methods (Vorobei 1986). The estimation of the thermal conductivity is not limited to any one of these methods. However, the estimation of thermal diffusivity or volumetric heat capacity requires transient experiments. The phenomenon of heat conduction is simply described by heat flowing down a temperature gradient to restore thermal equilibrium. Thus, it is necessary to introduce a heat source to perturb the thermal equilibrium in the material of interest to establish a temperature gradient. The temperature distribution and the applied heat must be measured in order to estimate the

thermal properties. The mathematical description will be discussed later in Chapter 3.

There are basically two different types of experimental analysis currently in use, the absolute method and the relative method. The absolute method provides a very accurate means of estimating the thermal properties but it requires expensive instrumentation (e.g. thermocouples, resistance thermometers, IR cameras, heaters, etc.) and great care in their use. In the relative method the thermal conductivity is determined by reference to a material of known conductivity. Due to the desired accuracy of the present analysis, the absolute method is employed in this work.

### **2.3 Special Experimental Methods for CVD diamond**

There have been several important experimental studies concerning the thermal conductivity of CVD diamond films over the past several years. The different experimental techniques used in these works can be divided into four different categories: surface instrumentation, the laser pulse technique, IR radiation thermography and photothermal laser beam deflection. These techniques and experimental procedures which are instrumental in determining thermal conductivity both parallel ( $k_{\parallel}$ ) and perpendicular ( $k_{\perp}$ ) to the film surface are discussed in turn in the following paragraphs, see Figure 2.5.

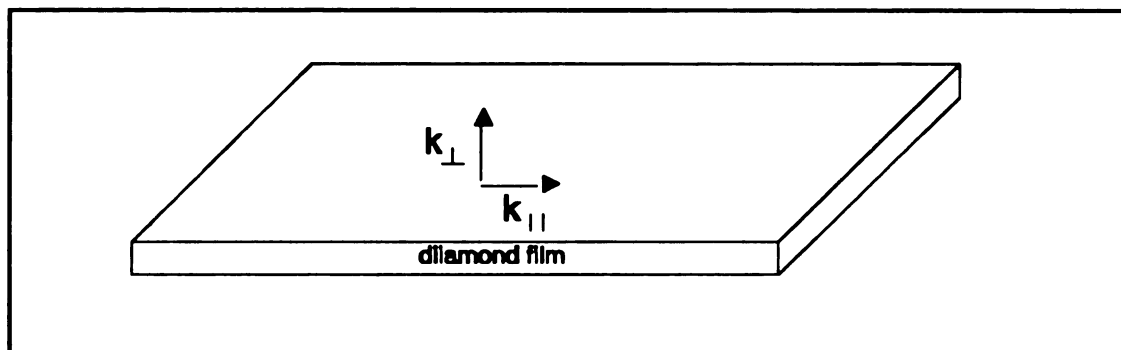


**Figure 2.5.** Thermal conductivity parallel and perpendicular to the film surface.

*Surface Instrumentation:*

Surface instrumentation (such as, thermocouples, thermistors and resistance thermometers) is currently the most common form of detecting and recording the temperature distribution on the surfaces of diamond films. Morelli, Beetz and Perry (1988) introduced an experimental procedure known as the steady state four-probe technique to determine the thermal conductivity parallel ( $k_{\parallel}$ ) to the surface of the film as a function of thickness and temperature. This method involves the use of a thin film heater and four thermocouples. The heater which was attached to one end of the diamond film sample generated a thermal gradient across the film surface. The thermocouples which were also attached to the surface using conductive silver paint monitored the temperature distribution. The substrate was etched away from the backside resulting in a window 10mm x 5mm of free standing diamond. The sample was then placed in a vacuum so that convection could be neglected. The effects of radiation were minimized by enclosing the sample between two metal shrouds. The heat input and the temperature

distribution were recorded at steady state and the thermal conductivity was determined as a function of temperature and thickness. The absolute uncertainty in their results (~15%) was determined by the accuracy to which the film thickness could be measured. The relative uncertainty was determined from the resolution of the thermocouple voltage (~1-2%) at room temperature. Table 2.1 displays some of their experimental results.

Thickness ( $\mu\text{m}$ )	$k_{\parallel}$ (W/m K)
1	800
10	1000
100	1100

**Table 2.1.** Thermal conductivity of diamond film evaluated at different thicknesses at room temperature, Morelli, Beetz and Perry (1988). Films were prepared using the hot filament method.

Anthony, Fleischer, Olson and Cahill (1991) estimated the thermal conductivity both parallel ( $k_{\parallel}$ ) and perpendicular ( $k_{\perp}$ ) to the surface of a diamond film. The sample, which had dimensions 3.3cm x 1.5 cm x 170  $\mu\text{m}$ , was also prepared by the hot-filament CVD method. In their study, two different techniques which utilized surface instrumentation were used. Parallel to the surface the thermal conductivity was measured between 6-100 K using the steady-state four-probe technique. A 1000-W CuNi thin film heater was attached to one end of the sample to induce the temperature gradient and carbon resistance thermometers, which were attached to the surface of the sample, recorded the temperature distribution. In the perpendicular plane,  $k_{\perp}$  was determined

between 80-300 K using what they termed as an "ac diffusive heat wave technique". Here a silver line 100  $\mu\text{m}$  wide and 3000  $\text{\AA}$  thick was deposited directly on a silicon substrate to act as a heater-thermometer. By knowing the thermal conductivity of the substrate and by measuring the temperature at the opposite face they calculated  $k_{\perp}$ . From their study Anthony and Fleischer concluded that the thermal conductivity of diamond was a strong function of temperature. They also found that  $k_{\perp} > k_{\parallel}$  but were unable to positively conclude this due to experimental errors associated with each method.

Graebner, Jin, Kammlott, Herb and Gardinier (1992) used a similar setup to determine the thermal conductivity parallel to the film surface ( $k_{\parallel}$ ) using two thin film heaters which were evaporated directly onto the sample, one near each end. The temperature distribution was measured again by a row of four very fine thermocouples. Measurements were performed on several samples prepared by the microwave CVD method. The samples having different thicknesses were placed in a vacuum where the effects of convection and radiation were neglected. From their study Graebner, Jin and Kammlott also concluded that the thermal conductivity was a function of the film thickness.

Graebner, Mucha, Seibles and Kammlott (1992) determined the thermal conductivity using a technique that involved etching a window of free standing diamond  $2 \times 4 \text{ mm}^2$ , similar to the Morelli, Beetz and Perry (1988) procedure. The remaining silicon served as a rugged platform to support the film as well as a heat sink and a referenced temperature boundary. The flow of heat from a heater in the center of the window was monitored with thermocouples. The thin film heater and the chromel and constantan thermocouples were deposited on the surface of the diamond by standard

evaporation techniques. The steady state temperature distribution, detected by the thermocouples, was then compared with a numerical simulation to extract the thermal conductivity parallel to the surface ( $k_{\parallel}$ ). Their efforts yielded values for  $k_{\parallel}$  in the range of 200-600 W/m°C. The choice of window dimensions was made to reduce the effects of radiation. To predict the thermal influence from radiation they developed the ratio,

$$\frac{k_{rad}}{k_{cond}} \sim \frac{2\sigma\epsilon w^2 T_o^3}{\kappa t} \quad 2.1$$

where  $k_{cond}$  is the conductance of heat along the film of thickness  $t$ ,  $k_{rad}$  is the effective conductance due to radiation between the film and its surroundings,  $\sigma$  is the Stefan-Boltzman constant and  $\kappa$  is the thermal conductivity. By evaluating this ratio under unfavorable conditions  $\epsilon=1$ ,  $T_o=300$  K,  $t = 2\mu\text{m}$  and  $\kappa = 300$  W/m K and varying the width ( $w$ ), they were able to neglect the effects of radiation when the ratio became significantly small. The effects of convection were not considered in their study. The results of their study are presented in the Table 2.2.

Thickness ( $\mu\text{m}$ )	$k_{\parallel}$ (W/m K)
2.8	410
3.8	400
7.0	600
7.3	330
7.5	460
7.8	452
7.8	500
10.6	280
11.6	335
13.1	190

**Table 2.2.** Thermal conductivity parallel to the film surface ( $k_{\parallel}$ ) as a function of film thickness presented by Graebner, Mucha, Seibles and Kammlott (1992)

Baba *et al.* (1991) concluded that the thermal conductivity for diamond films was also dependent on the amount of hydrogen impurity deposited from the methane ( $\text{CH}_4$ ) gas mixture. In this study an experimental method termed the "ac calorimetric" method was employed. Here, one end of the diamond samples was periodically heated by a halogen lamp. The temperature amplitude ( $T_{AC}$ ) at a distance ( $x$ ) away from the heat source was monitored by a thermocouple which was attached to the sample's surface. A relation between  $T_{AC}$  and distance ( $x$ ) is given by

$$\ln |T_{AC}| = \ln \left( \frac{q}{4\pi f d C_p} \right) - \left( \frac{\pi f}{\alpha} \right) x \quad 2.2$$

where  $q$  is heat quantity,  $f$  is the heating frequency, and  $C_p$ ,  $d$  and  $\alpha$  are the specific heat, thickness and the thermal diffusivity of the film. The thermal conductivity was extracted from the diffusivity of two samples and evaluated from the slope of the above equation by varying  $x$ . The thermal conductivity of the film prepared with 1%  $\text{CH}_4$  concentration reached 1200 W/m K but the thermal conductivity of the film prepared with 5%  $\text{CH}_4$  concentration decreased to less than 200 W/m K. Both samples were hot-filament CVD films.

*Laser Pulse Technique:*

While it is relatively straightforward to measure  $k_{\parallel}$  using surface instrumentation, it is much more difficult to measure  $k_{\perp}$  perpendicular to the film surface due to the small thermal resistance in this direction. For this reason a non-contact method which uses laser pulses to heat the face of the film and fast thermometry to monitor the arrival of the thermal wave at the opposite face is employed. The thermal conductivity can then be related to the short duration thermal shock applied by the laser.

Graebner, Jin, Kammlott, Bacon and Seibles (1992) utilized this laser pulse technique to help determine whether any anisotropic behavior existed in their CVD diamond films. In their study the thermal conductivity parallel to the surface  $k_{\parallel}$  was determined using standard surface instrumentation procedures previously discussed and the thermal conductivity perpendicular to the surface  $k_{\perp}$  was determined by using a Q-switched Nd:YAG laser as a heat source. The sample was glued with silver paste over

a hole to a temperature controlled copper plate. Germanium lenses were used to collect thermal radiation and measure the temperature on the back side of the sample. The heat from each laser pulse conducted laterally through the sample to thermal ground at its edges. The temperature rise on the back surface and the rapid transient after each pulse were recorded by the system. The thermal jump  $\Delta T(t)$  was calculated from the analytical expression presented by Parker *et al.* (1961)

$$\Delta T(t) = A \left[ 1 + 2 \sum_{n=1}^{\infty} (-1)^n \exp \left( \frac{-n^2 \pi^2}{L^2} \alpha t \right) \right], \quad 2.3$$

where  $A = q/\rho C_p L$  and  $\alpha = k_{\perp}/\rho C_p$ ;  $q$  is the absorbed energy per unit area and  $\alpha$  is the thermal diffusivity. Equation 2.3 is used to solve a system of equations where  $A$  and  $\alpha$  are the unknown quantities. By solving for the thermal diffusivity and measuring both the thermal response and the characteristic length of the film, the thermal conductivity,  $k_{\perp}$ , was calculated assuming a value for  $\rho C_p$ . A conductivity  $k_{\perp}$  of 800 and 1210 W/m K was found for two different samples with thicknesses of 234 and 144  $\mu\text{m}$  respectively. Values for  $k_{\perp}$  were observed to be at least 50% greater than values obtained for  $k_{\parallel}$ .

Later the same year Graebner, Jin, Kammlott, Herb and Gardinier utilized a similar setup to determine  $k_{\perp}$  as a function of thickness. Here the film surface was heated using a periodic laser pulse. The temperature at the top surface was monitored using a high speed infrared detector. Four samples, 0.5 x 1.0  $\text{cm}^2$  in area, with average thicknesses ranging between 28-408  $\mu\text{m}$  were evaluated. Their results concluded that the average  $k_{\perp}$  through the film increased from 1000 to 2100 W/m K as the thickness increased.

*Infrared Thermography:*

Ono, Baba, Tunomoto and Nishikawa (1986) utilized this non-contact method to determine the thermoconductivity parallel to the film surface. Using a long diamond film sample suspended by heated supports in a vacuum, the temperature distribution along the length was measured by an infrared thermograph. The surface area of the samples analyzed was 20 mm x 5 mm while the thicknesses varied between 7-30  $\mu\text{m}$ . Measurements were made between 100 °C and 130 °C on microwave plasma CVD diamond. From the results of this study, the thermal conductivity of the diamond films increases rapidly with decreasing concentration of methane. The highest value for  $k_{\parallel}$  was approximately 1000 W/m K.

A significant study determining the  $k_{\parallel}$  of diamond films using IR thermography was later done by Albin, Winfree and Crews (1990). The thermal conductivity was extracted from the measurement of the thermal diffusivity. Periodic heating was provided by a 20W, 1.064  $\mu\text{m}$  Nd:YAG laser and the time dependent surface temperature was measured by a 8-12  $\mu\text{m}$  infrared camera. A diagram of the set-up is displayed in Figure 2.6.

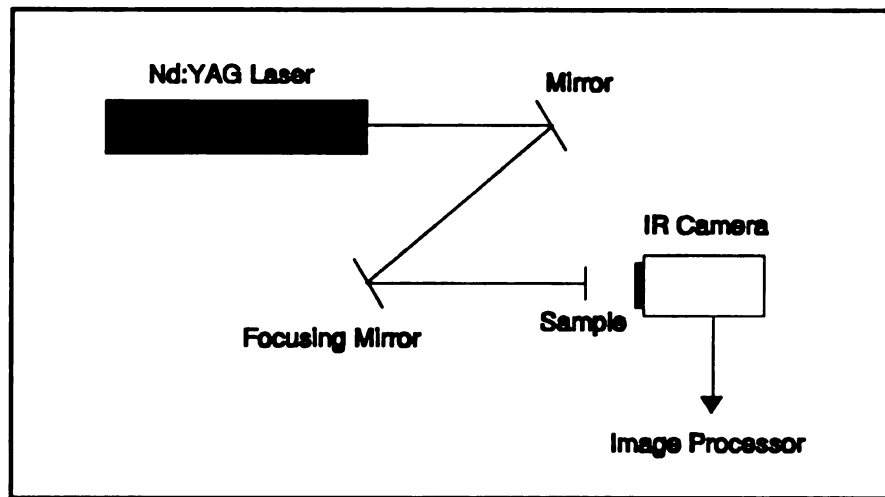


Figure 2.6. A block diagram of the type of experimental setup used by Albin, Winfree and Crews determining thermal diffusivity.

Temperature measurements between 25-35 °C were made on the back side of the sample using the infrared camera. The camera scanned a single horizontal line which passed through the center of the sample and the heating area. An image processor was used to digitize 128 successive images. Each image was compressed into a single temperature profile resulting in a sampling rate of 1/30 of a second. The IR camera allowed for a temperature resolution of less than 0.02 °C and a spatial resolution of better than 1 mm. In this study  $k_f$  for two samples of thickness 16 and 32  $\mu\text{m}$  were determined to be 1350 and 1328 W/m K respectively. The advantage of this technique is that the thermal diffusivity and the thermal conductivity of diamond films can be determined without special sample preparation.

***Photothermal Laser Beam Deflection:***

The technique known as photothermal laser beam deflection was introduced by Machlab, McGahan and Woolham (1991) as an alternate method of determining  $k_f$  in diamond films. This technique also known as the "mirage effect" uses the assistance of two separate laser beams. A diagram of the experimental setup used by Machlab, McGahan and Woolham is displayed in Figure 2.7.

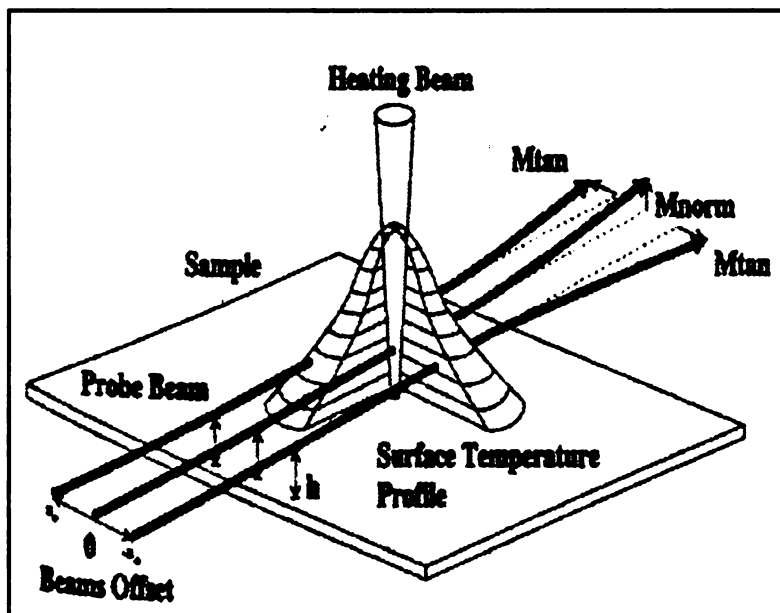


Figure 2.7. Schematic of the experimental setup for the Photothermal Laser Beam Deflection Technique, Machlab *et al.*, 1991.

One beam generates heat pulses within the sample producing heat pulses in the air above. The thermal pulse in the air results in an optical index of refraction gradient. The second beam passes through the index of refraction gradient and is deflected with components

both in the plane and perpendicular to the plane of the sample. Since the heating beam is periodic, the wavelength of these propagating waves can be detected. Because the wavelength of these thermal waves depends on the frequency of the heating beam and on the thermal properties, the thermal conductivity  $k_{\parallel}$  can be obtained. Although their study did not include experimental results for diamond films, they were successful in determining  $k_{\parallel}$  for aluminum. This method like the laser pulse technique and IR radiation thermography offers a non-destructive experimental evaluation of the thermal properties in CVD diamond films.

Although there have been several studies on the thermal conductivity of diamond films in recent years, they have focused on non-doped films for heat sink applications. Presently, very little is known about the effects boron doping will have on the properties of diamond. As a result, the author was unable to find information concerning the thermal characteristics of doped diamond films.

Without an understanding of how the doping process affects the thermal properties of CVD diamond films, applications as a semiconductor could be restricted and unreliable. As a result, experimental methods and analytical tools are presented in the present work to aid in the determination of the thermal conductivity of doped diamond films.

## **Chapter 3**

### **Problem Description**

In the area of inverse heat conduction, which includes the estimation of the thermal properties of a material from the relative temperature distribution and temperature rise, it is imperative that an accurate mathematical model of the system be developed. The mathematical model is used to describe the experimental setup such that the thermal behavior of the experiment can be predicted analytically. Without such a model, the thermal properties cannot be determined and without an accurate description from the model, any results are meaningless. Since there is a certain amount of error and uncertainty associated with different experimental setups, the role of the mathematical model can also become instrumental in pre-determining the overall success of an experiment. This section is dedicated to the discussion of three different mathematical models considered in the present work. The models will later be analyzed in Chapter 4 to determine the "best" experimental setup.

#### **3.1 Mathematical Modeling**

The phenomenon of heat conduction is described by the energy of motion between adjacent molecules. In nonmetallic solids, molecules having greater energy and

motion translate their energy to adjacent molecules at lower energy levels. In a solid body with a temperature gradient, Fourier's Law is used to relate the heat flux ( $q$ ) to the

$$\mathbf{q}(r, t) = -\mathbf{k}(r, t) \nabla T(r, t) \quad 3.1$$

temperature ( $T$ ) where the tensor  $\mathbf{k}$  [W/m K] is the effective thermal conductivity of the material, the temperature gradient  $\nabla T$  [°C/m] is a vector normal to the isothermal surface and the heat flux vector  $\mathbf{q}$  [W/m<sup>2</sup>] is the heat flow per unit time and unit area. The minus sign is inserted in accordance with the second law of thermodynamics. For example, if heat flows in a positive direction, the temperature must decrease in that direction. The three components of  $\mathbf{q}$  in the  $x$ ,  $y$  and  $z$  directions are given by

$$q_x = -k_x \frac{\partial T}{\partial x}, \quad q_y = -k_y \frac{\partial T}{\partial y}, \quad q_z = -k_z \frac{\partial T}{\partial z} \quad 3.2$$

for an orthotropic solid (Carslaw and Jaeger, 1959). The accurate estimation of the thermal conductivity  $\mathbf{k}$ , involves a solution to the heat conduction equation,

$$\int_{c.s.} (-\mathbf{q} \cdot \mathbf{n}) dA + \int_{c.v.} g(r, t) dV = \int_{c.v.} \rho C_p \frac{\partial T}{\partial t} dV, \quad 3.3$$

which is derived from the conservation of energy (Beck et al. 1992). The first term represents the net heat flux rate into the control volume;  $g(r,t)$  is the rate of internal volumetric heat generation; and the right side of the equation represents the energy storage rate. The solution of the equation in this study is solved for the following general assumptions:

- 1) heat dissipated through natural convection,
- 2) insulated at edges
- 3) radiation neglected
- 4) no energy storage (steady state condition),
- 5) isothermal in the z direction;  $q_z = 0$ ,
- 6) diamond film is isotropic.

Under these assumptions, general steady state heat conduction reduces to,

$$\int_{c.s.} (-\mathbf{q}\mathbf{n}) dA + \int_{c.v.} g(\mathbf{r}, t) dV = 0 \quad 3.4$$

Steady state experiments were chosen to be modeled instead of transient experiments due to the performance limitations of the experimental equipment. Although the data acquisition system, comprised of the infrared camera and the image processor, had excellent spatial resolution when viewing still thermal images, the image processor software is not equipped for imaging transient events. In light of this, another data-acquisition system, comprised of the infrared camera and the National Instruments AT-MIO-16F5 A/D board, was developed by the author. Using this system transient thermal events can be acquired, however, the spatial resolution is poor since the infrared camera's sampling rate is nearly ten times that of the fastest allowable sampling rate on the available A/D board. A detailed description of both data acquisition systems is given later in Chapter 5 and Appendix A.

Significant amounts of heat dissipated through convection and radiation can cause

severe problems in the estimation of the thermal conductivity of microstructures such as CVD diamond films. For this reason, analytical tools are presented later in Chapter 4 to help aid in the minimization of these errors and to better define what "significant" means in regards to the experimental results.

In order to improve our experimental results to determine the thermal conductivity  $k_{\parallel}$ , which is the effective thermal conductivity parallel to the diamond film surface, we must maximize the heat conduction in the film and minimize the heat conduction in the silicon substrate parallel to the film surface, see Figure 3.1.

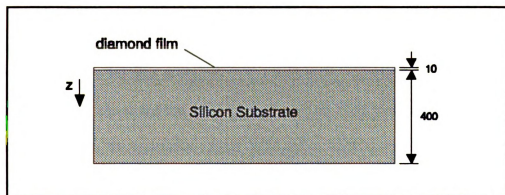


Figure 3.1. Ratio of the diamond film thickness to the silicon thickness in the z direction.

By comparing the thermal resistance of the diamond to the silicon in the parallel plane we see that,

$$\frac{R_d}{R_{si}} = \frac{k_{si} \delta_{si}}{k_d \delta_d} \quad 3.5$$

where  $R_{[j]}$  is the thermal resistance and  $\delta_{[j]}$  is the thickness of each layer. With  $k_{si} = 150$  W/mK,  $k_d = 1000$  W/m K,  $\delta_{si} = 400$   $\mu$ m and  $\delta_d = 10$   $\mu$ m, which are normal values for the thermal conductivity and the thickness, the thermal resistance in the diamond will be approximately six times that of the silicon substrate,  $R_d = 6R_{si}$ . Under these conditions, the thermal conductivity of the silicon is determined instead of the diamond film. For this reason, the silicon substrate must be etched from the backside of the sample leaving a window of free-standing diamond. An explanation of the etching process will be given later in Chapter 4.

### 3.1.1 One Dimensional Heat Conduction Model

The one dimensional heat conduction model was chosen because its solution is readily derived. The solution is also in a form that results in quicker and easier analytical analysis. However, the analytical advantage presents several experimental disadvantages. One disadvantage is the extensive sample preparation that must be done to ensure one dimensional heat flow. The top and bottom of the sample must be patterned and etched to get a channel of free standing diamond film. The sample is also very fragile due to the necessary geometry.

For the one dimensional case, we make the special assumption that the temperature gradient occurs only in the x direction. This can be done experimentally by making the characteristic length much greater than the width. With this additional assumption, the governing heat conduction equation reduces to the partial differential equation,

$$k \frac{\partial^2 T}{\partial x^2} - \frac{2h}{\delta} (T - T_{\infty}) + g = 0 \quad 3.6$$

where  $h$  is the convection coefficient [ $\text{W}/\text{m}^2 \text{K}$ ] on both sides,  $\delta$  is the thickness of the film,  $T_\infty$  is the temperature of the surroundings and  $g$  is the volumetric heat generation [ $\text{W}/\text{m}^3$ ] in the diamond film. A schematic diagram of the one dimensional model is displayed in Figure 3.2.

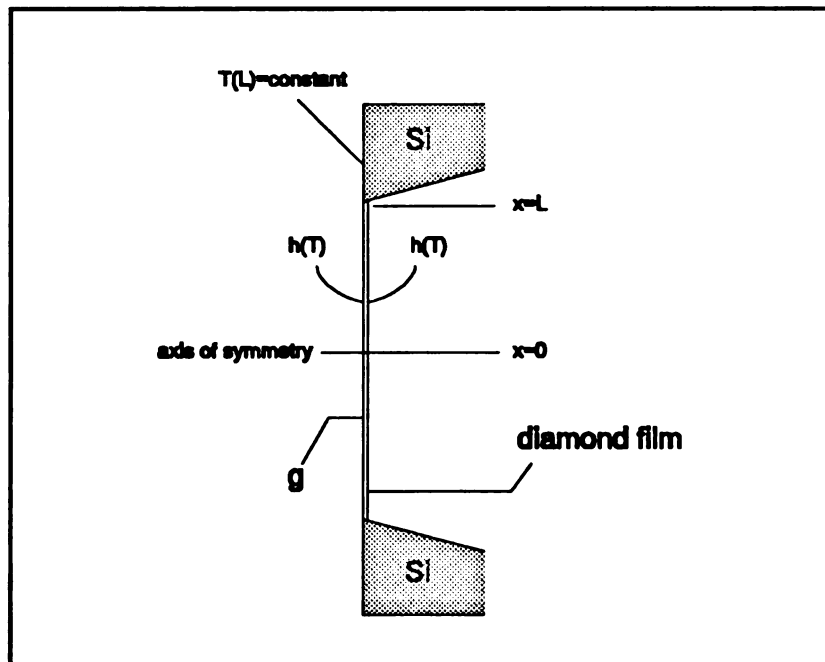


Figure 3.2. Schematic of the one dimensional model.

The free standing film behaves as a fin suspended in air. As heat is generated in the film a temperature distribution on the surface of the film forms about the center while the silicon maintains a constant temperature condition at the ends.

Because equation 3.6 is of second order, two boundary conditions are required for

the solution. Since the temperature profile from  $x = 0$  to  $x = L$  is assumed to be a mirror image of the temperature from  $x = 0$  to  $x = -L$  we can effectively describe the temperature distribution over the entire length by modeling one half of the exposed film. Therefore, we pick the first boundary condition at  $x = 0$ . This is a boundary condition of the second kind (Beck *et al.*, 1992) and is described by,

$$-k \frac{\partial T}{\partial x} \Big|_{x=0} = 0 \quad 3.7$$

The boundary condition at  $x = L$  is of the first kind and is described by,

$$T(x=L) = \text{constant} \quad 3.8$$

The assumption of this boundary condition is made due to the silicon substrate that remains at the edges of the sample, see Figure 3.2. The silicon which is more than 40 times the thickness of the diamond film and having a thermal conductivity of 150 W/m K acts as a thermal heat sink. The increased thermal mass at the edges is assumed to increase the temperature gradient across the film and allow the temperature at this boundary to remain at a lower constant value compared to the exposed surface of the film at steady state. Using the boundary conditions at  $x = 0$  and  $x = L$  yields the exact one dimensional solution,

$$T(x) = \left[ (T_{si} - T_{\infty}) - \frac{g\delta}{2h} \right] \frac{\cosh(m_f x)}{\cosh(m_f L)} + \frac{g\delta}{2h} + T_{\infty} \quad 3.9$$

where  $T_{si}$  is the temperature of the silicon at  $x = L$  and

$$m_f = \sqrt{\frac{2h}{k\delta}} \quad 3.10$$

### 3.1.2 Two Dimensional Heat Conduction Model

A two dimensional heat conduction model in cartesian coordinates was chosen to reduce some of the experimental challenges characteristic of the one dimensional model. This two dimensional model allows for less sample preparation, heat conduction throughout the plane of the film and a stronger film sample. Although this model is experimentally much friendlier, it is more difficult analytically.

In the two dimensional model, the coordinate system is defined parallel to the mutually perpendicular directions of the heat conduction so that the geometry is said to be orthotropic. The heat conduction equation for orthotropic bodies is assumed not to contain cross-derivatives. In addition, the thermal conductivity is considered to be the same in the x and y directions which is known as an isotropic condition. In the two dimensional model, heat is free to flow in the plane of the film, in directions x and y. By applying this special assumption, the two dimensional heat equation for this case is,

$$k \frac{\partial^2 T}{\partial x^2} + k \frac{\partial^2 T}{\partial y^2} - \frac{2h}{\delta} (T - T_\infty) + g = 0 \quad 3.11$$

where the thermal conductivity is assumed to be constant throughout the film. For this model special design considerations are also needed for the sample. Although detailed information on the design and fabrication of the actual diamond sample is given in

Chapter 4, a schematic of the physical design of the sample for the two dimensional model is displayed in Figure 3.3.

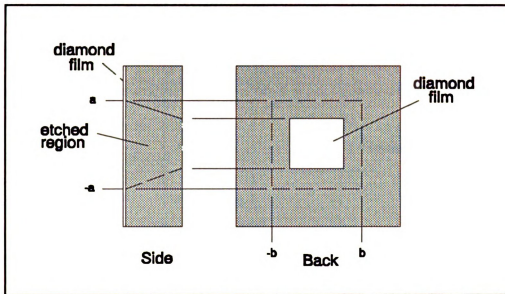


Figure 3.3. Schematic of the two dimensional diamond film sample, etched from the backside.

Here, the sample is etched from the backside resulting in a rectangular window of free standing diamond at the center. Such a sample would still have the silicon substrate at the edges to maintain the temperature boundary condition. By designing the sample in this way, we can solve the governing two dimensional equation using a model which has volumetric heat generation  $g$  [ $W/m^3$ ], constant temperature boundary conditions, and two axes of symmetry. A schematic of the model is displayed in Figure 3.4.

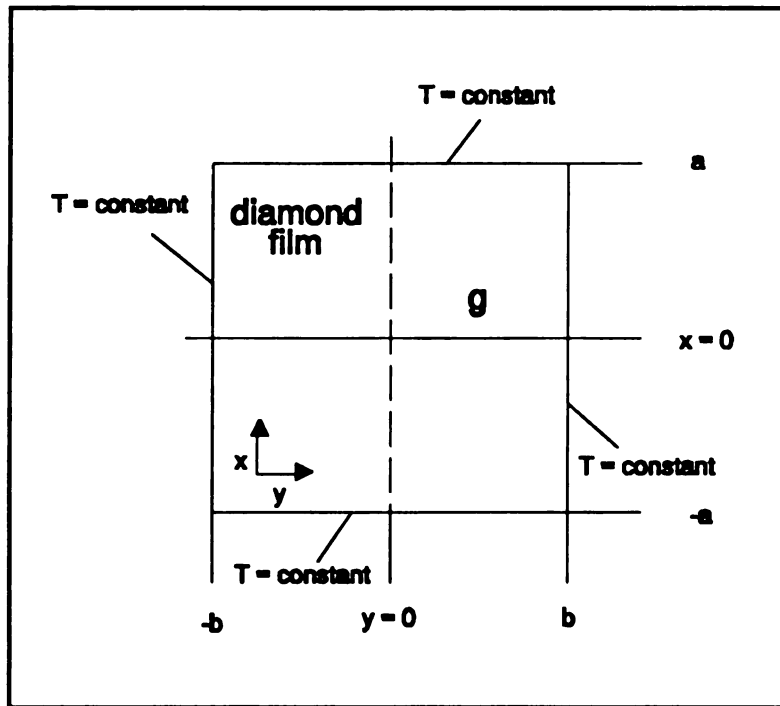


Figure 3.4. Schematic of the two dimensional model.

Since the model has four symmetric quadrants, we can effectively determine the temperature distribution on the entire face of the film by mathematically describing the temperature distribution in just one of the quadrants. A diagram of one of the symmetric quadrants is displayed in Figure 3.5.

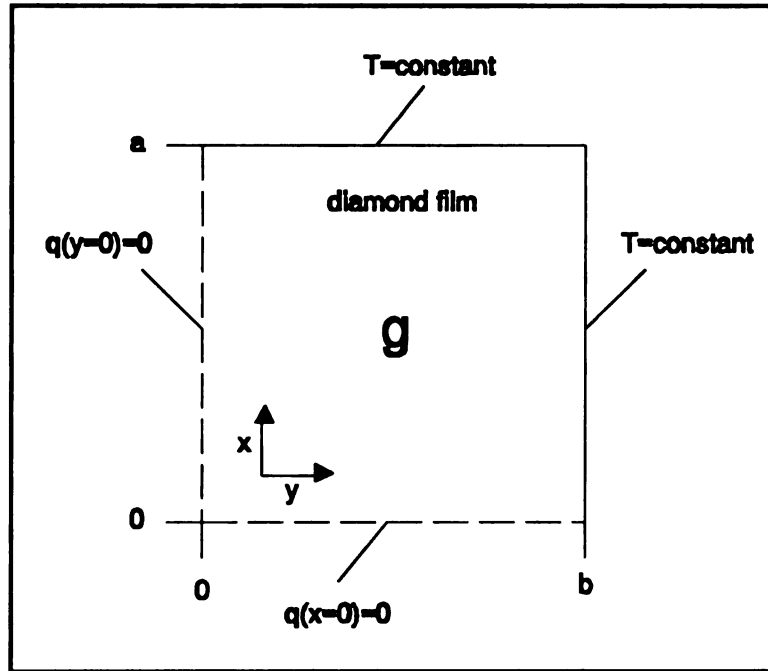


Figure 3.5. One of the symmetric quadrants for the two dimensional model.

With a boundary condition of the second kind at  $x = 0$  and  $y = 0$  and a boundary condition of the first kind at  $x = a$  and  $y = b$ , we turn to the Green's functions,  $G_{x21}$  and  $G_{y21}$ , to obtain the solution,

$$T(x, y) = \frac{4g}{k} \sum_{m=1}^{\infty} \sum_{n=1}^{\infty} \frac{\cos(\beta_m \frac{x}{a}) \cos(\beta_n \frac{y}{b}) (-1)^{m-1} (-1)^{n-1}}{\beta_m \beta_n [(\frac{\beta_m}{a})^2 + (\frac{\beta_n}{b})^2 + m_f^2]} + T_{\infty}, \quad 3.12$$

where  $\beta_m = \pi(m-1/2)$  and  $\beta_n = \pi(n-1/2)$ , (Beck *et al.*, 1992).

### 3.1.3 Radial Heat Conduction Model

The radial heat conduction model was chosen as a compromise between the analytical simplicity of the one dimensional model and the experimental advantages of the two dimensional model. The steady state solution for this model is well known and easily obtained for different conditions. Although the heat conduction would be restricted to one direction, it would also spread throughout the plane of the film, as in the two dimensional case.

For the one dimensional radial heat flow model, we make the special assumption that heat conduction is restricted to the radial direction. The physical design of the sample would be similar to the two dimensional case, but would have an exposed diamond window which is circular instead of rectangular, see Figure 3.6 For the one dimensional radial model the governing equation becomes,

$$k \frac{d^2 T}{dr^2} + k \frac{1}{r} \frac{dT}{dr} - \frac{2h}{\delta} (T - T_{\infty}) + g = 0 \quad 3.13$$

A schematic drawing of the one dimensional model for radial heat flow is displayed in Figure 3.6.

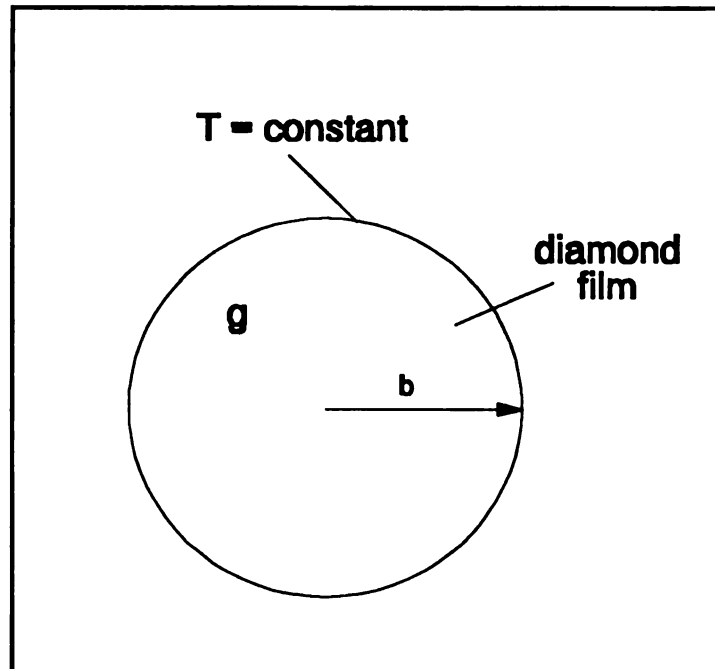


**Figure 3.6.** Schematic of the radial heat conduction model.

The general solution for the one dimensional radial heat flow is described by,

$$T(r) = C_1 I_0(m_f r) + C_2 K_0(m_f r) + \frac{g}{m_f^2 k} + T_\infty \quad 3.14$$

where  $I_0$  and  $K_0$  are the Bessel functions (Beck *et al.*, 1992). Since the temperature at  $r = 0$  is finite,  $C_2$  must be zero, and we are left with a boundary condition of the first kind,

$$T|_{r=b} = \text{constant} \quad 3.15$$

By applying this boundary condition to the general solution and solving for  $C_1$  we obtain,

$$T(r) = \frac{g}{m_f^2 k} \left[ 1 - \frac{I_0(m_f r)}{I_0(m_f b)} \right] + T_\infty \quad 3.16$$

which is the solution of the temperature distribution for radial heat flow with internal heat generation, natural convection from both front and back faces and a constant temperature boundary condition.

Each of the three derived expressions can be thought of as a mathematical tool which measures the thermal conductivity of a certain medium. In Chapter 4 we will determine which of these "tools" is most sensitive in its measurement and accurate in its estimation of the thermal conductivity of a doped diamond film.

## **Chapter 4**

### **Design of the Diamond Film Sample**

Perhaps the most important consideration for ensuring successful experimental results for the estimation of the thermal conductivity of CVD diamond films is the design of the sample. We have already encountered what adverse effects the silicon substrate can have on the results if it is not properly etched, but there are geometrical and electrical conditions of the sample that must also be addressed in order to optimize the experiment and ultimately improve the results. This chapter consists of two main parts of the design of the diamond film sample. The first part of the chapter deals with the analytical design and consists of discussions concerning relative error reduction, heating requirements and natural convection reduction. Out of this analytical analysis an optimum geometric and electrical design for the sample is chosen for the experiment. The second part of the chapter deals with the mechanical design of the sample. In this section, a diamond film sample is manufactured according to the optimum parameters calculated in the first part. Here the substrate preparation, diamond deposition, masking and etching processes are discussed.

## Analytical Design

### 4.1 Determining the Best Experimental Model

The first step towards designing the optimal diamond film sample is determining which model (one dimensional, two dimensional, or radial) has the smallest uncertainty in the estimation of the thermal conductivity. If the uncertainty of the relative temperature rise,  $\theta(r)$  ( $\theta(r) = T(r) - T_b$ ) at a particular location  $r$ , is dominated by the uncertainty of the thermal conductivity then,

$$w_\theta = \frac{\partial \theta(r)}{\partial k} w_k, \quad 4.1$$

where  $w_\theta$  and  $w_k$  are the uncertainties in the relative temperature distribution and the thermal conductivity, respectively (Holman, 1978). From this relationship, the relative uncertainty in the thermal conductivity becomes,

$$\frac{w_k}{k} = \frac{w_\theta}{\theta(r) \gamma(r)}, \quad 4.2$$

where

$$\gamma(r) = \frac{k \frac{\partial \theta(r)}{\partial k}}{\theta(r)} \quad 4.3$$

In this form we can concentrate on increasing the nondimensional sensitivity coefficient,  $\gamma(r)$ , to decrease the overall relative error in the measurement of the thermal conductivity,  $w_k$ .

In the following section,  $\gamma(0)$  for the three different models presented in Chapter 3 is calculated and plotted as a function of the characteristic length. Parameters such as

film thickness and temperature rise are also varied in these calculations to show their relative effect on the experimental error. At the end of this section,  $\gamma$  for all of the models is compared to determine which model yields the "best" estimation of the thermal conductivity.

*One Dimensional Model:*

In the one dimensional model we have the relative temperature distribution,

$$\theta(x) = \left[ (T_{si} - T_{\infty}) - \frac{g\delta}{2h} \right] \frac{\cosh(m_f x)}{\cosh(m_f L)} + \frac{g\delta}{2h}. \quad 4.4$$

Using equation 4.4 to calculate the non-dimensional sensitivity coefficient ( $\gamma$ ) evaluated at  $x = 0$  we get

$$\gamma(0) = \frac{k \frac{\partial \theta}{\partial k}}{\theta} \Big|_{x=0} = \frac{m_f L}{2} \frac{\tanh(m_f L)}{[\cosh(m_f L) - 1]} \quad 4.5$$

where

$$m_f = \sqrt{\frac{2h}{k\delta}}. \quad 4.6$$

The nondimensional sensitivity coefficient was evaluated at  $x=0$  to determine the sensitivity of the model to the measurement of the thermal conductivity where the temperature rise is the greatest. We can see from equations 4.5 and 4.6 that  $\gamma$  is a function of length (L), the thermal conductivity (k), the film thickness ( $\delta$ ) and the natural convection coefficient (h). In the following calculations of  $\gamma$ , the diamond thermal conductivity was set to  $k = 1000$  W/m K and the convection coefficient was determined

from the expression,

$$\bar{h} = \frac{(.68 + .67 R_a^{\frac{1}{4}})}{[1 + (\frac{.492}{Pr})^{\frac{9}{16}}]^{\frac{4}{9}}} \frac{k_a}{\ell} \quad 4.7$$

where  $k_a$  is the thermal conductivity of the surrounding air and  $\ell$  is the characteristic length ( $\ell = 2L$ ) of the sample. This expression describes the average natural convection coefficient for a vertical plate with an isothermal surface (Incropera, 1990).

To aid in the analysis of  $\gamma$  in the one dimensional case, program *ID* was written. By inputting the surface temperature of the diamond film, the surrounding temperature of the air, the thermal conductivity of the film ( $k_f$ ), the film thickness and a range for the characteristic length,  $\gamma$  as a function of the total length ( $\ell$ ) is calculated. The program allows for temperature dependent properties of the air and prompts the user when calibrations of these properties are extended beyond their range. The output generated by the program is displayed in Figures 4.1 and 4.2.

In Figure 4.1,  $\gamma$  is plotted as a function of the total length for the different film thicknesses of 5, 10 and 15  $\mu\text{m}$ .

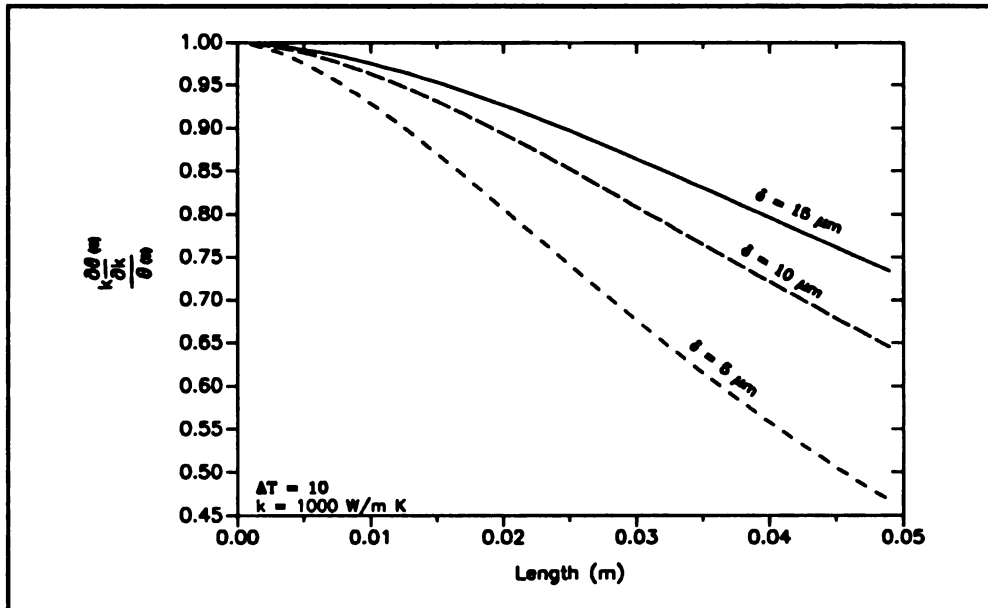


**Figure 4.1.** Nondimensional sensitivity coefficient as a function of characteristic length for different film thicknesses, 1D case.

For each of these curves the temperature difference between the surface of the sample at  $x=0$  and the surroundings was set to  $\Delta T = 10^\circ\text{C}$ . From Figure 4.1, we notice that the relative error increases with increasing length and decreases with increasing film thickness.

From equation 4.5, we see that  $\gamma$  is also a function of  $h = f(\Delta T)$ . Figure 4.2 displays  $\gamma$  as a function of length for different temperature differences.

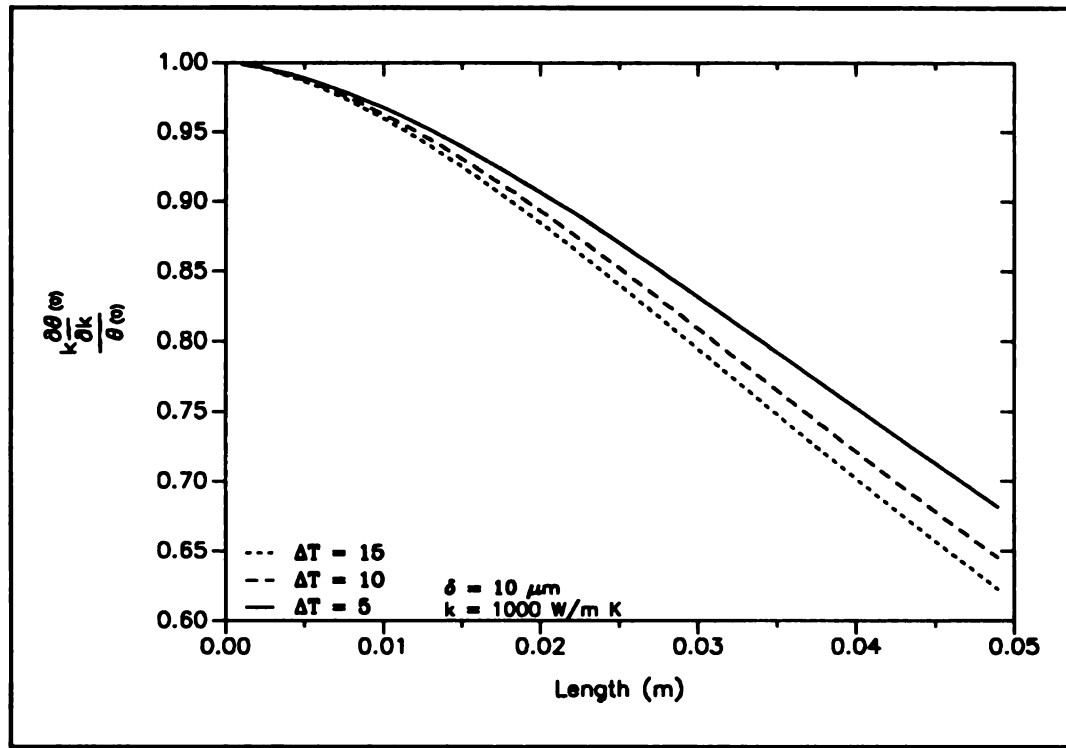


**Figure 4.2.** Nondimensional sensitivity coefficient vs. characteristic length for different temperature rises, 1D case.

The film thickness was held at  $10 \mu\text{m}$  while the temperature differences were set to 5, 10 and  $15 \text{ }^\circ\text{C}$ . Although at a given length the graph displays an decrease in  $\gamma$  with an increase in the temperature difference, we see that the relative error of the thermal conductivity is more sensitive to the film thickness than the relative temperature rise when comparing Figures 4.1 and 4.2.

*Two Dimensional Model:*

In the two dimensional model we have the relative temperature distribution,

$$\theta(x, y) = \frac{4g}{k} \sum_{m=1}^{\infty} \sum_{n=1}^{\infty} \frac{\cos(\beta_m \frac{x}{a}) \cos(\beta_n \frac{y}{b}) (-1)^{m-1} (-1)^{n-1}}{\beta_m \beta_n [(\frac{\beta_m}{a})^2 + (\frac{\beta_n}{b})^2 + m_f^2]} \quad 4.8$$

Evaluating this expression at  $x = 0$  and  $y = 0$ ,

$$\gamma(0, 0) = \sum_{m=1}^{\infty} \sum_{n=1}^{\infty} \left[ 1 - \frac{m_f^2}{[(\frac{\beta_m}{a})^2 + (\frac{\beta_n}{b})^2 + m_f^2]} \right] \quad 4.9$$

The nondimensional sensitivity coefficient is determined at (0,0) because it is at this location where the relative temperature rise is at its peak and the radiometer's signal-to-noise ratio is maximized. We can see from equation 4.9 that  $\gamma$  is a function of the characteristic length (a), the characteristic width (b) and  $m_f$ . The fin term,  $m_f$ , is dependent on the thermal conductivity (k), film thickness ( $\delta$ ) and the natural convection coefficient (h), (refer to equation 4.6). To aid in the analysis of  $\gamma$  in the two dimensional case, program 2D was written. After inputting the surface and surrounding temperatures, the thermal conductivity, the film thickness and a range for the characteristic length (l), where  $l = 2a$  and the length and width are equal,  $\gamma$  is calculated for the two dimensional case as a function of the total length. The program also allows for temperature dependent properties of air.

By calculating  $\gamma$  as a function of length for different film thicknesses, we see the

same behavior as in the one dimensional case.

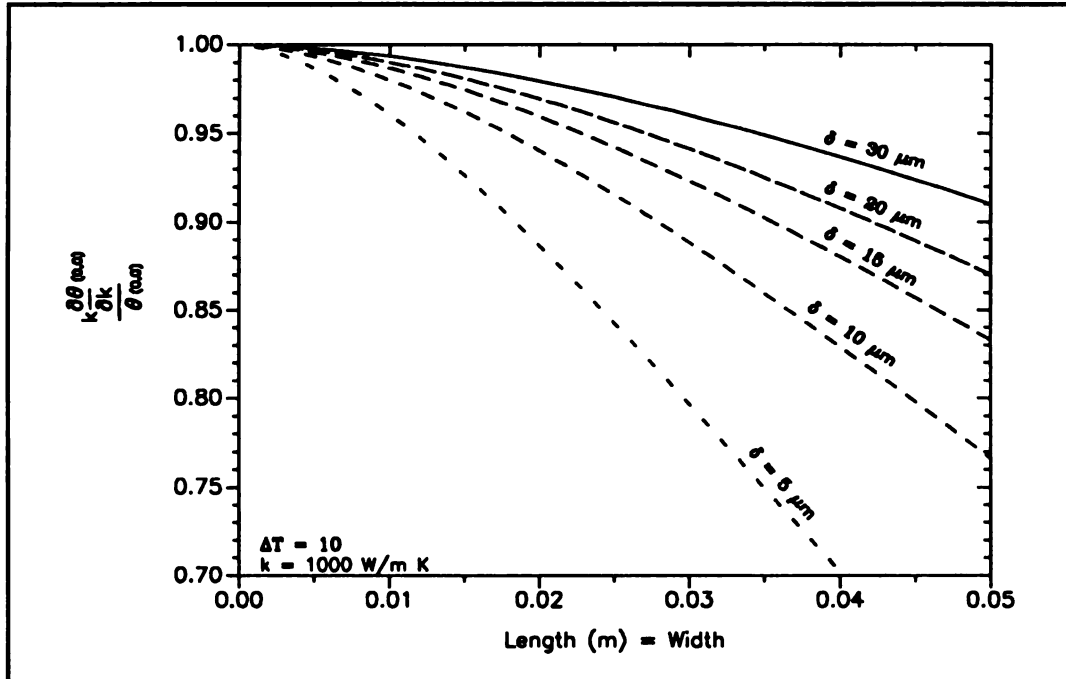


**Figure 4.3.** Nondimensional sensitivity coefficient vs. characteristic length for different film thicknesses, 2D case.

Again, the relative error of the estimated thermal conductivity increases with increasing length and decreases with increasing thickness. Figure 4.3 also shows that increasing  $\gamma$  by increasing the film thickness becomes more challenging for thicker samples. By increasing the thickness from 5  $\mu\text{m}$  to 10  $\mu\text{m}$  at a length of 4 cm, we increase  $\gamma$  by 0.12. However, if the film thickness is increased from 20  $\mu\text{m}$  to 30  $\mu\text{m}$ , a 10  $\mu\text{m}$  difference, we only increase the value of  $\gamma$  by a mere 0.03. This information is beneficial in designing an optimal experimental sample having a relatively thin diamond film while keeping

diamond deposition time to a minimum.

The  $\gamma$  values here corresponding to the same film thickness and  $\Delta T$  are greater than the one dimensional case. A comparison of  $\gamma$  for both the one and two dimensional models is presented in Figure 4.4.

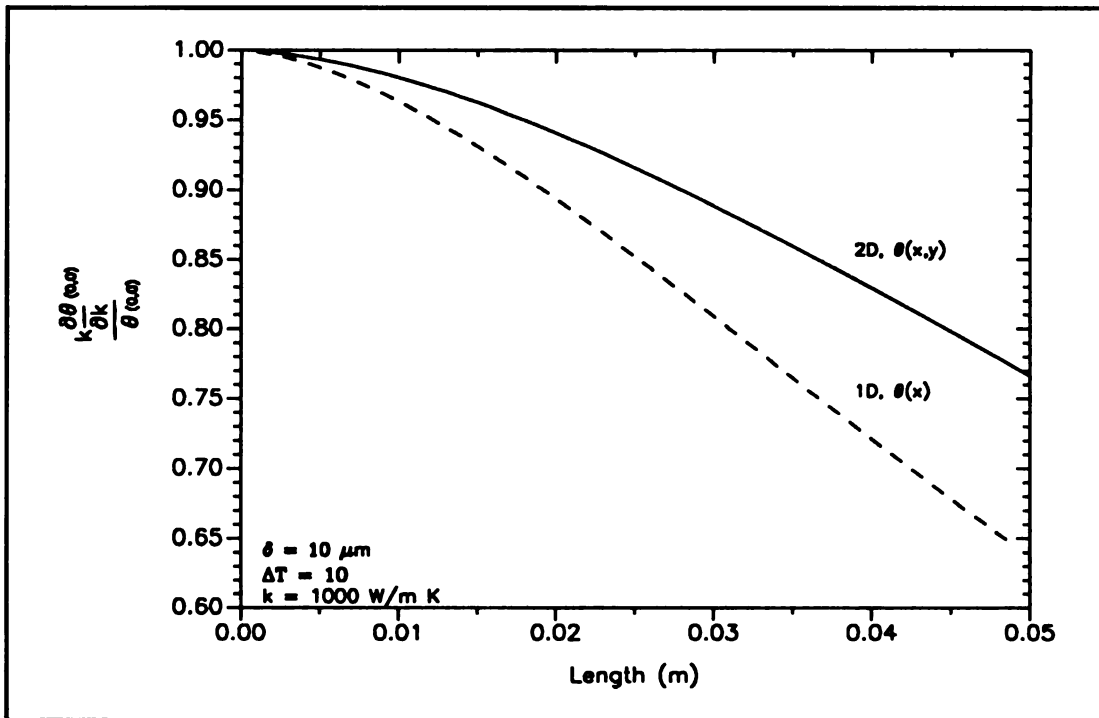


**Figure 4.4.** Comparison of the nondimensional sensitivity coefficient for the one dimensional and two dimensional cases at the same characteristic length.

We can see from Figure 4.4 that the relative error in the estimation of the thermal conductivity is consistently higher in the one dimensional experiment than in the two dimensional experiment. At  $l = 5$  cm and  $\delta = 10$   $\mu$ m,  $\gamma(0,0)$  for the two dimensional model is approximately 0.76 where  $\gamma(0)$  for the one dimensional model corresponding to the same length is only 0.64.

Figure 4.5 is a plot of  $\gamma$  as a function of length for different temperature differences in the two dimensional case.

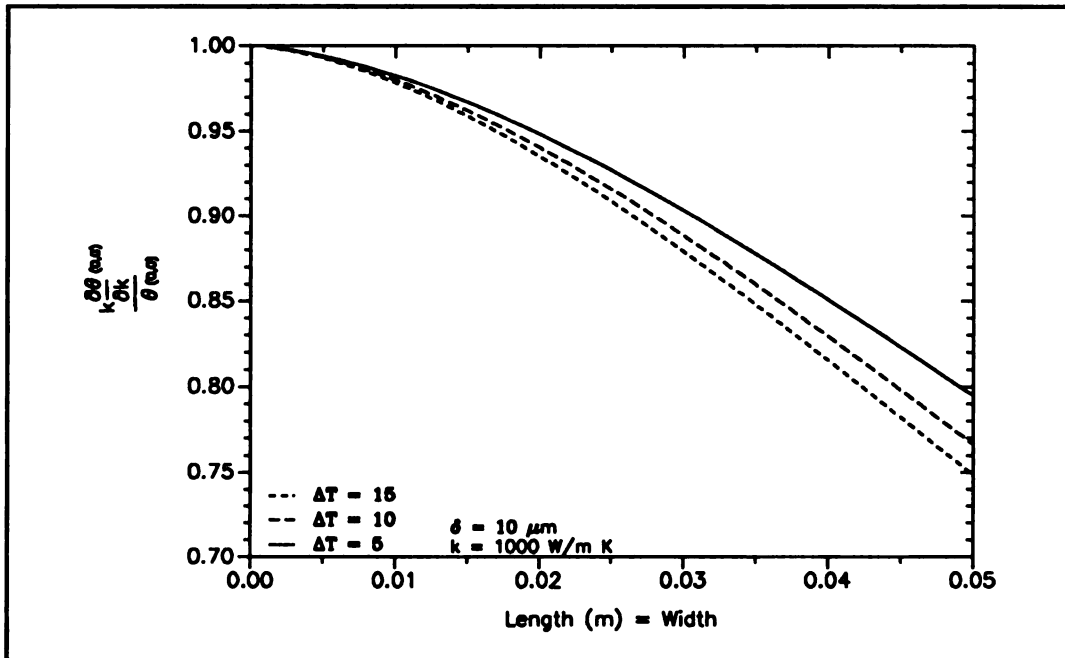


**Figure 4.5.** Nondimensional sensitivity coefficient vs. characteristic length for different temperature rises, 2D case.

We can see here that  $\gamma$ , as in the one dimensional model, is not as sensitive to the temperature rise as compared to a change in the film thickness. In fact, for lengths of approximately .01 m or less the change in  $\gamma$  with respect to the steady state temperature difference is almost negligible.

Since the analysis has dealt with a square sample, it is interesting to determine if there is a better rectangular geometry that would improve the estimates of  $k$  or if there is a geometrical arrangement we should avoid altogether. Figure 4.6 is a plot of  $\gamma$  as a

function of the characteristic length for different sample widths (1.0, 0.5 and 0.25 cm).

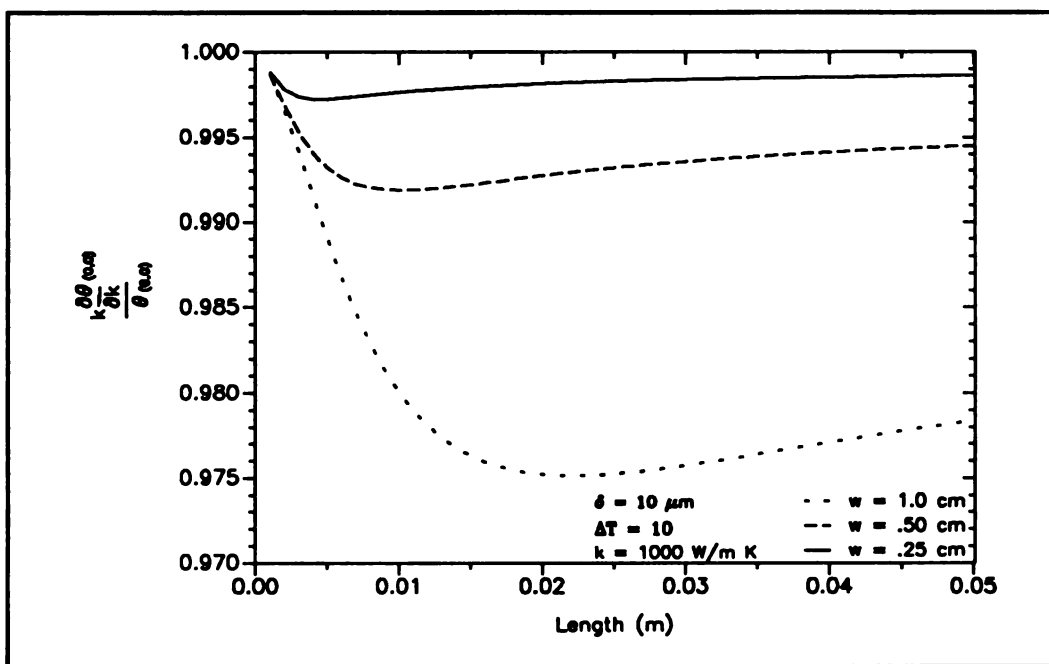


Figure 4.6. Nondimensional sensitivity coefficient vs. characteristic length for different sample widths of 1.0, 0.50 and 0.25 cm, 2D case.

By holding the widths constant we see that all three curves have a minimum value for  $\gamma(0,0)$  where the total length equals twice the total width ( $a \approx 2b$ ). Although all of the values for  $\gamma$  are above 0.975 for  $\delta = 10 \mu\text{m}$ ,  $\Delta T = 10$  and  $k = 1000 \text{ W/m K}$ , this geometrical ratio should probably be avoided when designing a diamond film sample for this two dimensional model. For it is this ratio,  $a/b \approx 2$ , where the relative error in the estimation of the thermal conductivity is greatest.

**Radial Model:**

In the one dimensional radial model the relative temperature distribution is described by the expression

$$\theta(r) = \frac{g}{m_f^2 k} \left[ 1 - \frac{I_0(m_f r)}{I_0(m_f b)} \right] \quad 4.10$$

Evaluating this expression at  $r = 0$ ,

$$\gamma(0) = \frac{m_f b}{2} \left[ \frac{I_1(m_f b)}{I_0(m_f b)^2 - I_0(m_f b)} \right] \quad 4.11$$

where  $b$  is the radius of the sample. As in the one dimensional and two dimensional analyses, a computer program was written for calculating  $\gamma(0)$  for the radial case. Program *RAD* was written using the Student version of Matlab. Matlab was used in this case due to its ability to quickly and easily evaluate  $I_0$  and  $I_1$  Bessel functions. *RAD* uses the same input values of film thickness, steady state temperature difference, and thermal conductivity as in the one and two dimensional cases, but prompts the user for the diameter of the sample which is the characteristic length.

In Figure 4.7,  $\gamma(0)$  is again plotted as a function of the characteristic length (diameter) for different film thicknesses.

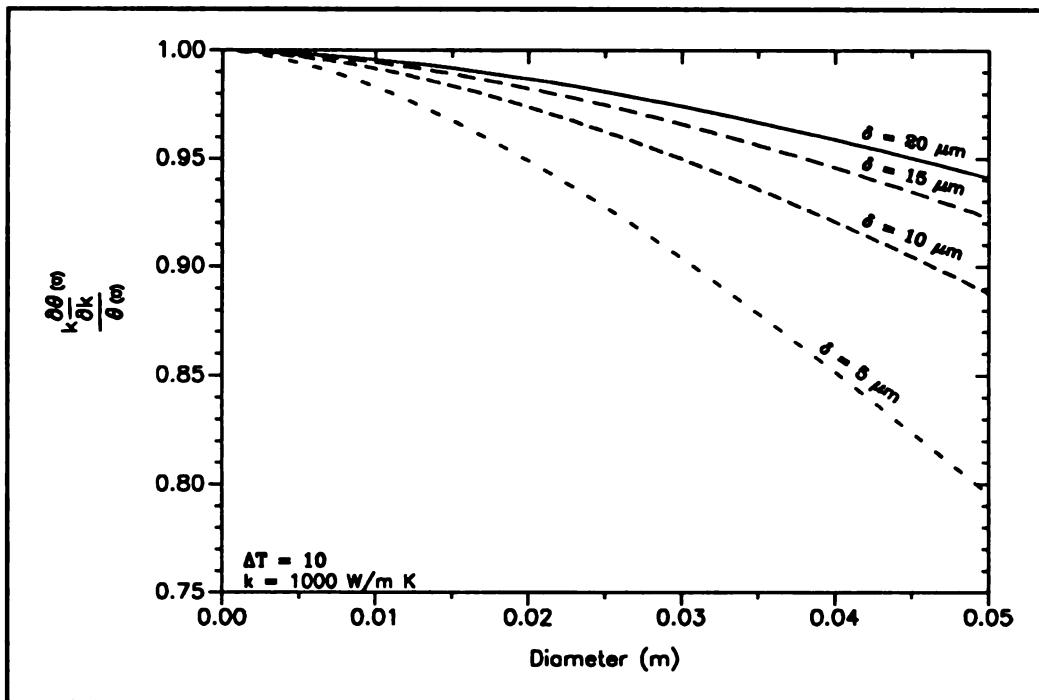


**Figure 4.7.** Nondimensional sensitivity coefficient vs. diameter for different film thicknesses, radial case.

We can see from the results in Figure 4.7 that  $\gamma(0)$  behaves in much the same way as in the one and two dimensional cases. Values for  $\gamma(0)$  decrease with increasing diameter but increase with increasing sample thickness.

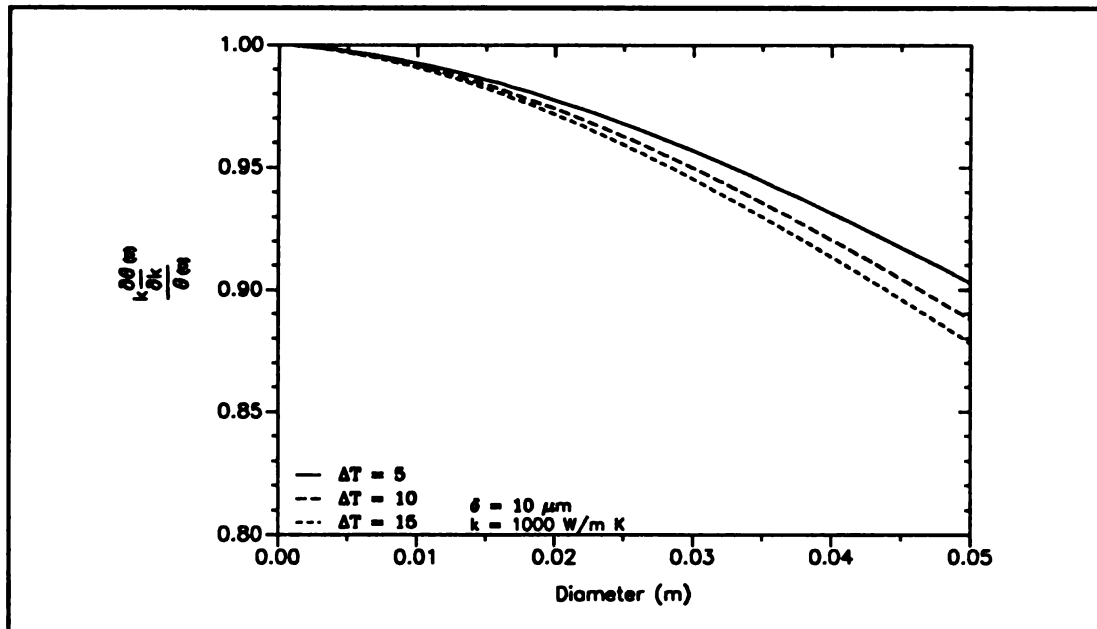


Figure 4.8. Nondimensional sensitivity coefficient vs. diameter for different temperature rises, radial case.

Figure 4.8 shows again that even for the radial case that  $\gamma(0)$  is more sensitive to the film thickness than the steady state temperature difference,  $\Delta T$ . The temperature difference again has little effect on the relative error of the experiment for diameters of approximately .01 m or less.

In order to choose the experimental design of the sample which would most limit the relative error of the estimation of the thermal conductivity,  $\gamma(0)$  versus the characteristic length for all three cases (one dimensional, two dimensional and radial) is compared at a film thickness of 10  $\mu\text{m}$ , a  $\Delta T$  of 10  $^{\circ}\text{C}$  and a thermal conductivity of 1000 W/m K. These parameter values were chosen to simulate actual experimental conditions.

The plot for all three cases can be seen in Figure 4.9.

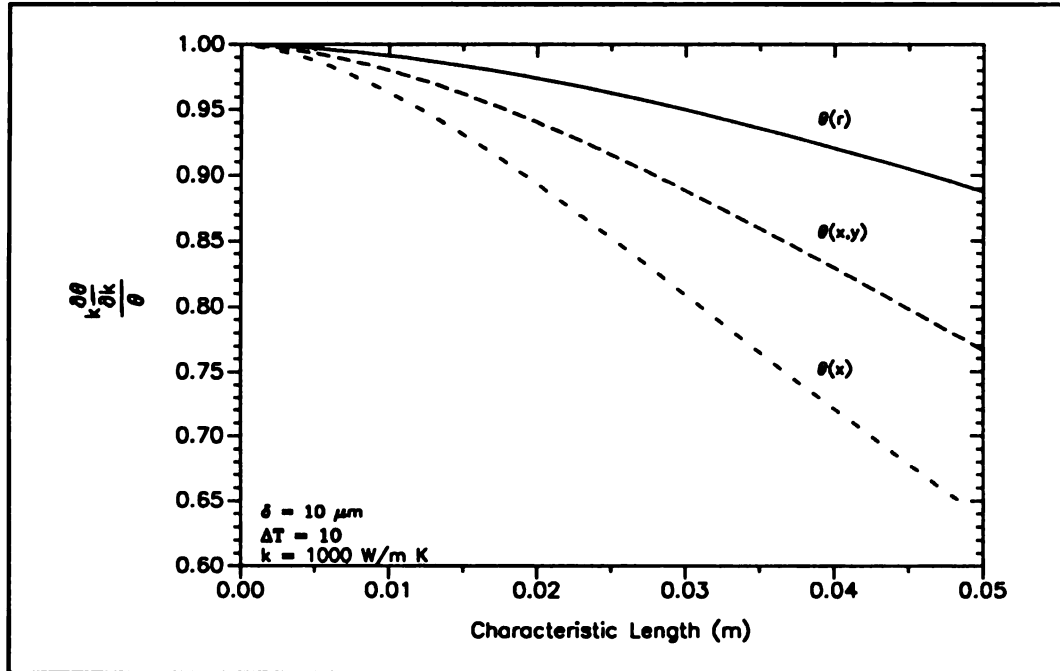


Figure 4.9. Comparison of the nondimensional sensitivity coefficient vs. characteristic length for 1D, 2D and radial cases.

We can see that  $\gamma(0)$  for the radial model is consistently higher than both the one dimensional case and the two dimensional case. From this analysis using the nondimensionalized sensitivity coefficient,  $\gamma(0)$ , we have determined that the radial model will produce the most accurate experiment for the determination of the thermal conductivity.

## 4.2 Special Requirements for the Desired Temperature Rise

Now that we have determined the "best" analytical model for the experiment, we must deal with some special heating requirements for the diamond film. Due to diamond's unique semiconduction capabilities (in its doped state), we are able to use electrical resistive heating within the doped film to create the necessary temperature gradient. However, in using internal heat generation within the film we must be certain that 1) there is volumetric heat generation in only the diamond film region and 2) the electrical resistivity of the film is low enough so the film can be heated with the available power supply.

### 4.2.1 Volumetric Heat Generation in Diamond

Since diamond is deposited on a silicon substrate during the manufacturing process, we must be certain that as we try to heat the diamond film the electrical current does not leak into the silicon which also conducts electricity. If there is not electrical insulation between the two semiconducting layers, substantial error in quantifying the volumetric heat generation within the diamond film will occur. If the electrical leakage is substantial, there could even be volumetric heat generation within the silicon itself, completely invalidating the experimental results.

To combat this problem, a thin layer of  $\text{SiO}_2$  is commonly deposited on top of the silicon substrate. The  $\text{SiO}_2$ , an electrical nonconductor, acts as an insulating medium between the deposited diamond and the silicon substrate. A diagram of a sample with the additional layer of  $\text{SiO}_2$  is displayed in Figure 4.10.

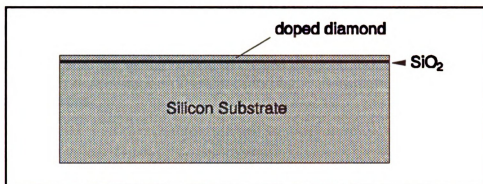


**Figure 4.10.** Diagram of sample with a doped diamond film, a layer of SiO<sub>2</sub> and a silicon substrate.

However, this substrate alone cannot always provide adequate electrical insulation when the silicon is etched from the backside. The etchant chemical which is used to dissolve the silicon can settle between the silicon and diamond layers destroying the thin SiO<sub>2</sub> layer. So, in order to ensure electrical insulation, a thin layer of undoped (electrically nonconductive) diamond is deposited first on top of the SiO<sub>2</sub> layer. A diagram of this type of sample can be seen in Figure 4.11.

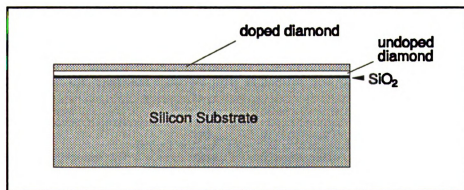


**Figure 4.11.** Schematic of sample with doped and undoped diamond films, a layer of SiO<sub>2</sub> and a silicon substrate.

Since diamond is impermeable to the etchant, the undoped layer provides a solid electrically nonconductive medium between the doped diamond region and the silicon substrate. We would like to have the undoped layer as thin as possible ( $\approx 1 \mu\text{m}$ ) because this layer can limit our ability to heat the doped diamond film and it may have different thermal properties.

#### 4.2.2 Doping Requirements for the Diamond

In order to allow for the internal heat generation necessary to heat the diamond, we must dope the diamond film with boron to obtain a certain electrical resistivity. The electrical resistivity is inversely proportional to the level of boron added before the diamond deposition process. If the resistivity is too high then the available power supply (120 volts, 1.5 amps) will be insufficient in generating the necessary power to heat the film. In addition, the resistivity must be low enough to compensate for the heat sink behavior that the undoped diamond layer will have. We need to avoid a situation in which the undoped layer of diamond dissipates all of the heat generated in the doped layer and creates a uniform temperature distribution across the surface of the film.

Currently, the Microstructures Laboratory which makes these diamond samples can manufacture films having a resistivity ( $\rho$ ) of  $0.5 \Omega\text{-cm}$ . To see if this resistivity is sufficient to heat the diamond film we turn to the revised solution of the radial model

$$\theta(r) = \frac{g\delta_d}{2h} \left[ 1 - \frac{I_o(m_{eff}r)}{I_o(m_{eff}b)} \right] \quad 4.12$$

where

$$m_{eff} = \sqrt{\frac{2h}{k(\delta_d + \delta_u)}} \quad 4.13$$

and  $\delta_d$  and  $\delta_u$  are the thicknesses of the doped and undoped diamond layers, respectively. Evaluating this solution at  $r = 0$ , we find the relative temperature rise at the center of the exposed diamond to be

$$\theta(0) = \frac{g\delta_d}{2h} \left[ 1 - \frac{1}{I_0(m_{eff}b)} \right] \quad 4.14$$

The volumetric heat generation ( $g$ ) is equivalent to electrical power per unit volume and is calculated from the expression,

$$g = \frac{V^2}{(R * Volume)} \quad 4.15$$

where  $V$  is the applied voltage and  $R$  is the electrical resistance. To obtain uniform heat generation we use the electrical circuit displayed in Figure 4.12 where  $V$  and  $L$  correspond to the applied voltage and the length of the circuit, respectively.

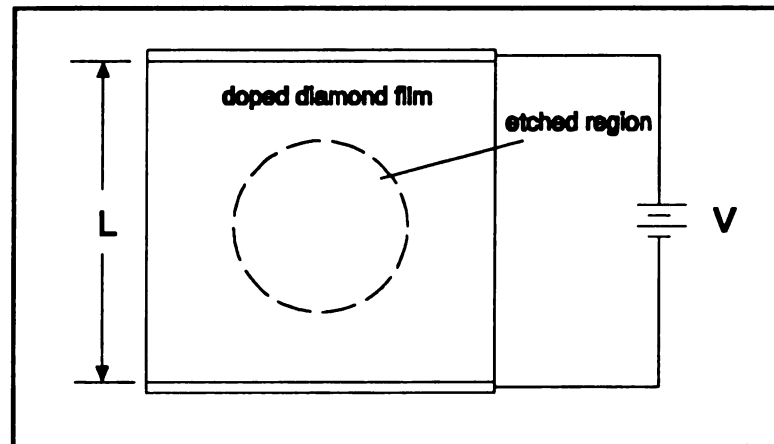


**Figure 4.12.** Schematic of the electrical circuit.

The electrical resistance in this case is defined as,

$$R = \frac{\rho L}{A_c}, \quad 4.16$$

where  $\rho$  is the resistivity of the film and  $A_c$  is the cross sectional area of the doped film. Substituting equations 4.15 and 4.16 into equation 4.14, we develop the relationship between the applied voltage, the electrical resistivity of the film and the relative temperature rise to be,

$$\theta = \frac{V^2 \delta_a \left[ 1 - \frac{1}{I_o (m_{eff} b)} \right]}{2 h \rho L^2} \quad 4.17$$

where  $L$  is the distance the current travels in the circuit ( $L \geq$  diameter of the etched region). This relationship is useful in pre-determining the temperature range of the experiment according to the sample's geometry, resistivity and the available electrical power. The relative temperature rise,  $\theta$ , is calculated as a function of voltage with the resistivity set to 0.5  $\Omega$ -cm, a circuit length of 2 cm, and the diameter of the etched region fixed at 1 cm. The results are presented in Figure 4.13.

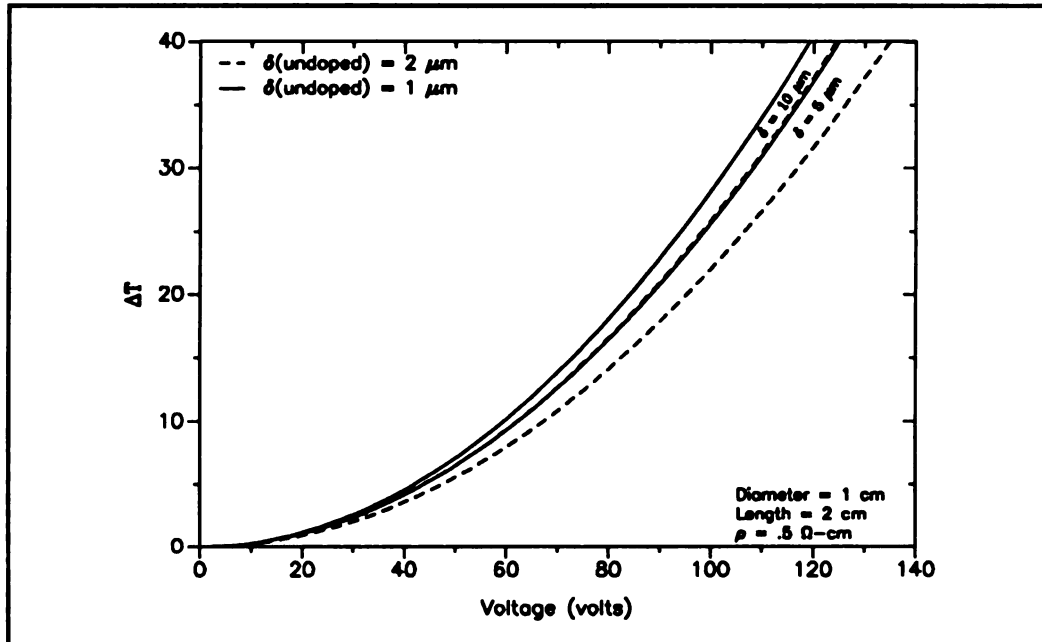


**Figure 4.13.** Temperature rise as a function of applied voltage for different film thicknesses.

The four curves in Figure 4.13 represent the voltage requirements for heating films with doped thicknesses of 5 and 10  $\mu\text{m}$  and undoped thicknesses of 1 and 2  $\mu\text{m}$ . Although limited to 120 dc volts for the applied voltage, this prediction indicates that we can achieve approximately a 40  $^{\circ}\text{C}$  temperature rise with a sample having a doped thickness of 10  $\mu\text{m}$  and a thermal conductivity of 1000 W/m K. Likewise, a 30  $^{\circ}\text{C}$  temperature rise can be reached having doped and undoped film thicknesses of 5 and 1  $\mu\text{m}$ , respectively. It is interesting to note that the heating requirements for the  $\delta_d = 10 \mu\text{m}$ ,  $\delta_u = 2 \mu\text{m}$  and the  $\delta_d = 5 \mu\text{m}$  and  $\delta_u = 1 \mu\text{m}$  cases are nearly the same. This is to be expected since the ratio of the 2 layers in each case is 5:1. Therefore, if the highest doping level is used,

a Hall concentration of  $9.6 \times 10^{18} \text{ cm}^{-3}$  resulting in a resistivity of  $0.5 \text{ } \Omega\text{-cm}$  at 300 K, the heating requirements for the doped diamond film should be adequate to achieve the goals of the experiment, even with the addition of the undoped layer of diamond.

### 4.3 Limiting Natural Convection

In most of the previous works dealing with the measurement of the thermal properties of CVD diamond films listed in Chapter 2, natural convection was addressed as a source of uncertainty in the experimental setup. Because natural convection is another form of heat transfer (other than conduction), it can pose serious problems to the estimation of the thermal conductivity if it is not limited. Figure 4.14 is a plot of  $\gamma(0)$  versus the product of the fin term  $m_f$  and the characteristic length for the three models discussed in Chapter 3. This product is a nondimensional parameter that relates to the amount of heat lost by convection.

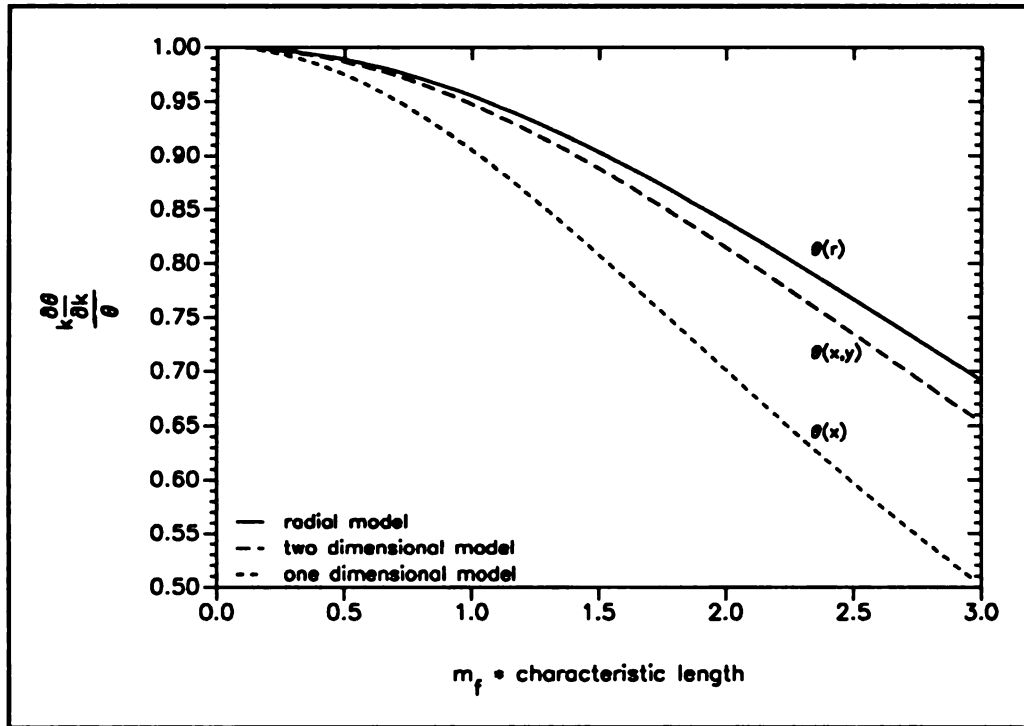


Figure 4.14. Nondimensional sensitivity coefficient vs. ( $m_f$ \*characteristic length) for the 1D, 2D, and radial cases.

We can see from Figure 4.14 that as convection becomes more dominant the relative error in the thermal conductivity increases. Not only can the error in the estimated thermal conductivity be high but errors in the calculation of the convection coefficient can also be significant.

Since the natural convection coefficient must be calculated from position and temperature dependent empirical expressions, values tend to represent approximations rather than exact quantities. In light of this, some engineers and physicists have designed

vacuum chambers in an attempt to negate the effects of natural convection. Theoretically, a perfect vacuum would indeed negate convection. However, practically, a vacuum chamber presents additional experimental challenges; one of which is the design of the chamber itself. Additional instruments, measurements and seals around electrical lead wires and other openings only add to the experimental difficulty. In many cases the vacuum chamber can prove to be more of an experimental inconvenience rather than an aid.

Since good vacuum chambers are either time consuming to build or expensive to buy, one of the goals of the present work was to design an experimental setup which was simple, effective and did not require the use of a vacuum chamber to minimize natural convection. In order to do this, however, we must properly choose the geometry of the sample. We see from Figure 4.14 that by decreasing the characteristic length we decrease natural convection. Recall that the convection heat transfer is proportional to the surface area. By comparing the surface areas for the two dimensional and the radial cases, we see that the characteristic lengths are related by  $\pi/4 D^2 = L^2$ , where L is the length of the two dimensional sample and D is the diameter of the radial sample. Since the characteristic lengths are set equal in Figure 4.14 the radial curve and the two dimensional curve become separated by a factor of  $(\pi/4)^{1/2} \approx 0.9$ .

In order to quantify the relative amount of heat lost by natural convection compared to the volumetric heat generation we again turn to the mathematical model for the radial case

$$\frac{1}{r} \frac{d}{dr} \left( r \frac{d\theta}{dr} \right) - \frac{2h}{k(\delta_d + \delta_u)} \theta + \frac{g\delta_d}{k(\delta_d + \delta_u)} = 0 \quad 4.18$$

which now includes the thin layer of undoped diamond ( $\delta_u$ ); the solution is described by equation 4.12. If we divide the governing differential equation, equation 4.18, by  $[g\delta_d/k(\delta_d+\delta_u)]$ , the nondimensional convection term becomes  $[-2h\theta/g\delta_d]$ . This parameter represents the percentage of the total heat generated which is lost to natural convection. Substituting equation 4.14 into the nondimensional convective term,  $[-2h\theta/g\delta_d]$ , we get

$$\left| \frac{2h\theta(0)}{g\delta_d} \right| = 1 - \frac{1}{I_o(m_{eff}b)} \quad 4.19$$

We again evaluate  $\theta$  at  $r=0$  since it is at this center location where the temperature rise is greatest. A plot of this parameter as a function of the sample diameter at different film thicknesses is presented in Figure 4.15.

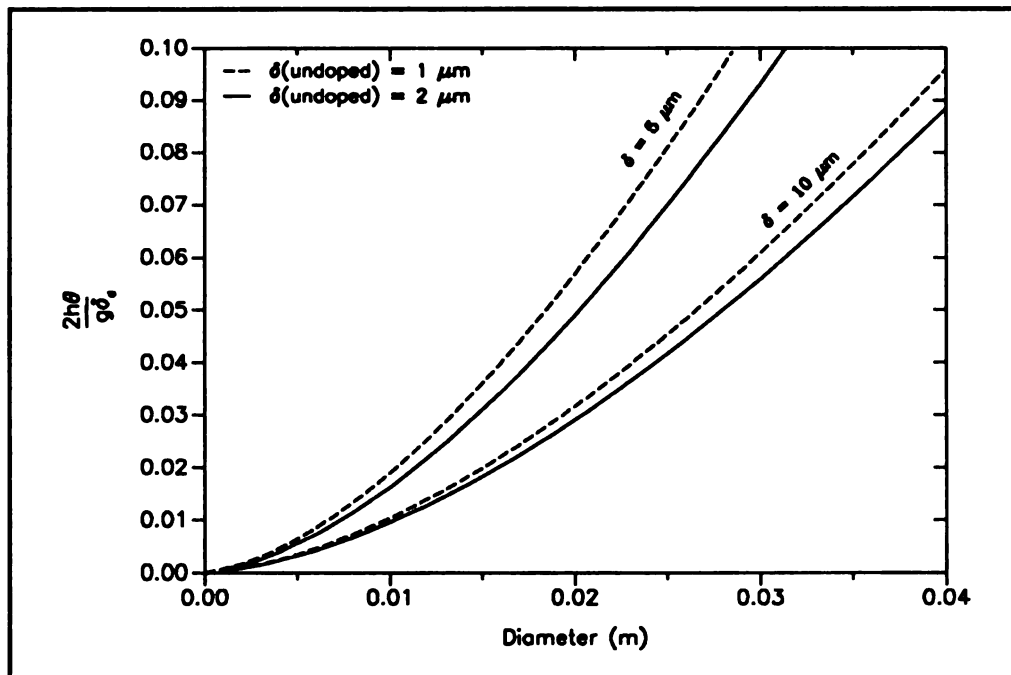


**Figure 4.15.** Ratio of natural convection to the total heat generated in doped film vs. diameter for different film thicknesses.

We can see from Figure 4.15 that with  $\delta_d = 10 \mu\text{m}$ , convection contributes approximately 1% of the total heat dissipated assuming a sample diameter of 1 cm and a thermal conductivity of 1000 W/m K. Likewise, when  $\delta_d = 5 \mu\text{m}$  convection contributes just under 2% of the heat loss. In addition, we also see that the undoped layer of diamond decreases the effects of natural convection.

Before choosing a geometry for the sample, we need to once again calculate  $\gamma(0)$  as a function of the diameter for different film thicknesses (mainly 10 and 5  $\mu\text{m}$ ) to see the effects the undoped diamond layer has on the relative error. The nondimensional sensitivity coefficient for doped thicknesses of 10  $\mu\text{m}$  and 5  $\mu\text{m}$  and undoped thicknesses of 1  $\mu\text{m}$  and 2  $\mu\text{m}$  as a function of diameter is presented in Figure 4.16.

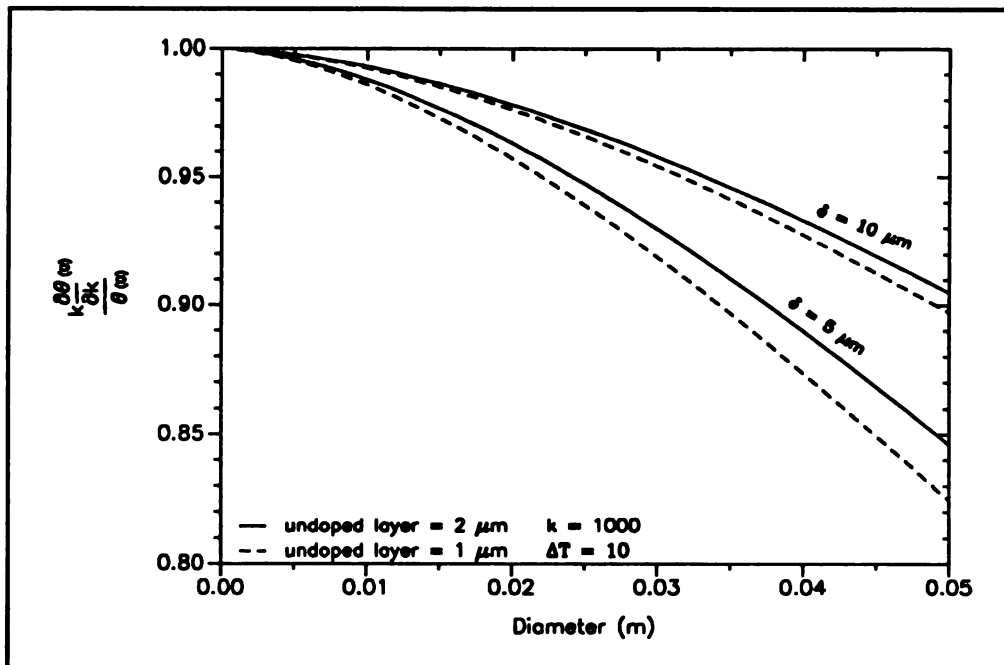


Figure 4.16. Nondimensional sensitivity coefficient vs. diameter for different doped and undoped film thicknesses.

Although the undoped layer of diamond decreases our relative temperature rise, we see from the results of Figure 4.16 that the undoped layer of diamond can also help decrease the error in the estimation of the thermal conductivity. However if the thickness of the undoped film is relatively large compared to the doped film the estimated thermal conductivity will be indicative of the undoped region not the doped, a situation that we want to avoid.

#### 4.4 Analytical Results

From the results of the analytical analysis presented in this section we can choose specific geometrical and electrical parameters for the design of the diamond sample that will optimize the radial experiment.

A diameter of approximately 1 cm is a desirable characteristic length because the relative error is little-affected by both the relative temperature rise and the thickness of the doped film in this region. This diameter is also advantageous since the infrared scanner will have no problem imaging an object of this size.

A Hall concentration of  $9.6 \times 10^{18} \text{ cm}^{-3}$  resulting in the resistivity ( $\rho$ ) of  $0.5 \text{ } \Omega\text{-cm}$  is a suitable doping level to create a temperature rise of 30–40 °C, depending upon the actual thicknesses of the doped and undoped layers. It is recommended that the resistivity not exceed  $1 \text{ } \Omega\text{-cm}$  for film thicknesses on the order of  $10 \text{ } \mu\text{m}$  if using a 120 v, 1.5 Amp power supply. For higher film resistivities, the power supply may be unable to heat the sample.

Although the results become better as the thickness of the doped layer increases, reasonable values for  $\delta_d$  range from 5–10  $\mu\text{m}$ . This is due to the slow deposition rate of

the current hot-filament deposition chamber in the Microstructures Laboratory. However, in this range, convection adds up to only 2% of the total heat dissipated for the worst case ( $\delta_d = 5 \mu\text{m}$ ,  $\delta_u = 1 \mu\text{m}$ ) and the nondimensional sensitivity coefficient,  $\gamma(0)$ , is at a high value of 0.985.

An undoped diamond layer between 1-2  $\mu\text{m}$  is also suggested by the analysis. This is the range at which the film surface becomes continuous. A continuous layer is essential in ensuring electrical insulation between the two semiconducting media. The undoped layer of diamond should not only allow for an adequate temperature rise but should also help reduce the relative error and the natural convection in the experiment.

diameter of exposed diamond	$\leq 1 \text{ cm}$
thickness of doped diamond layer ( $\delta_d$ )	5-10 $\mu\text{m}$
thickness of undoped diamond layer ( $\delta_u$ )	1-2 $\mu\text{m}$
resistivity of doped region ( $\rho$ )	$\leq 1.0 \Omega\text{-cm}$

**Table 4.1.** Optimum sample design parameters

These results are determined from assuming a thermal conductivity of 1000 W/m K.

### **Mechanical Design**

This section describes specialized design techniques utilized by the Microstructures Laboratory at Michigan State University's Research Complex to fabricate diamond samples described by the results of the preceding analytical analysis. The design of the

diamond sample itself consists of two main parts, the topside fabrication of the doped and undoped layers of diamond and the bottomside fabrication of the patterned diamond mask.

#### **4.5 Topside Fabrication**

Before diamond can be deposited on either side of the substrate, the supporting silicon wafer must be carefully prepared and cleaned. The wafer, approximately 450  $\mu\text{m}$  thick, with a thin layer of  $\text{SiO}_2$  on top is first cut to a 2 x 2  $\text{cm}^2$  square. The square is cleaned thoroughly using pure acetone and then methanol, rinsed with distilled water and then dried with nitrogen gas.

With the wafer properly cut and cleaned, a solution known as photoresist is applied to the top surface of the  $\text{SiO}_2$ . This solution is applied by spinning the wafer in a rotation machine. If the surface of the wafer is free of debris then photoresist can be evenly distributed across the surface. The sample is then placed in an oven set at a temperature of about 400  $^\circ\text{C}$  for approximately 30 min. in order for the photoresist to adhere to the  $\text{SiO}_2$ . The application of the photoresist is an important factor in the success of the diamond deposition since it is this solution in which the diamond powder and other elements necessary to grow the diamond crystals are present.

Upon completion of the substrate preparation, the diamond film fabrication process for the topside is commenced. The sample is placed in a container known as the deposition chamber. This chamber contains the electrical filaments which heat the sample and the necessary carbon-enriched gas mixtures for deposition. A picture of the deposition chamber is shown in Figure 4.17.



Figure 4.17. A photograph of the hot filament CVD diamond deposition chamber.

The sample rests inside the deposition chamber on a platform several inches below the heating filaments. The chamber is then closed and vacuum is applied so that the quantity of the gases can be carefully regulated once the process is activated. With the gases pumped out of the chamber, the power is switched on such that there is approximately 4 mA of current flowing through each of the six filaments which are connected in parallel. As the filaments begin to heat up the surface of the sample, hydrogen gas is injected into the chamber for approximately 3 min so the surface of the photoresist can be cleaned. When the pressure is less than 10 mtorr in the deposition chamber, the gas valves controlling the flow of the carbon enriched gases ( $\text{CH}_4$ ,  $\text{C}_2\text{H}_2$  and  $\text{CO}$ ) are then

opened. As the filament temperature reaches 2000 °C, the carbon from the injected gases begins to deposit on the crystals already present in the photoresist. As the carbon crystals grow in size and begin to fill in throughout the surface of the substrate, a continuous layer of diamond eventually results. Due to the grain size of the crystals and the fill-in pattern on the surface of the substrate, the film becomes continuous between thicknesses of 1 and 2  $\mu\text{m}$ . With a growth rate of only 0.25  $\mu\text{m/hr}$ , the process of fabricating the undoped layer of diamond lasts approximately four hours.

The thickness of the undoped layer for both samples was measured with a scanning electron microscope (SEM). Measurements were taken along the plane parallel to the film surface to determine the thickness of this layer. In the graphs generated by the SEM, Figures 4.18-4.21, the x axis is in units of  $\mu\text{m}$  and the y axis is in angstroms ( $\text{\AA}$ ),  $10^{-10}$  m.

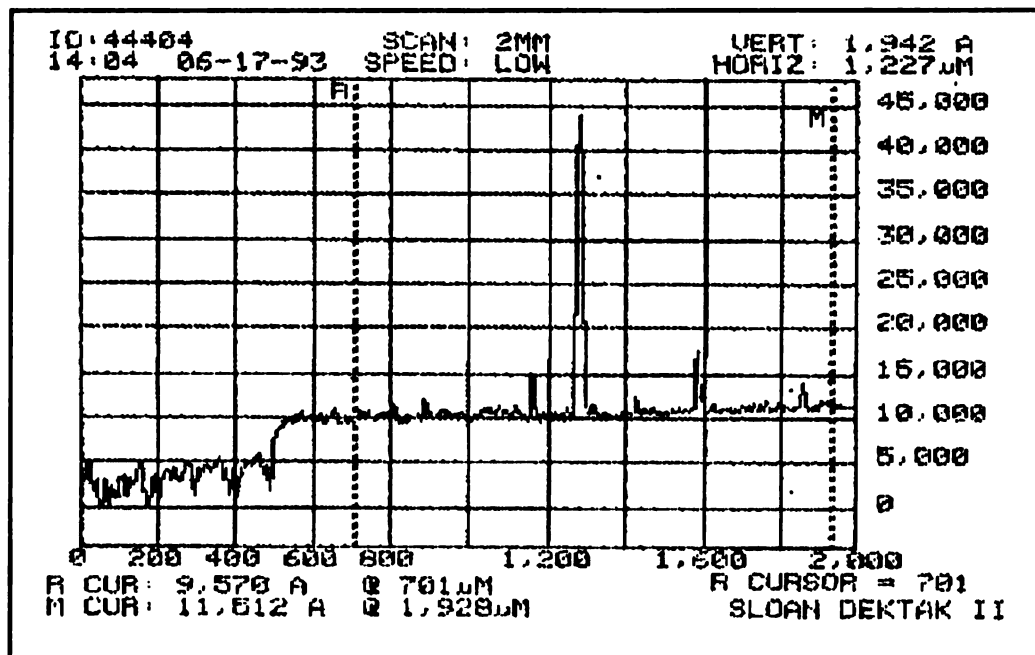


Figure 4.18. Thickness of the undoped diamond film on sample A measured in  $\text{\AA}$  by the SEM.

We see from this measurement that the undoped film on sample A has a continuous layer approximately  $10,000 \text{ \AA}$  ( $1.0 \text{ \mu m}$ ) thick. The large peak near the center of the graph is due to small debris, probably dust particles.

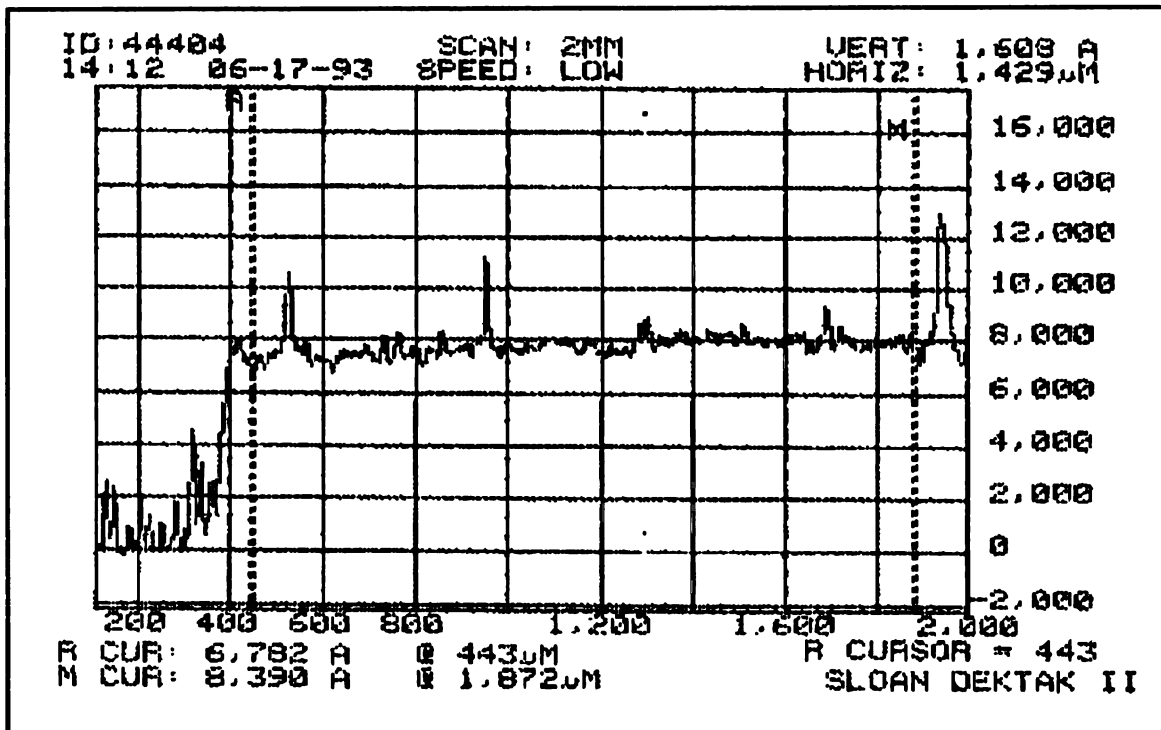


Figure 4.19. Thickness of the undoped diamond film on sample B measured in  $\text{\AA}$  by the SEM.

Figure 4.19 is a measurement of the undoped layer of sample B where the thickness of the undoped layer of diamond is approximately  $8,000 \text{ \AA}$  ( $0.8 \text{ \mu m}$ ).

With the undoped layer approximately  $1 \text{ \mu m}$  thick for each sample and by checking

the electrical resistance of the films we can conclude that the undoped diamond films are sufficient in providing the necessary electrical insulation from the silicon substrate.

With the first layer completed, the process is stopped and preparations begin to fabricate the doped diamond layer. After the sample has cooled, a boron holder is subsequently placed on the surface of the film, directly under the filaments. The holder is in a honeycomb configuration, housing many openings where the boron powder is added. By filling all of the holes in this holder, the highest available doping level for the doped layer is achieved. After the holder is filled, the deposition process is again repeated. However, in order to ensure uniform doping throughout the film, the film is redoped for every 4  $\mu\text{m}$  of growth.

After approximately 10 hours of deposition, the process is terminated and the thicknesses are again measured using the SEM. Figures 4.20 and 4.21 are SEM measurements of the doped films for both samples.

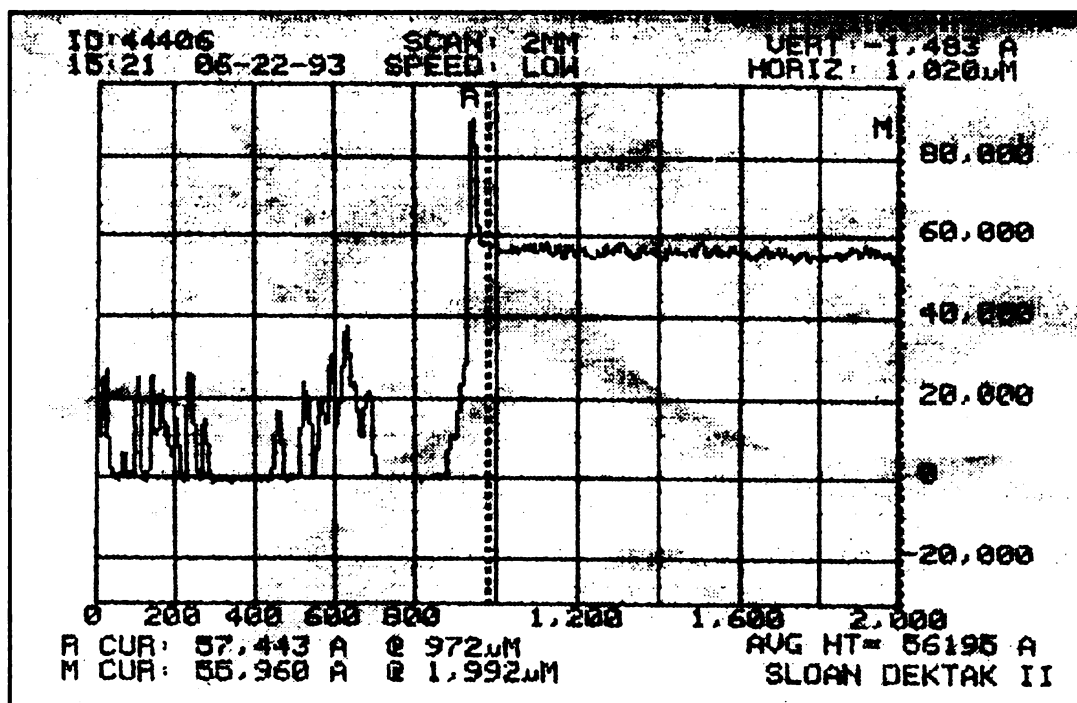


Figure 4.20. Thickness of the doped film on sample A measured in Å by the SEM.

Figure 4.20 shows a thickness of approximately  $56,000 \text{ \AA}$  ( $5.6 \text{ }\mu\text{m}$ ) for the doped diamond layer on sample A, while Figure 4.21 shows an increasing thickness of nearly  $60,000 \text{ \AA}$  ( $6 \text{ }\mu\text{m}$ ) for the doped region on sample B.

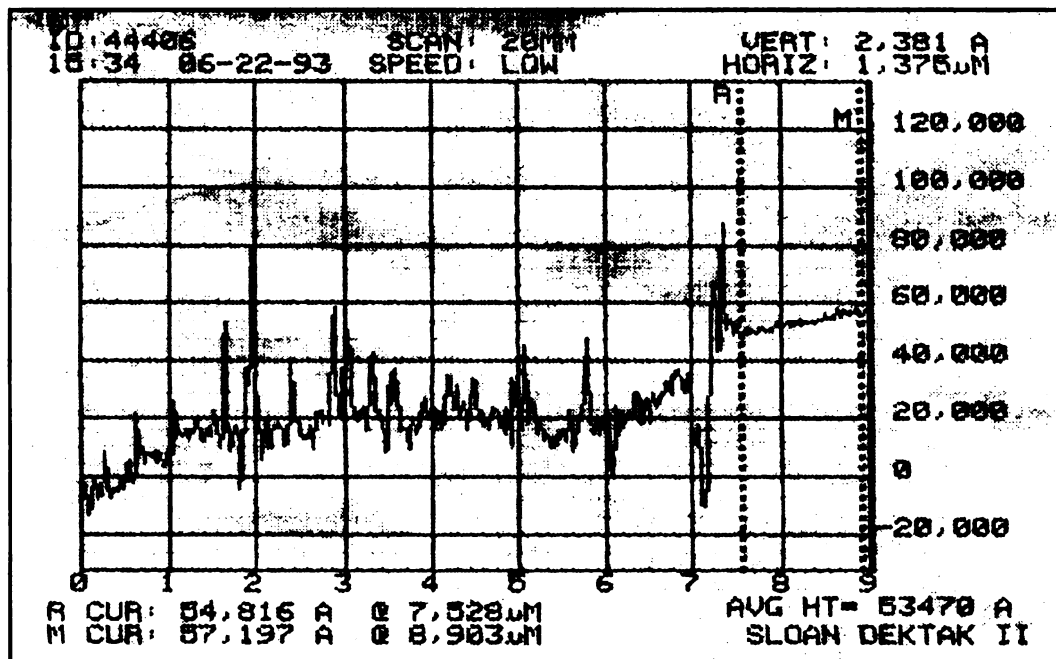


Figure 4.21. Thickness of the doped diamond film on sample B measured in Å by the SEM.

#### 4.6 Bottomside Sample Fabrication

When designing a sample that has a free standing circular diamond window  $\leq 1$  cm in diameter, specialized fabrication techniques must be used on the bottom of the sample. For instance, in order to remove the silicon backing in the area of interest and maintain the sample's structural integrity by retaining silicon in other areas, the diamond must first be patterned on the backside. Patterning, commonly known as masking, is a technique which enables diamond to be deposited and grown in precise surface configurations.

To pattern the samples, a mask is first designed. The mask is used to block UV

rays which bombard the photoresist after it has adhered to the back of the sample. By exposing the photoresist to UV radiation, diamond growth occurs in the regions shielded by the mask and is eliminated in the exposed regions.

After the back has been patterned, the undoped diamond deposition process is again repeated. Unlike the top layers of diamond, the thickness of the bottom layer has no significant effects on the results. However, the layer needs to be continuous to guard against excessive removal of the silicon during etching.

Pictures of one of the diamond samples made by the Microstructures Fabrication Laboratory is displayed in Figures 4.22 and 4.23.



Figure 4.22. Deposited doped diamond film on the front side of sample A.



**Figure 4.23.** Diamond mask patterned on the back side of sample A.

With the diamond deposition completed on the backside, the sample can now be etched. To etch the sample a solution consisting of 25 ml of hydrofluoric acid (HF), 50 ml of nitric acid ( $\text{HNO}_3$ ), and 25 ml of acetic acid ( $\text{CH}_3\text{COOH}$ ) is prepared. The solution is then carefully deposited (using a micro pipette) inside the circular region on the backside of the sample where it attacks the exposed silicon. Since the solution is applied to the silicon substrate in small amounts, the acid and its potency tend to evaporate rather quickly. In light of this, the solution is periodically deposited to the silicon surface until it has penetrated through to the undoped layer of diamond on the topside of the sample. This process, however, is a tedious one and takes several days to complete. With the

silicon completely removed in the circular region inside the diamond mask, the top layers of diamond are now free standing and exposed on both front and back sides.

## **Chapter 5**

### **Experimental Techniques**

Experimentally, diamond films are one of the most challenging materials to analyze thermally. Their microstructural size and rapid thermal response pose both spatial and temporal problems for experimental techniques utilizing surface mounted temperature sensors such as thermocouples and resistance thermometers. For this reason an optical, non-contact technique was implemented for temperature acquisition. This technique detects the thermal radiation emitted by an object and calculates the temperature.

The experimental techniques developed for the steady state temperature measurements of doped diamond films are described in this chapter. Included are subsections detailing the data-acquisition system and the experimental setup.

#### **5.1 The Data Acquisition System**

The data acquisition system is comprised of three primary components: 1) the Model 600L Infrared Imaging Radiometer, 2) the Thermal Image Processing System and 3) a digital multimeter. The first two components, the infrared radiometer and the image processor, comprised the temperature measurement system, while the digital multimeter

is used to measure the power generated in the electrical circuit. A diagram of the data acquisition system is displayed in Figure 5.1.

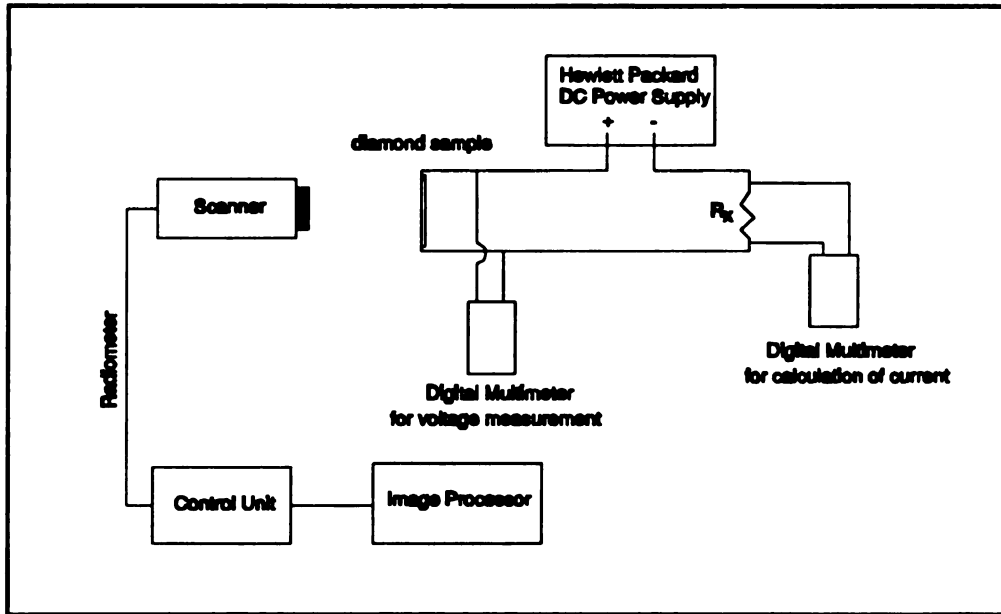
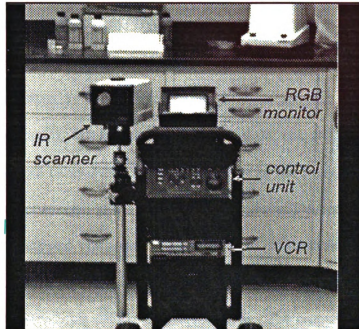


Figure 5.1. Diagram of the data acquisition system.

### 5.1.1 The Inframetrics Model 600L Infrared Imaging Radiometer

The Inframetrics Model 600L Infrared Imaging Radiometer, consisting of an infrared scanner and an electronic control unit, is designed for applications requiring real-time analysis of static or dynamic thermal patterns. The high performance system combines superior image quality and thermal sensitivity with true temperature measurement display and background correction. The system can also be linked with a video cassette recorder or a thermal image processor to store thermal events. The Model

600L IR Radiometer complete with scanner, RGB monitor, control unit and VCR is displayed in Figure 5.2.



**Figure 5.2.** The Inframetrics 600L IR Radiometer.

The scanner incorporates two independent electromechanical servos (galvanometers) which perform horizontal and vertical scanning. Attached to these servos are scanning mirrors which are contained in a sealed, evacuated module for increased efficiency. Horizontal scanning is performed at the very high rate of 8 kHz in a resonant sinusoidal mode. Vertical scanning is performed in a sawtooth pattern consistent with standard TV formats at 60 Hz.

The thermal radiation entering the scanner through a germanium window is

deflected by the horizontal and vertical scanning mirrors and is focused on a HgCdTe detector. Motorized focus and zoom mechanisms are operated within the scanner by remote control. With the HgCdTe detector cooled by liquid nitrogen to approximately 77 K, maximum thermal sensitivity is obtained.

The signal generated by the HgCdTe detector is processed, digitized, reformatted and prepared for visual display by the control unit. A microprocessor within this unit accesses such functions as background temperature, temperature range and emittance settings, image averaging, fast line scanning, focusing and zooming. The microprocessor also performs internal calibrations as the temperature of the scanner changes and when filters or lenses are connected to the scanner. The control unit accesses individual picture elements, then calculates temperatures according to calibration curves which were measured at the factory and stored in a read-only-memory. Due to variations to spectral response, every system has a unique calibration curve. The output from the control unit is a standard RS-170 format with 8 bit resolution, providing 256 pixels/line.

In order to increase the spatial resolution when imaging smaller objects, two additional lenses are installed on the front of the scanner. One lens is a 3x telescopic lens which is connected directly to the scanner. Attached to the telescopic lens, however, is a 6" closeup lens which can resolve objects smaller than 100  $\mu\text{m}$ . A photograph of the two lenses is displayed in Figure 5.3.



**Figure 5.3.** The 6" close-up lens and the 3x telescopic lens used to increase the spatial resolution of the radiometer.

### **5.1.2 Thermal Image Processing System**

The Thermal Image Processing System is primarily used to capture and store entire thermal patterns and access temperatures corresponding to any or all digitized picture elements (pixels) which make up the thermal field. Each field consists of 365 x 280 pixels, totaling over 102,000 accessible surface temperature measurements.

Temperature measurements are individually calculated from the radiant intensity

of each pixel, which is digitized and saved in an 8 bit format. When the minimal 5 °C temperature range is activated on the control unit of the Radiometer, a maximum thermal resolution of 0.03 °C is attained.

By using the external optics previously discussed and seen in Figure 5.4 and by zooming in at the minimum field of view allowed by the radiometer, the spatial resolution shrinks to approximately 1 pixel / 10  $\mu\text{m}$ . With this type of spatial resolution, the smallest area that can be fully imaged is approximately 4 mm x 3 mm.

The Thermal Image Processing System resides in an Epson 286, 16 Mz PC. Since the computer is only used to run the driver software for the image processor, access its functions and store images, the 286 is an adequate machine.

### **5.1.3 The Omega 880 Digital Multimeter**

In order to simplify the experimental setup and resulting experimental procedures, the Omega 880 Digital Multimeter is used to measure the power supplied to the electrical circuit to calculate the internal heat generation within the doped diamond film region. A picture of the multimeter is displayed in Figure 5.4.



Figure 5.4. The Omega 880 Digital Multimeter.

The multimeter is used to check and measure the applied voltage and determine the current flowing through the circuit usually by measuring the voltage across a known resistance, see Figure 5.1.

## 5.2 System Calibration Check

Since the radiometer uses inaccessible internal calibration curves which were measured by the supplier to calculate temperature, it is important that the performance of these tables be calibrated versus a known temperature in order to validate this temperature measurement system. The radiometer was calibrated using a vertically mounted "black"

aluminum plate which was uniformly heated from the backside and had a thermocouple attached to the center of the frontside. The thermocouple was used to measure the temperature of the plate. Assuming the emissivity of the plate to be 0.98, the temperature measured by the radiometer was the same as the temperature measured by the thermocouple. In this case, the emissivity that is input into the control unit of the radiometer merely acts as a calibration factor which initializes the "actual" temperature of the thermocouple and measured temperature of the radiometer.

As the temperature of the plate increased, the corresponding temperature measured by the radiometer was recorded. The calibration covered a temperature range from 25-100 °C and the results are presented in Figure 5.5.

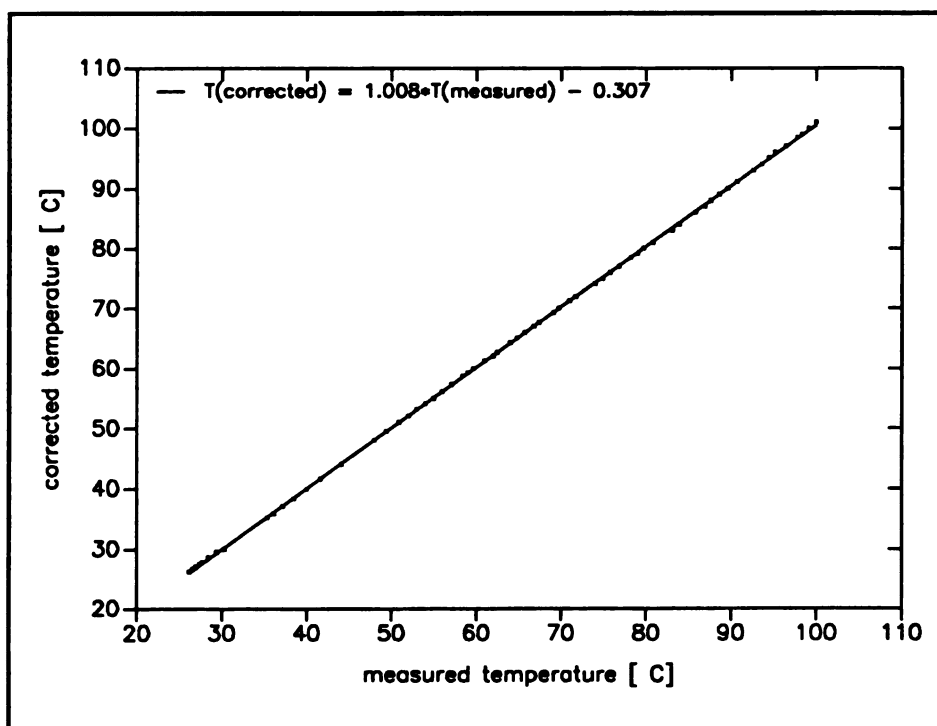


Figure 5.5. Corrected temperature of thermocouple vs. measured temperature of radiometer.

In Figure 5.5 the thermocouple temperature (assumed to be the true temperature) is plotted as a function of the temperature measured by the radiometer. A linear curve fit was performed on the data resulting in the equation,

$$T_{corr} = 1.008 * T_{meas} - 0.307 \quad 5.1$$

where  $T_{corr}$  is the corrected temperature measured by the thermocouple and  $T_{meas}$  is the temperature measured by the radiometer in °C. Although the constant term, -0.307, creates a difference between the actual temperature and the measured temperature, it has no effect on the relative temperature rise, which is the quantity needed to determine the thermal conductivity of the diamond film. Since the relative temperature rise is quantified as the difference between the initial temperature and the steady state temperature, the constant drops out and we are left with

$$\Delta T_{act} \approx \Delta T_{meas} \quad 5.2$$

Even though the exact value for the emissivity of the plate must be assumed to measure the temperature of the plate with the radiometer, the internal calibrations used by the control unit are assumed to be valid since the calibration is linear and has a slope of 1.008, which is less than 1% different from one. The recorded temperature range of 25-80 °C extends beyond the expected relative temperature rise of the experiment.

The biggest challenge in using this type of temperature acquisition system, however, involves the emissivity. In order to measure the absolute temperature or the relative temperature rise of a material, the emissivity must be known or determined. Unlike thermocouples and resistance thermometers, the temperature measured by the

radiometer is a function of the radiant intensity. For a simplified illustration, the emissive power of a grey body is expressed as,

$$E = \epsilon \sigma T^4 \quad 5.3$$

where  $\epsilon$  is the emissivity,  $\sigma$  is the Stefan-Boltzmann constant and  $T$  is the temperature in Kelvin (Siegel and Howell 1981). The radiometer internally calculates temperature from the measured emissive power  $E$ . From equation 5.3 it is evident that the emissivity must be used to determine the absolute temperature and we find that the same holds true for the relative temperature rise. Using equation 5.3, the relative temperature rise of a grey body is calculated to be

$$T - T_{\infty} = \left( \frac{1}{\epsilon \sigma} \right)^{\frac{1}{4}} \left( E^{\frac{1}{4}} - E_{\infty}^{\frac{1}{4}} \right) \quad 5.4$$

where  $T$  and  $E$  are the temperature and the radiosity at a certain state and  $T_{\infty}$  and  $E_{\infty}$  are the temperature and radiosity, respectively, of the surroundings. From equation 5.4 we also see that the relative temperature rise is a function of the emissivity.

In order to check the assumption that the relative temperature rise is a function of the emissivity, the radiometer was used to record the temperature of a heater at two different power levels. At each level, temperatures were measured using two different assumed emissivities. Since the change in the radiosity ( $\Delta E$ ) is the same in each case, the temperature difference at each emissivity is compared. Figure 5.6 is a plot of the surface temperature of the heater for both high and low radiosity levels using emissivities of 1.0 and 0.80.

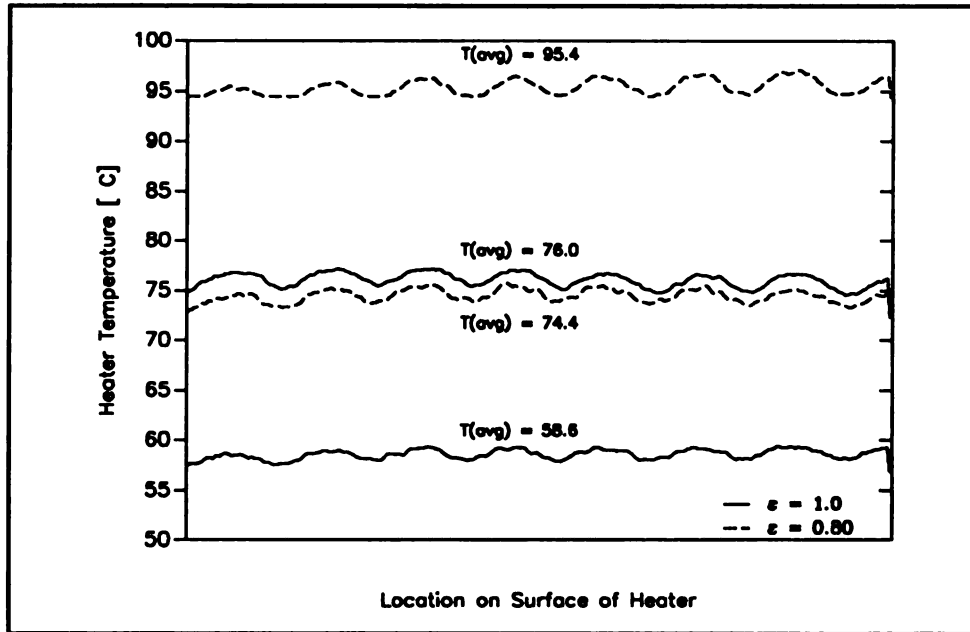


Figure 5.6. Heater surface temperature vs. location

At each level the average temperature across the surface of the heater was determined. The small peaks correspond to the heater element locations across the surface. If the temperature rise is a function of emissivity, we should get different  $\Delta T$ 's at each emissivity setting, which is the case. The temperature difference at  $\epsilon = 0.80$  (95.4-74.4) equals 21 °C whereas the temperature difference at  $\epsilon = 1.0$  equals only (76.0-58.6) 17.4 °C. These values of 21.0 and 17.4 are quite different, hence, it is evident that in order to accurately determine the relative temperature rise across the surface of the sample we must carefully determine the emissivity of the doped diamond film. Procedures involving the determination of the emissivity are discussed later in Chapter 6.

### **5.3 Experimental Setup**

A series of steady state experiments was conducted on one of the diamond film samples (sample A) which was prepared by the Microstructures Laboratory. Because of the special design considerations of the samples, the sample setup consists of only four items:

- the diamond film sample,
- electrical conducting adhesive tape,
- electrical lead wires and
- an adjustable clamp to suspend the sample in a vertical position.

#### **5.3.1 Preparation of the Sample Setup**

Each of the two setups for each sample is constructed in exactly the same manner starting with cutting the electrical conducting tape into two strips approximately 2 cm x 0.45 cm. It is important that the tape contact only the surface of the doped diamond film and not the silicon substrate. Since good contact between the tape and the film surface is imperative silver paint was added to the diamond-tape interface. A schematic and photograph of sample A after experimental sample preparation are displayed in Figure 5.7 and Figure 5.8.

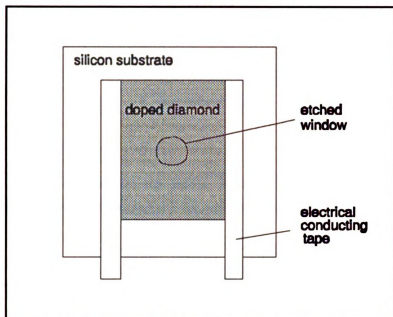


Figure 5.7. Schematic view of sample setup.

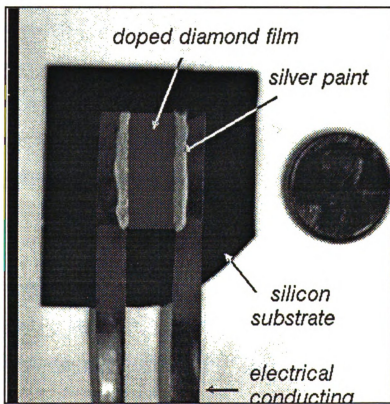


Figure 5.8. Photograph of the sample setup.

## **Chapter 6**

### **Procedures and Results for One Dimensional Radial Experiments**

This chapter presents the experimental procedures and preliminary results for the measurement of the thermal conductivity for a doped diamond film sample prepared by the Microstructures Laboratory at Michigan State University. As described in Chapter 4, the one dimensional radial heat flow model was designed to decrease the relative error in the measurements and to obtain a more symmetrical temperature distribution. By choosing a diameter of less than 0.003 m for this model, convection, which becomes less than 1% of the total heat generated, can be neglected, further simplifying experimental procedures. Issues concerning the determination of diamond film emissivity, electrical power, optimal radiometer settings and temperature acquisition are also discussed in this chapter.

#### **6.1 Determining the emissivity**

As explained in Chapter 5, the emissivity of the diamond film must be determined in order to accurately convert the emissive power measured by the radiometer to surface

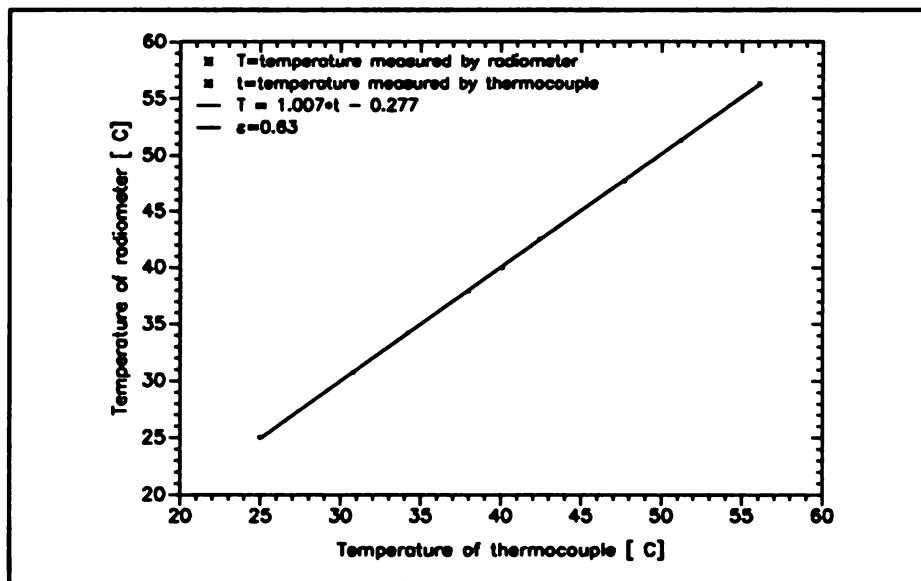
temperature. The emissivity of the diamond film sample was determined by adjusting the emissivity value input required by the radiometer such that the temperature calculated by the radiometer matched that of a thermocouple attached to the surface of the diamond film. The setup used to determine the emissivity of the diamond film is presented in Figure 6.1.



Figure 6.1. Setup used to determine the emissivity of the diamond film for sample A.

The area mode on the control unit of the radiometer was activated allowing for a real time averaged temperature measurement over a small surface area anywhere within the imaged field of view. With the small area positioned on the junction of the thermocouple itself, the radiometer measured the temperature of the thermocouple as the sample was

heated over a temperature range from 25-55 °C. The temperatures matched when using an emissivity of 0.63 as input into the control unit. The correspondence between the temperature measured by the thermocouple and the temperature measured by the radiometer using an emissivity of 0.63 is presented in Figure 6.2.



**Figure 6.2.** The relationship between the temperature measured by the radiometer and the thermocouple at an emissive setting of 0.63.

By performing a linear curve fit on the data, we see that there is a slope of 1.007 for a temperature range between 25-55 °C, refer to Figure 6.2. The correlation coefficient for this linear curve fit was determined to be 0.998. Since there is less than 1% error in assuming a slope of 1.000 and since the constant offset is cancelled out when taking differences, we are confident in assuming the emissivity of the diamond film to be 0.63 over the temperature range of interest here.

Ideally, we would like to determine the emissivity with the junction of the thermocouple attached to the free-standing diamond film, since it is the temperature distribution in this region which will be recorded. However, attempting to apply and attach a thermocouple to this fragile area proved to be disastrous for sample B. Upon first attempting this procedure using sample B, the free-standing diamond window was subsequently broken when thermocouple wires (approximately 100  $\mu\text{m}$  in diameter) were pushed through this region. With just one other sample to work with, sample A, every precaution was taken to ensure its structural integrity not only in this procedure but in the ones that followed.

## **6.2 Measurement of the Electrical Power**

Measuring the electrical power in the designed circuit is imperative in determining the volumetric heat generated in the doped diamond film region. Without knowing the volumetric heat generation it is impossible in the present experiment for us to determine the thermal conductivity of the CVD doped diamond film. However, due to the rapid thermal response of diamond during heating, the Omega digital multimeter can have difficulty tracking the electrical current flowing through the circuit. This problem is further compounded by the fact that electrical power generated within the doped region of the film was found to be a function of temperature. For this reason, the electrical power is calculated by determining the electrical resistance of the doped film as a function of temperature, rather than the standard method of measuring the voltage across a known resistance. In order to measure the resistance as a function of temperature the sample was placed in an oven where the electrical resistance was measured using the

digital multimeter and the temperature was measured by the thermocouple used to determine the emissivity. The temperature of the oven was varied over a range from 25-55 °C. The results of the measured resistance at different temperatures are presented in Table 6.1.

Temperature (°C)	Resistance ( $\Omega$ )
25	1184
30	1173
35	1157
40	1144
45	1124
50	1101
55	1075

Table 6.1. Temperature versus resistance for sample A.

Notice that the resistance decreases with increasing temperature, which is characteristic of semiconductors. About a 10% reduction in the electrical resistance is noted over a temperature rise of 30 °C.

Hence, instead of measuring the current through a known resistor and calculating the power using  $V \cdot I$ , where  $V$  is the voltage and  $I$  is the current, the electrical power can be more accurately determined in this case from the  $V^2/R$  relationship, where  $V$  is the voltage and  $R$  is the electrical resistance.

### 6.3 Radiometer Settings

After the emissivity ( $\epsilon$ ) and the resistance of the diamond film have been determined, the radiometer is now prepared for thermal image acquisition. Using an emissivity of 0.63, the thermal sensitivity was maximized by using the smallest temperature range of 5 °C. Four images were averaged in real time to improve the signal-to-noise ratio. Image averaging is an attractive option for two main reasons. First and foremost, the signal-to-noise ratio alone is increased by a factor of two in this case and second the amount of data is compressed by a factor of four. However, when using this real time image averager, one must be certain that the displayed thermal field, a composite image averaged from four separate fields, does not contain any thermal information of the relative temperature rise of the diamond window in its transient state. Since the averaged image is being scanned at a 0.07 sec interval (60/4 Hz), we need to capture the image at least 0.07 sec after the relative temperature rise is at a steady state condition or transient effects would be averaged into the results.

The time constant of the film can be approximated by the relation,

$$t \approx \frac{b^2}{\alpha}, \quad 6.1$$

(Carslaw and Jeager 1959) where  $\alpha$  is the thermal diffusivity of the diamond film,  $b$  is

the radius of the etched region and  $t$  is the approximate time in which the relative temperature rise reaches steady state. Assuming a thermal conductivity of 200 W/m K, a density ( $\rho$ ) of 3500 kg/m<sup>3</sup> and a specific heat ( $c_p$ ) of 509 J/kg K, the thermal diffusivity ( $\alpha$ ) is calculated to be  $112.3 \times 10^{-6}$  m<sup>2</sup>/sec for this case where  $b = 0.003$  m. A thermal conductivity of 200 W/m K, which is on the low end of the published values for the thermal conductivity of diamond films, was used to give us a "worst case" scenario for the time constant. The larger the time constant, the more limiting is the use of the image averager. From equation 6.1, the time constant of the diamond film is calculated to be approximately 0.02 sec using a radius ( $b$ ) of 1.5 mm. Hence, as long as we capture the image 0.10 sec after the film has started to heat, the composite thermal field averaged over four images should represent the relative temperature rise in its steady state condition.

It should be noted that although the relative temperature rise of the etched diamond window reaches a steady state condition, the surface temperatures continue to rise as the sample is heated. This condition is termed a quasi-steady state and it is this condition that describes the global heating of the diamond-silicon specimen.

Because the heating of the sample is described by a quasi-steady state condition and not entirely by the steady state condition modeled, it is important to determine the amount of energy lost due to the heat capacity of the diamond sample. The effective volumetric heat capacity  $g_{hcap}$  of the diamond film which is the energy absorbed in the film itself is given by

$$g_{hcap} = \rho C_p \frac{\partial T}{\partial t} \quad 6.2$$

Using the density ( $\rho$ ) and the specific heat ( $C_p$ ) for diamond, as previously determined, and typical experimental data where  $\partial T/\partial t = (30-22)^\circ\text{C}/2 \text{ secs}$ ,  $g_{\text{hcap}} \approx 8.91 \times 10^5 \text{ W/m}^3$ . We now need to compare the volumetric heat capacity,  $g_{\text{hcap}}$  with the measured volumetric heat generation,  $g_d$ . For an experiment corresponding to the particular temperature rise used to calculate  $g_{\text{hcap}}$ ,  $g_d \approx 1.75 \times 10^9 \text{ W/m}^3$ . By determining the ratio ( $g_{\text{hcap}}/g_d$ ), we see that the energy needed to increase the temperature of the exposed diamond film in its quasi-steady state represents less than 0.1% of the total volumetric heat generation ( $g_d$ ) in the film.

## **6.4 Surface Temperature Measurements**

Acquiring surface temperature measurements when using the thermal image processor consists of two main processes: 1) capturing the desired thermal field and 2) acquiring the surface temperatures, respectively.

### **6.4.1 Capturing Images Using the Thermal Image Processor**

Before the actual thermal images are acquired, the sample must be aligned and focused within the desired field of view (FOV). Because the focal distance between the sample and the scanner is approximately 15 cm, the minimum FOV could not be used because the scanner aperture reflected back off of the sample. This reflection shows up as a black dot, which is present in the center of the image at close range and is magnified when decreasing the FOV. As a result, the FOV and the position of the sample were adjusted to avoid this reflection. In the experiments that follow two different FOV's were utilized.

Once the optics are adjusted and the scanner focused, the sample was connected to the electrical circuit and a constant voltage is applied. The temperature of the sample immediately increases and as it enters into the user defined range (e.g. 25-30 °C) the image is captured and stored using the freeze frame on the image processor. It is this image which contains the desired temperature distribution across the film.

During this procedure, the radiometer was first focused on the front side of the sample. However, in this position the boundary temperature at the silicon-diamond interface was difficult to determine. Since the chemical etches the silicon at an angle, the thickness of the silicon at this interface is relatively thin, making it difficult to locate when imaging through the diamond on the front side. A photograph of the sample setup viewed from the front side is presented in Figure 6.3.

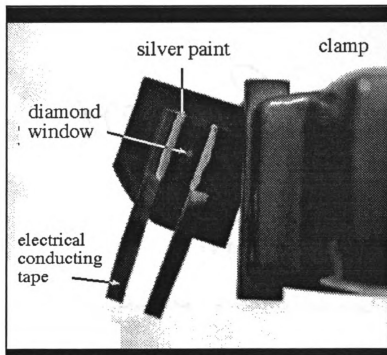


Figure 6.3. Sample setup viewed from the front side.

As seen in Figure 6.3, silver paint was used on the sample to increase electrical contact between the electrical conducting tape and the doped diamond surface, resulting in increased uniform heating. The paint was not essential.

In order to locate the boundary of the free-standing diamond window 3 mm in diameter with greater precision, the sample was simply rotated 180° such that the back side of the sample was imaged. A photograph of the sample setup in this position is presented in Figure 6.4.

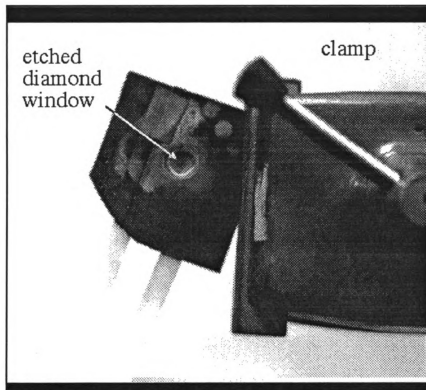


Figure 6.4. Sample setup viewed from the back side.

In this position the diamond-silicon interface can be determined more accurately in the infrared image. Since there is a negligible temperature gradient across the thickness of the diamond film and since the sample is symmetric on both faces, the temperature distribution on both sides of the sample is assumed to be equivalent. Hence, our results should not be adversely affected by positioning the sample in this manner.

Before acquiring the thermal images, the precise location of the diamond-silicon interface in the FOV is determined. By using the electronic ruler provided by the image processor software, the coordinates for the diameter of the free standing diamond film are located. After the diameter is located, the x,y coordinates which are displayed by the RGB monitor are recorded such that the appropriate temperature distribution can later be extracted from the acquired thermal field.

After the diameter of the free standing film has been located in the FOV, the thermal fields can now be acquired. With the power settings set at approximately 0.40, 0.62 and 0.88 watts five thermal images were captured using two different FOVs. These images can be viewed in Figures 6.5-6.9.

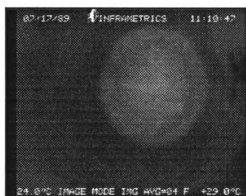


Figure 6.5. Image 1 from experiment #1 at 0.40 watts.

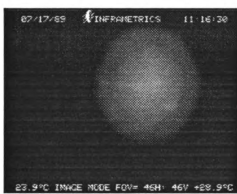


Figure 6.6. Image 2 from experiment #2 at 0.62 watts.



Figure 6.7. Image 3 from experiment #3 at 0.88 watts.



Figure 6.8. Image 4 from experiment #4 at 0.40 watts.



Figure 6.9. Image 5 from experiment #5 at 0.88 watts.

### **6.4.2 Temperature Acquisition**

After the thermal images have been acquired using the appropriate control unit settings on the radiometer, the temperatures can be determined from the thermal field using the *File\_Access* program run by the *GWBASIC* interpreter. This program, which is part of the thermal image processor software, extracts data from a particular line in the thermal field and converts the individual pixel intensity to temperature using calibration tables stored in the ROM of the radiometer's microprocessor. To extract the temperature distribution, *File\_Access* simply prompts the user for the image filename and the line number. With the location of the diameter already determined, the line number is entered and the temperatures corresponding to the pixel location across the entire thermal field are then written to a data file.

After the temperatures have been determined across the designated line from the thermal field, the next step is to extract only those temperatures associated with the temperature distribution across the diameter of the diamond window. Since the coordinates of the diameter were already determined by using the electronic ruler, the temperature distribution across the 3 mm diameter free-standing diamond window for each of the five experiments can be located and extracted from the line temperature data extending across the entire horizontal FOV. The temperature distribution for each of the five experiments can be seen in Appendix B.

### **6.5 Measurement of the Thermal Conductivity**

Quantifying the thermal conductivity after acquiring the temperature distribution across the diamond film requires two steps. The first step is to develop a mathematical

model for the problem; and the second step is to use the temperature data and the model together to estimate the thermal conductivity ( $k_{||}$ ).

### 6.5.1 The Simplified Experimental Model

Because the temperature difference between the surface of the film and the surroundings is small (within 10 °C), it is reasonable to assume that radiation can be neglected. The validity of this assumption is demonstrated below through acquired experimental data. Heat transferred by radiation is described by

$$Q_{rad} = 2A\epsilon\sigma(T^4 - T_{\infty}^4) \quad 6.3$$

where  $\epsilon$  is the emissivity,  $\sigma$  is the Stefan-Boltzmann constant,  $T$  is the temperature of the film,  $T_{\infty}$  is the temperature of the surroundings and  $2A$  ( $2\pi r^2$ ) represents both sides of the surface area of the exposed diamond window. With  $\epsilon = 0.63$ ,  $\sigma = 5.67 \times 10^{-8} \text{ W/m}^2 \text{ K}^4$ ,  $r = 0.0015 \text{ m}$ ,  $T = 305 \text{ K}$  (32 °C) and  $T_{\infty} = 295 \text{ K}$  (22 °C),  $q_{rad} = 0.00054 \text{ W}$ . Since the temperature difference used in this calculation simulates experiments for the largest heat dissipation ( $q = 0.88 \text{ W}$ ) radiation represents less than 0.1% of the total heat generated within the film and, therefore, can be neglected.

Since the diamond window was etched to only a diameter of 0.003 m to aid in the strength of the sample, the effects of convection, discussed in detail in Chapter 4, can also be neglected. With a characteristic length of 0.003 m convection  $\leq 1\%$  of the total heat generated within the film, when assuming a thermal conductivity between 250-1000 W/m K, which is the expected range for the thermal conductivity of doped diamond. The

percentage of heat lost due to convection is, again, calculated from equation 4.19.

By neglecting convection, the former mathematical description of the experiment, described by equation 4.10, is further simplified to

$$\theta(r) = \frac{g_d \delta_d}{4k(\delta_u + \delta_d)} (b^2 - r^2) \quad 6.4$$

where

$$g_d = \frac{V^2}{RLW\delta_d} \quad 6.5$$

and

$$\theta(r) = T(r) - T_b \quad 6.6$$

Equation 6.6 represents the difference between the temperature at the boundary ( $r=b=0.0015$  m) and the temperature at a particular radial position.

### 6.5.2 Estimating the Thermal Conductivity

Now that the appropriate temperature distributions have been acquired and the governing equation simplified, the program NLIN (Beck 1993) is used to analyze the data and estimate the thermal conductivity. NLIN uses the method of least squares

$$S = \sum_{j=1}^N [Y_j - T_j]^2 \quad 6.7$$

where  $N$  is the number of data points,  $Y_j$  is the measured temperature and  $T_j$  is the calculated temperature represented by

$$T_j = T_b + HK \left[ 1 - \left( \frac{r_j}{b} \right)^2 \right] \quad 6.8$$

where  $H = (g_d \delta_d b^2) / 4(\delta_u + \delta_d)$  and  $K = 1/k$ . Using the method of least squares the program simultaneously estimates both  $T_b$  and  $k$  to calculate  $T_j$  such that the error in  $S$  is minimized. In order to minimize the error in  $S$ , NLIN uses the system of equations

$$\frac{\partial S}{\partial T_b} = -2 \sum_{j=1}^N [Y_j - T_j] = 0 \quad 6.9$$

and

$$\frac{\partial S}{\partial k} = -2 \sum_{j=1}^N [Y_j - T_j] H \left[ 1 - \left( \frac{r_j}{b} \right)^2 \right] = 0 \quad 6.10$$

Actually, NLIN is a sequential nonlinear estimation program that has more complex calculations than indicated by equations 6.9 and 6.10 but these equations form the basis of its estimation process for this linear problem.

By inputting  $H = V^2 b^2 / 4RLW(\delta_u + \delta_d)$  for each case where  $L = 0.0045$  m,  $W = 0.02$  m,  $b = 0.0015$  m and  $V$  is measured and  $R$  is determined from Table 6.1,  $T_j$  is calculated for each of the five experiments. The measured temperature distribution ( $Y_j$ ) and the corresponding calculated temperature distribution  $T_j$  across the surface of the diamond window are displayed together in Figures 6.10 and 6.11. The largest temperature rise is approximately 3 °C.

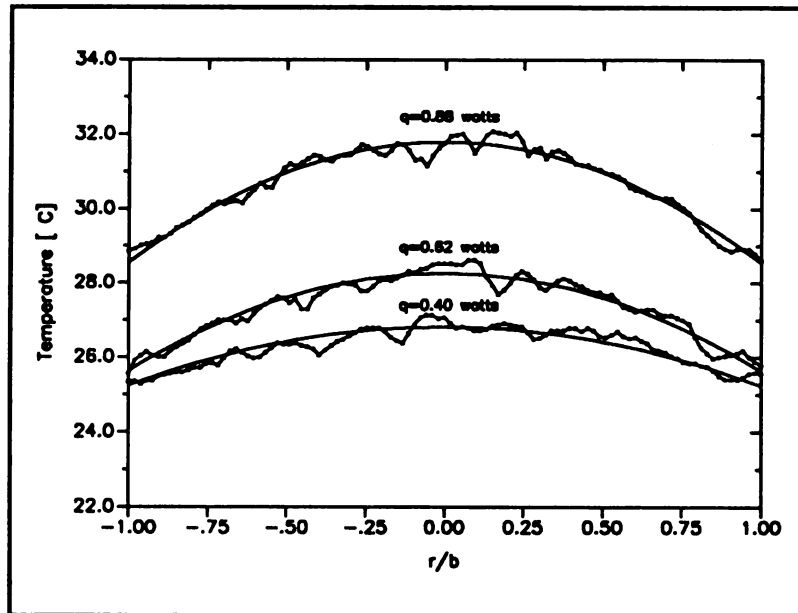


Figure 6.10. Measured and calculated temperature distribution for experiments 1,2 and 3.

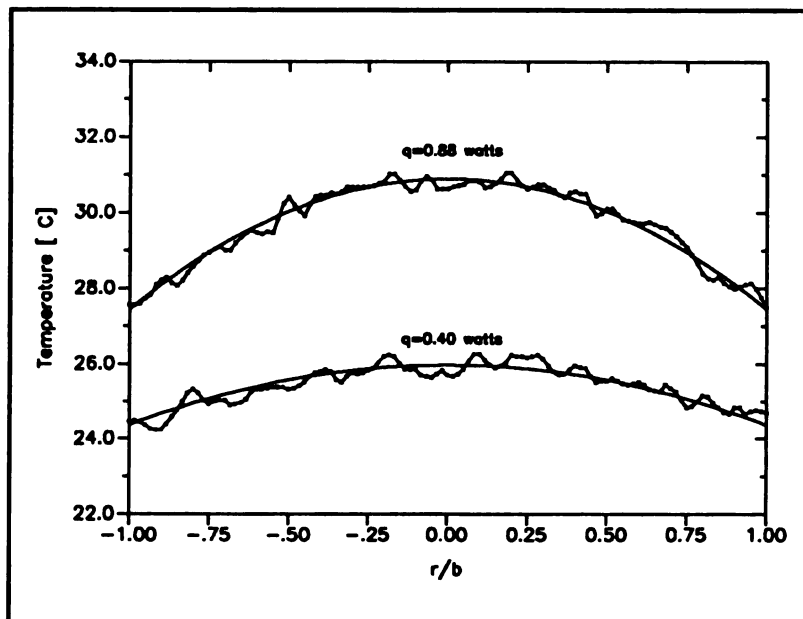


Figure 6.11. Measured and calculated temperature distribution for experiments 4 and 5.

NLIN not only fits the mathematical model, equation 6.4, to the data but it also calculates the residuals which are the differences between the measured and calculated temperatures  $[Y_j - T_j]$ . The residual distribution for each of the five experiments can be seen in Figures 6.12-6.16. The standard deviations are approximately  $0.18\text{ }^\circ\text{C}$ , compared to about a  $2\text{ }^\circ\text{C}$  temperature rise.

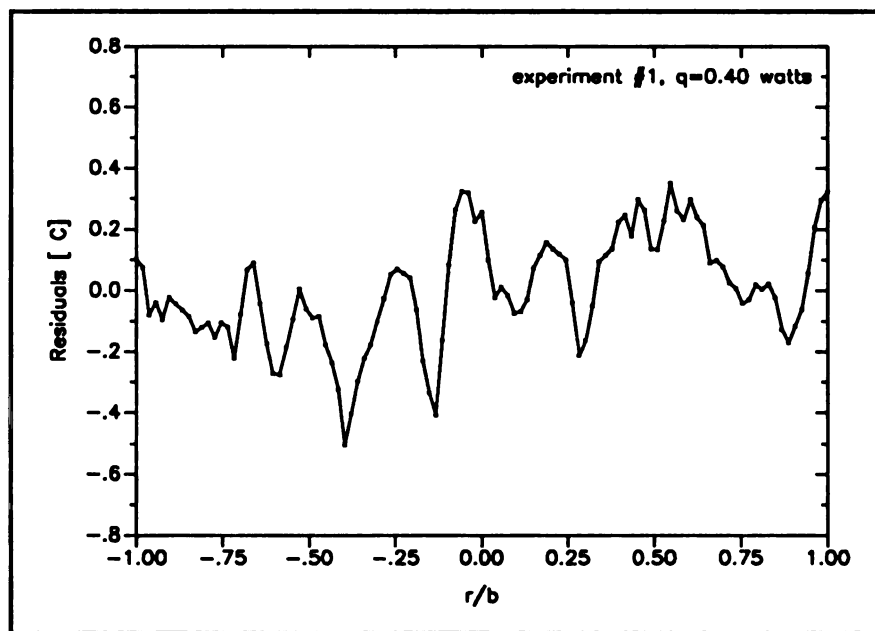


Figure 6.12. Residual distribution for experiment #1, 107 pts.

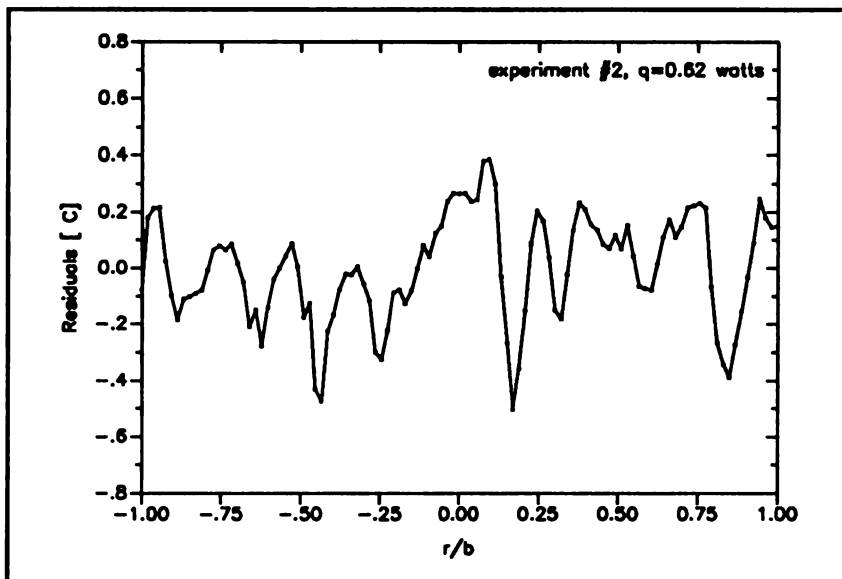


Figure 6.13. Residual distribution for experiment #2, 107 pts.

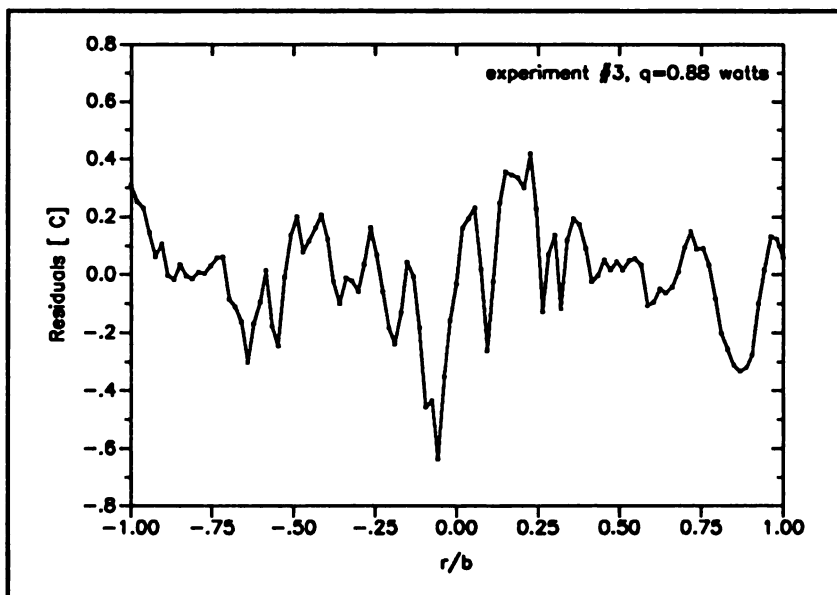


Figure 6.14. Residual distribution for experiment #3, 107 pts.

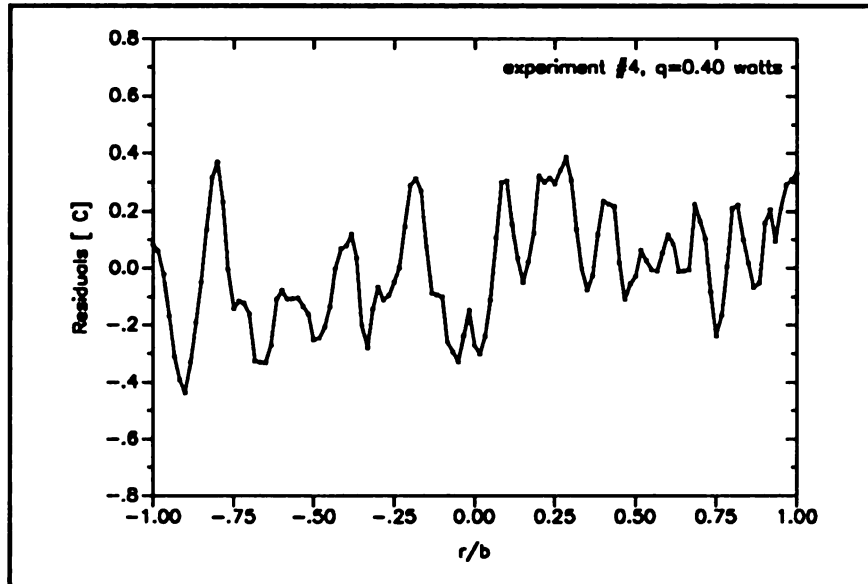


Figure 6.15. Residual distribution for experiment #4, 121 pts.

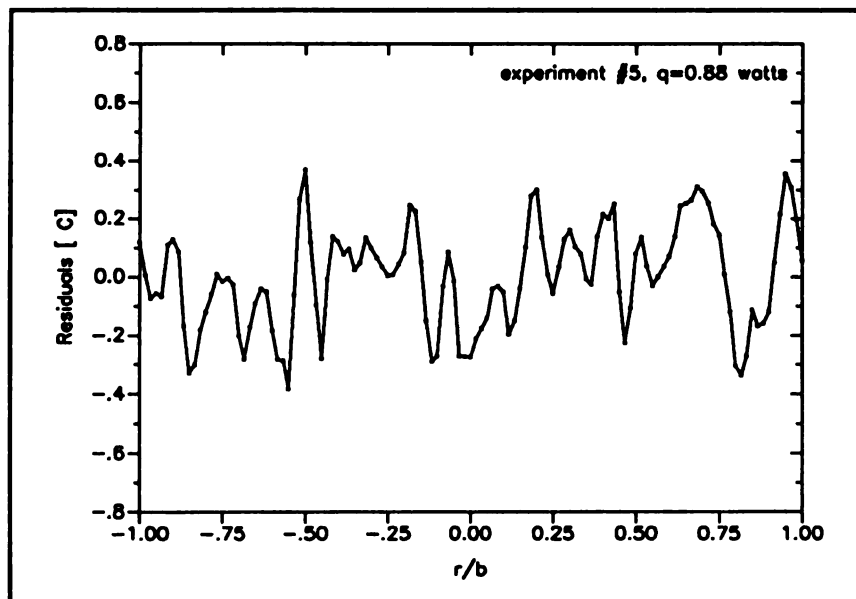


Figure 6.16. Residual distribution for experiment #5, 121 pts.

Across most of the diameter, the residual pattern is unique for each of the five experiments, representing a random rather than a systematic error. However, in the region  $0.75 < r/b < 1.00$ , a trend may exist. This trend could represent a systematic error due to the non-uniform heating noticed while running the experiments. At certain temperature ranges a slight thermal wave starting outside the region  $r = +b$  and continuing across the diamond film was visible in the displayed thermal field. This wave could be the result of non-uniform doping in the semiconducting diamond layer, non uniform thickness in the diamond or even the non-uniform thickness of the silicon at the boundary where  $r = b$ .

Although the pattern is mostly random from one experiment to another, the residuals remain correlated due to the number of points making up the "peaks" and "valleys" describing the residual distribution.

The thermal conductivity is estimated sequentially from the temperature data across the surface of the entire diamond window using the system of equations presented by equations 6.8, 6.9 and 6.10. The results are presented in Figures 6.17-6.21.

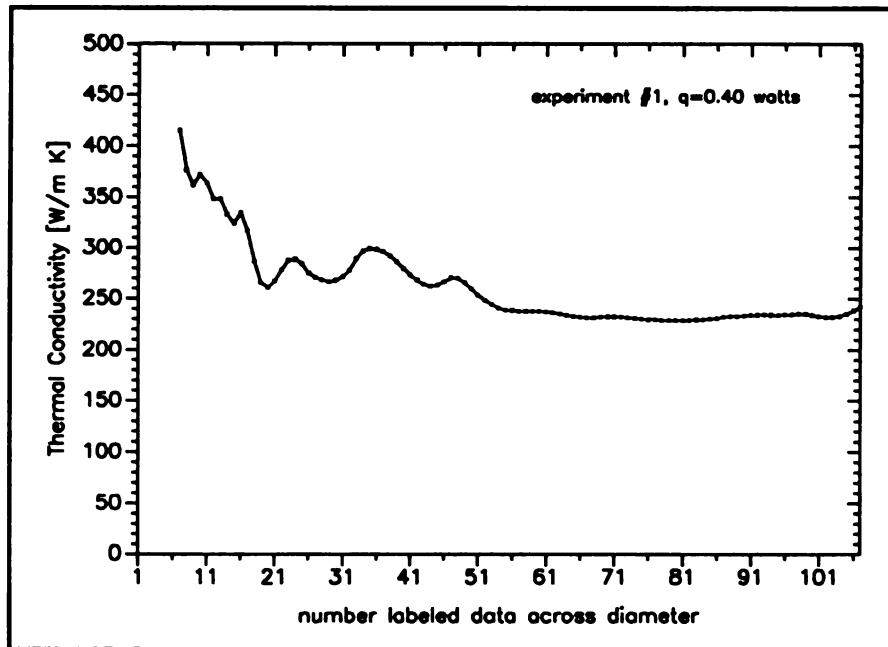


Figure 6.17. Sequential estimation of the thermal conductivity for experiment #1, 107 data points.

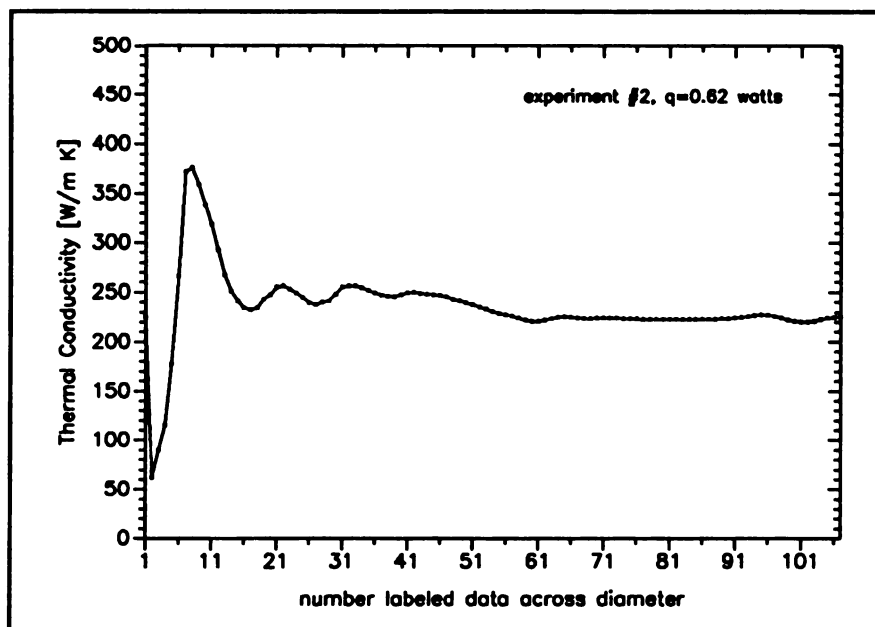


Figure 6.18. Sequential estimation of the thermal conductivity for experiment #2, 107 data points.

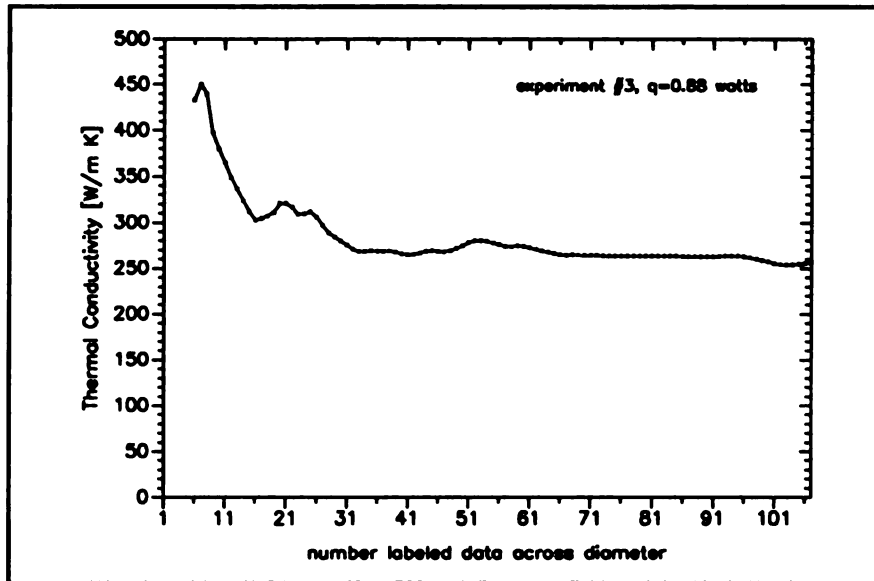


Figure 6.19. Sequential estimation of the thermal conductivity for experiment #3, 107 data points.

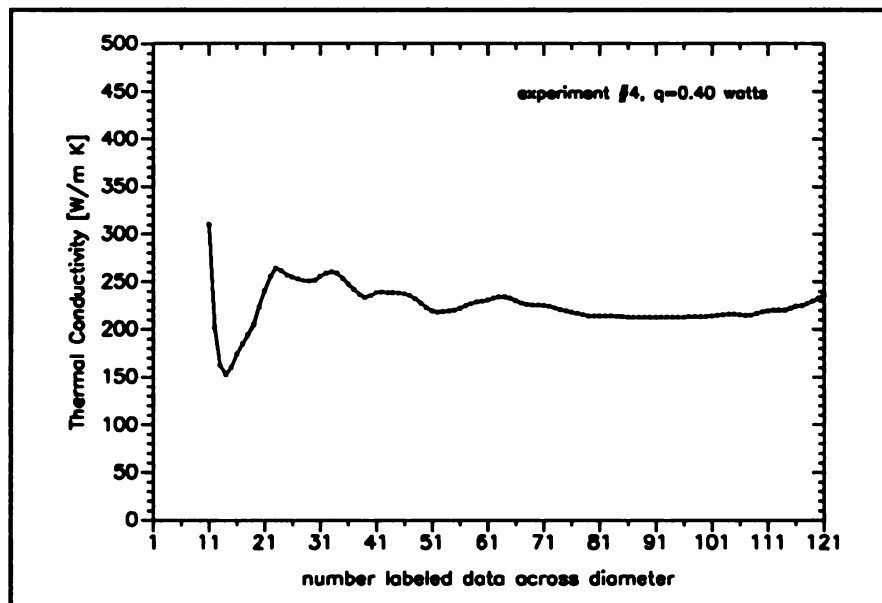
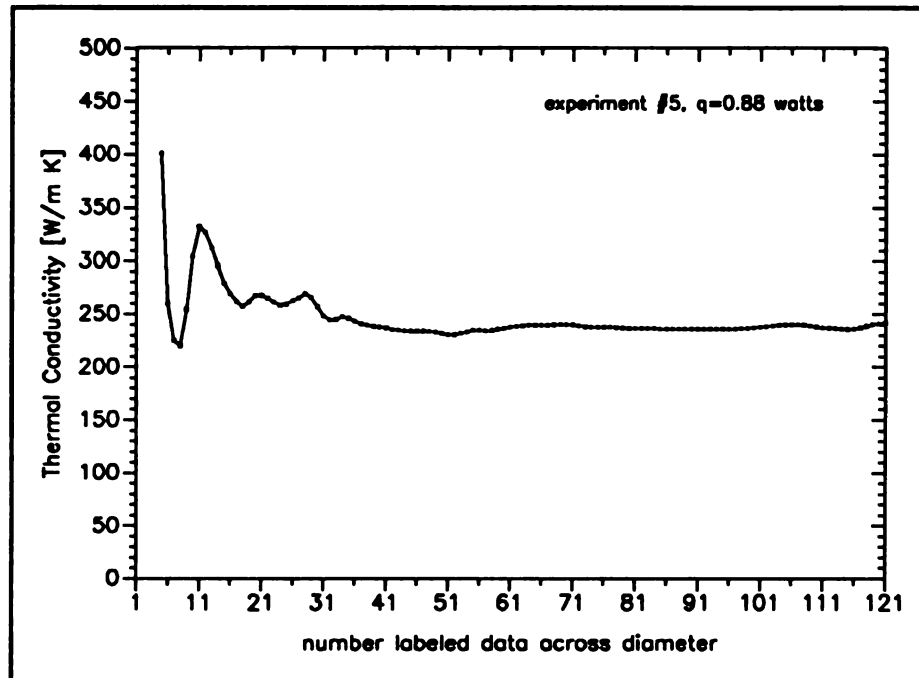


Figure 6.20. Sequential estimation of the thermal conductivity for experiment #4, 121 data points.



**Figure 6.21.** Sequential estimation of the thermal conductivity for experiment #5, 121 data points.

The initial estimates for the thermal conductivity using the first 25 points or so vary with great magnitude. This variation is due to the limited amount of data for the system to converge to a consistent estimate for both  $T_b$  and  $k$ . As more data are used, however, the estimate begins to settle around a tighter range and remains relatively constant throughout most of the second half of the data set.

The final estimate either at  $x=107$  or  $x=121$ , depending on the particular FOV used in the experiment, represents the best estimate by the system for the thermal conductivity. The estimated thermal conductivity for each of the five experiments is presented in Table

Experiment No.	k (W/m K)	Voltage (volts)	Resistance (ohms)	Power (Watts)
1	242	21.8	1184	0.40
2	225	27.1	1177	0.62
3	256	32.1	1173	0.88
4	236	21.7	1184	0.40
5	241	32.1	1173	0.88

**Table 6.2.** The thermal conductivity estimated by NLIN for each of the five experiments at different power levels.

For the five experiments the average value for the thermal conductivity for sample A and the standard deviation from that average are calculated to be  $240 \pm 11$  W/m K, respectively. The standard deviation represents experimental reproducibility to within a 5% variation in the average value for one sample using three different power levels and two different fields of view (FOV).

The thermal conductivity for sample A is determined from experiments 3 and 5 where the electrical power was set at 0.88 watts and the signal-to-noise ratio is greatest. The  $100(1-\alpha)\%$  confidence interval for the resulting estimates in each experiment is

assumed to be

$$k - \sigma_s \sqrt{(\mathbf{X}^T \mathbf{X})^{-1}} t_{1-\alpha/2} (n-p) \leq k \leq k + \sigma_s \sqrt{(\mathbf{X}^T \mathbf{X})^{-1}} t_{1-\alpha/2} (n-p) \quad 6.11$$

where  $\sigma_s$  is the standard deviation of the temperature,  $\sqrt{((\mathbf{X}^T \mathbf{X})^{-1})}$  is the square root of the covariance matrix divided by the variance and  $t_{1-\alpha/2} (n-p)$  is the t statistic for  $(n-p)$  degrees of freedom (Beck and Arnold, 1976). For 95% confidence  $t_{.975}(100) \approx 1.998$  (Miller and Freund, 1965). Since  $\sigma_k$  and  $\sqrt{((\mathbf{X}^T \mathbf{X})^{-1})}$  are calculated from the NLIN output file, the estimated thermal conductivity and confidence interval for experiment #3 and experiment #5 are determined to be  $256 \pm 9$  W/m K and  $241 \pm 7$  W/m K, respectively. The uncertainty of the measurement is approximately  $(100 \times (9/256)\%)$  3.6% for experiment #3 and  $(100 \times (7/241)\%)$  3.0% for experiment #5.

Hence, the estimated thermal conductivity for sample A, calculated by averaging the results obtained in experiments 3 and 5, is determined to be  $249 \pm 8$  W/m K. The confidence interval represents a 3.2% uncertainty in the estimated value of the thermal conductivity.

## 6.6 Experimental Uncertainty

The experimental uncertainty is a measure of the accuracy of the method used in determining the thermal conductivity and accounts for measurement uncertainties in quantities such as thickness of film, voltage, temperature, etc. It acts as a global uncertainty which is driven by the precision at which all of the experimental unknowns can be measured. The uncertainty in the measurement of the thermal conductivity is determined from the expression,

$$\begin{aligned}
w_k = [ & \left( \frac{\partial k}{\partial V} \Delta V \right)^2 + \left( \frac{\partial k}{\partial b} \Delta b \right)^2 + \left( \frac{\partial k}{\partial R} \Delta R \right)^2 \\
& + \left( \frac{\partial k}{\partial L} \Delta L \right)^2 + \left( \frac{\partial k}{\partial W} \Delta W \right)^2 \\
& + \left( \frac{\partial k}{\partial \theta} \Delta \theta \right)^2 + \left( \frac{\partial k}{\partial (\delta_d + \delta_u)} \Delta (\delta_d + \delta_u) \right)^2 ]^{\frac{1}{2}}
\end{aligned} \tag{6.12}$$

where the terms  $\partial k/\partial \xi$  are the sensitivity coefficients determined from equation 6.4 and the  $\Delta \xi$  terms are the estimated errors in the measurements. The experimental uncertainty is calculated using the power levels and temperature rises for experiments 3 and 5, as stated before. The experimental parameters, their uncertainties and the corresponding contributions to the uncertainty of the thermal conductivity are presented in Table 6.3.

Experimental Parameter ( $\xi$ )	Estimated Uncertainty in Parameter ( $\Delta \xi$ )	Contribution to the uncertainty in the thermal conductivity ( $W^2/m^2 K^2$ )
V = 32.1 volts	$\Delta V = 0.1$ volts	$(\partial k/\partial V \Delta V)^2 = 3.0$
R = 1173 $\Omega$	$\Delta R = 5$ $\Omega$	$(\partial k/\partial R \Delta R)^2 = 1.4$
b = 0.0015 m	$\Delta b = 0.00001$ m	$(\partial k/\partial b \Delta b)^2 = 13.7$
L = 0.0045 m	$\Delta L = 0.00010$ m	$(\partial k/\partial L \Delta L)^2 = 38.0$
W = 0.02 m	$\Delta W = 0.00005$ m	$(\partial k/\partial W \Delta W)^2 = 0.5$
$\theta = 3$ $^{\circ}C$	$\Delta \theta = 0.1$ $^{\circ}C$	$(\partial k/\partial \theta \Delta \theta)^2 = 85.4$
$\delta_d + \delta_u = 0.0000066$ m	$\Delta(\delta_d + \delta_u) = 0.0000001$ m	$(\partial k/\partial(\delta_d + \delta_u) \Delta(\delta_d + \delta_u))^2 = 17.65$

**Table 6.3.** Experimental parameters, their estimated uncertainties and the corresponding contributions to the uncertainty of the thermal conductivity.

The uncertainty in the voltage measurement ( $\Delta V = 0.1$  volts) was chosen since the DVM recorded voltages to the nearest 0.1 volts. The uncertainty in the resistance ( $\Delta R = 5 \Omega$ ) was determined from the variation of the resistance due to temperature range from 28-31 °C. The uncertainty in the radius (0.00001 m) was determined by measuring the sample under a microscope using an objective micrometer which had a sensitivity of 0.00001 m. The uncertainty of the width  $\pm 0.00005$  m and the uncertainty in the length of 0.00010 m is due to the silver paint which was added to the surface of the sample to improve the electrical contact. The boundary of the silver paint is not as sharp and clear as the other recorded dimensions. The uncertainty of the diamond film thickness was determined from the sensitivity of the SEM and a conservative estimate for the uncertainty of the relative temperature rise, 0.1 °C, was also chosen. By substituting the values presented in Table 6.3 and evaluating equation 6.12 the thermal conductivity along with the experimental uncertainty is calculated to be  $249 \pm 13$  W/m K. This represents approximately a 5.2% uncertainty in the estimated value of the thermal conductivity. It is interesting to note that the confidence interval calculated by NLIN, which represents uncertainties in the relative temperature distribution, and the experimental uncertainty calculated from only the uncertainty in temperature are nearly equivalent assuming  $\theta = 3$  °C and  $\Delta\theta = 0.1$  °C. The confidence interval was calculated to be  $\pm 8$  W/m K while the experimental uncertainty due to only the temperature was calculated to be  $\pm 9$  W/m K. We see from Table 6.3 that although the experimental uncertainty is primarily driven by the uncertainty in temperature it is also affected by uncertainties in other experimental parameters such as length, radius, etc.

After examining the previous works concerning the thermal properties of diamond

films discussed in Chapter 2, there are only two studies which determined the experimental uncertainty. Graebner, Jin, Kammlott, Bacon, Seibles, Banholzer (1992) and Graebner, Jin, Kammlott, Herb, Gardinier (1992) determined the experimental uncertainty for their laser pulse method to be ~3%. This uncertainty was reportedly determined by the uncertainty in film thickness. One advantage in using the laser pulse technique is that the heat dissipated does not have to be quantified and, hence, there is no need to take into account heating power uncertainties. However, there are uncertainties in the temperature measurements and in the  $\rho C_p$  product, which enables the calculation of the thermal conductivity from the thermal diffusivity. It is unclear in both articles if uncertainties in temperature and in  $\rho C_p$  are included in the results or if their reported uncertainty of 3% is calculated only from the uncertainty of the diamond film thickness.

## **Chapter 7**

### **Summary and Conclusions**

The goal of this research was to design experimental methods and techniques for the measurement of doped CVD diamond film thermal conductivity. In the pursuit of this goal both analytical and experimental studies were conducted.

From the analytical investigation, the optimal experimental model was first chosen. A sensitivity analysis determined from one dimensional, two dimensional and radial potential geometries revealed that the radial heat flow model was most sensitive to the measurement of the thermal conductivity. Further investigation of the radial model revealed optimal geometrical parameters such as the diameter and thickness of the doped diamond layer which would limit convective losses and decrease the relative error. Parameters such as film resistivity, film geometry and thickness of the undoped diamond layer were also chosen to obtain the desired temperature rise.

As a result of the analytical analysis, two diamond film samples were fabricated by the Microstructures Laboratory at the Michigan State University Research Complex using hot-filament CVD deposition. A new experimental setup was constructed and its design was the result of specialized sample fabrication techniques. A bi-regional

deposition process was conducted to deposit a doped (semiconducting) diamond layer on top of an undoped (electrically insulating) diamond region. The undoped layer with a thickness of approximately 1  $\mu\text{m}$  ensured electrical insulation between the two semiconducting layers (doped diamond and silicon). The doped layer with a thickness of approximately 5.6  $\mu\text{m}$  was fabricated by injecting boron into the film as a charge carrier which provided a means of electrically heating the samples. A diamond patterning technique was also used to deposit a diamond mask on the backside of both samples. After the mask was deposited, the exposed silicon was chemically removed, creating a free-standing diamond window. Because of the mask's chosen geometry and the chemical application process utilized during etching, the silicon was removed in the circular configuration needed to simulate the optimal radial experiment.

Temperature measurements were recorded using an infrared thermography technique. The temperature acquisition system, consisting of a high speed IR scanner, control unit, RGB monitor and high resolution thermal image processor was utilized to capture thermal images of the diamond sample during its quasi-steady heating. Temperatures across an entire line spanning the horizontal FOV and corresponding to the location of the diameter of the diamond window were first calculated from individual pixel intensity using internal calibration tables stored in the ROM of the infrared control unit and then extracted from each of the thermal images. The temperature distribution across the 3 mm diamond window was located in the extracted temperature file using an electronic ruler provided by the image processor software.

Five different experiments were conducted on one of the prepared samples using two different fields of view resulting in 107 and 121 individual surface temperature

measurements at three different power levels (0.40, 0.62 and 0.88 watts). The thermal conductivity was estimated in each experiment using the method of least squares to minimize the error between the measured temperature distribution recorded by the infrared temperature acquisition system and the calculated temperature distribution determined from the optimal radial heat flow model.

For the five experiments the average value for the thermal conductivity for sample A and the standard deviation from that average was calculated to be  $240 \pm 11$  W/m K, respectively. The standard deviation represents an experimental reproducibility for a single sample at three different power levels and two different fields of view to within a 5% variation in the average value.

The thermal conductivity for sample A was determined from experiments 3 and 5 where the electrical power was 0.88 watts and the signal-to-noise ratio was greatest. The estimated thermal conductivity for sample A, calculated by averaging the results obtained in experiments 3 and 5, was determined to be  $249 \pm 8$  W/m K using a least squares approximation. The confidence interval ( $\pm 8$  W/m K) represents a 3.2% uncertainty in this estimated value, but only considers uncertainties in temperature.

The experimental uncertainty which was determined by estimated uncertainties in the measurements of all the experimental parameters is calculated to be  $\pm 13$  W/m K. Hence, the estimated value for the thermal conductivity of a doped diamond film using the experimental methods and techniques developed in this work is determined to be  $249 \pm 13$  W/m K, representing an experimental uncertainty of  $\sim 5\%$ .

Based on the author's literature review, this is the first reported value for the thermal conductivity of a semiconducting diamond film.

**Suggestions for Future Work:**

- 1) Determine the accuracy of the methods and techniques used in the present work by simulating a similar sample setup using a material of known thermal conductivity (silicon) and then compare the known and estimated values. This "dummy" sample setup can be used to validate the mathematical model in different proposed experimental scenarios.
  
- 2) Make the sample more robust by depositing more diamond on the silicon substrate. By increasing the thickness of the doped diamond film, a more reliable sample can be fabricated, allowing for increased diamond window diameters, larger temperature rises, increased spatial resolution, decreased convective effects and better estimates of the thermal conductivity as determined by the sensitivity analysis. A thickness of at least 10  $\mu\text{m}$  for the doped layer of diamond is suggested.
  
- 3) Measure the thermal conductivity as a function of the film thickness.
  
- 4) Measure the thermal conductivity as a function of the film resistivity (doping level).
  
- 5) Measure the thermal conductivity at high temperatures using a) the present setup which is placed in an open environment which could be adversely affected by convection, b) the setup placed in a vacuum which could be adversely affected by radiation and c) the setup placed in an oven which may be most immune to the effects of convection and radiation. The "dummy" sample setup can be used here to both determine the optimal experimental environment for the measurement of the thermal properties at high temperatures and to validate the mathematical model.
  
- 6) Use the transient capabilities of the IR temperature acquisition system described in Appendix 1 to determine the density-specific heat product,  $\rho C_p$ , for CVD doped diamond films.

- 7) Develop a new experimental method which will not require specialized sample design and extensive sample preparation for the measurement of the thermal properties (e.g. bi-regional diamond deposition, diamond patterning, masking and etching). These techniques are very time consuming and their permanent effects on the sample limit the practical use of the diamond film after it has been prepared. Developing a method which would use a laser line heat source instead of electrical heating would allow for the determination of the thermal properties of both doped and undoped CVD diamond films with minimal sample preparation.
- 8) Compare the results obtained by the method used in the present work with the method proposed in 7.
- 9) Determine the thermal properties for diamond film samples prepared by the microwave method and compare with the experimental results obtained from the diamond film samples prepared by the hot filament method.
- 10) Determine the degree of reproducibility obtained for the thermal properties of diamond films prepared by a fixed processing method.

## List of References

- Albin, S., Winfree, W.P., and Crews, B. Scott, "Thermal Diffusivity of Diamond Films Using a Laser Pulse Technique.", J. Electrochem. Soc., Vol. 137, 1990, No. 6.
- Anthony, T.R., Fleischer, J.L., Olson, J.R., and Cahill, D.G., "The Thermal Conductivity of Isotopically Enriched Polycrystalline Diamond Films.", J. Appl. Phys., Vol. 69, 1991, No. 12.
- Baba, K., Aikawa, Y., and Shohata, N., "Thermal Conductivity of Diamond Films.", J. Appl. Phys., Vol. 69, 1991, No. 10.
- Beck, J.V., and Arnold, K.J., Parameter Estimation in Engineering and Science, John Wiley and Sons, 1977.
- Beck, J.V., Cole, K., Haji-Sheikh, Litkouhi, B., Heat Conduction Using Green's Functions, Hemisphere Press, N.Y., 1992.
- Carslaw, H.S. and Jaeger, J.C., Conduction of Heat in Solids, 2nd ed., Oxford University Press, London, 1959.
- Graebner, J.E., Jin, S., Kammlott, G.W., Bacon, B., Seibles, L., and Banholzer, W., "Anisotropic Thermal Conductivity in Chemical Vapor Deposited Diamond.", J. Appl. Phys., Vol. 71, 1992, No. 11.

Graebner, J.E., Jin, S., Kammlott, G.W., Herb, J.A., and Gardinier, C.F., "Unusually High Thermal Conductivity in Diamond Films.", Appl. Phys. Lett., Vol. 60, 1992, No. 13.

Graebner, J.E., Jin, S., Kammlott, G.W., Herb, J.A., and Gardinier, C.F., "Large Anisotropic Thermal Conductivity in Synthetic Diamond Films.", Letters to Nature, Vol. 359, 1992, p. 401.

Graebner, J.E., Mucha, J.A., Seibles, L., and Kammlott, G.W., "The Thermal Conductivity of Chemical-Vapor-Deposited Diamond Films on Silicon.", J. Appl. Phys., Vol. 71, 1992, No. 7.

Holman, J.P., Experimental Methods for Engineers, McGraw-Hill, Inc., 1978.

Incropera, F.P., and DeWitt, D.P., Introduction to Heat Transfer, 2nd ed., John Wiley and Sons, 1990.

Machlab, H., McGahan, W.A., and Woollam, J.A., "Thermal Diffusivity Measurements by Photothermal Laser Beam Deflection (PTD): Data Analysis Using the Levenberg-Marquardt Algorithm.", Thin Solid Films, Vol. 215, 1991, pp. 103-107.

Miller, I., and Freund, J.E., Probability and Statistics for Engineers, Prentice-Hall, Inc., 1965.

Morelli, D.T., Beetz, C.P., and Perry, T.A., "Thermal Conductivity of Synthetic Diamond Films.", J. Appl. Phys., Vol. 64, 1988, No. 6.

Ono, A., Baba, T., Funamoto, H., and Nishikawa, A., "Thermal Conductivity of Diamond Films Synthesized by Microwave Plasma CVD.", Japanese J. Appl. Phys., Vol. 25, 1986, No. 10.

Parker, W.J., Jenkins, R.J., Butler, C.P., and Abbott, G.L., J. Appl. Phys., Vol. 32, 1679, 1961.

Siegel, R., and Howell, J.R., Thermal Radiation Heat Transfer, 2nd ed., Hemisphere Publishing Corp., 1981.

Spehar, J., "Diamonds, Electronic's Best Friend.", IEEE Potentials, Vol. 10, No. 4, 1991, pp. 9-12.

Vorobei, V.V., "Thermoelastic Problems for Monodirectional Fiber Composites Exposed to Pulsed Thermal Action.", Soviet Applied Mechanics, Vol. 22, 1986.

**Appendix A.****Calibration of the Inframetrics 600L Radiometer for  
Rapid Transient Thermal Events**

By connecting the signal output from the control unit to an A/D board, the radiometer, consisting of the high speed IR scanner and control unit, has the ability to track transient thermal events. However, the voltage signal output from the control unit which is proportional to temperature must be calibrated. The calibration of the 600L radiometer for imaging transient thermal events as detailed in this section consists of five components: 1) setup and execution, 2) reproducibility, 3) temporal resolution, 4) thermal resolution and 5) relative accuracy. These components are discussed in turn in the following paragraphs.

***Setup and Execution:***

Displayed in Figure A.1 is a diagram of the experimental setup used in the calibration.

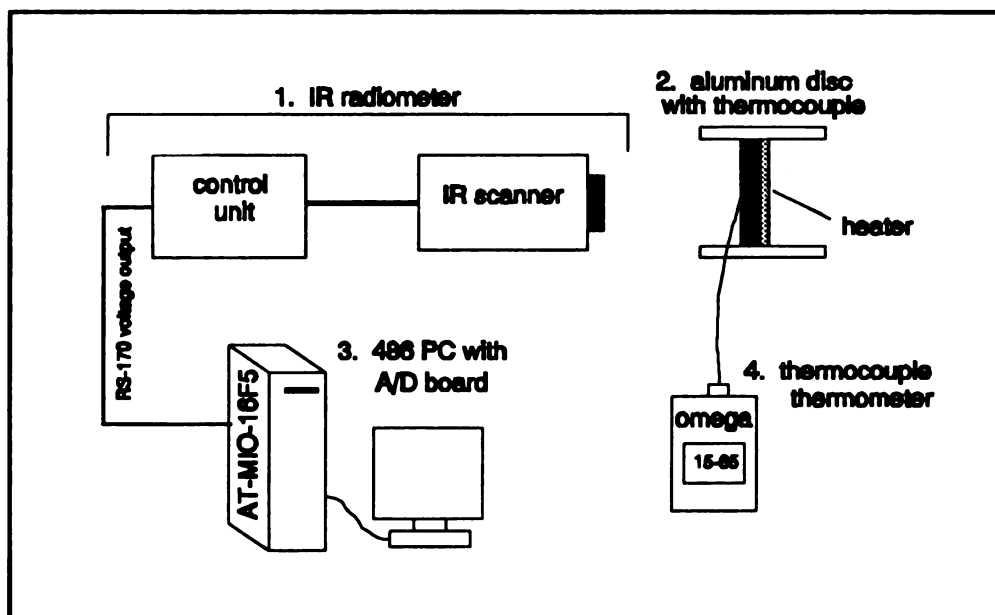


**Figure A.1.** Setup used for the calibration of the IR radiometer to record transient thermal events.

The setup consists of four main instruments: 1) The Inframetrics 600L IR radiometer, 2) black aluminum disk with heater and thermocouple, 3) computer data acquisition system with the National Instruments (AT-MIO-16F5) A/D board and 4) the Omega Type E thermocouple thermometer, model 450-AET.

Before executing the calibration, three settings have to be made on the radiometer. The first setting is related to the emissivity of the small region surrounding the thermocouple on the surface of the disc. The emissivity of the disc is selected by matching the temperature measured by the radiometer with the temperature measured by the thermocouple which is attached to the surface of the aluminum disc. As a precautionary measure, this procedure should not commence until the liquid nitrogen temperature and the dewar temperature have stabilized within the IR scanner or results

could be erroneous. This time is approximately 25 min.

After the thermometer and radiometer temperatures have been initialized by selecting the appropriate emissivity, the fast line scan mode is selected from the control unit. Since only horizontal scans occur in this mode, the thermocouple can be scanned continuously at high frequencies by the radiometer. The calibration must be executed in the fast line scan mode due to the vertical and horizontal line scans performed in the regular imaging mode which make it extremely difficult to later recover the appropriate voltage data values corresponding to the location of the thermocouple since the entire FOV is being scanned. In order to ensure that the exact location of the thermocouple on the surface of the disc was being scanned, the thermocouple was placed in a crevice extending across the diameter of the disc and positioned vertically in the FOV. The thermocouple was located as the darkest region in the FOV due to the higher emissive value associated with the crevice. After the thermocouple was located a temperature span of 50 °C was selected with a range from 15-65 °C.

The black aluminum heater unit was comprised of a type E thermocouple, an aluminum disc and a 10  $\Omega$  Minco thermofoil heater mounted on the backside of the plate using a thin layer of silicon grease. The heater element was aligned parallel to the same direction as the horizontal line scan to eliminate unwanted temperature gradients which might distort the location of the thermocouple. The heater was connected to a power supply where the temperature of the plate could be controlled.

Data was recorded on a CompuAdd 33 MHz, 486 PC which utilized the AT-MIO-16F5 data acquisition board. The board which contains 12 bit resolution A/D converters was driven by standard LabWindows data acquisition software. The radiometer output,

a standard RS-170 signal, was connected to the computer by a coaxial cable where voltage readings were recorded on the order of 1 volt. During execution of the calibration the power to the heater was increased until the thermometer temperature reached a maximum temperature of 65 °C. Every 2 °C, as the plate cooled, the data acquisition program was activated and the corresponding voltages were immediately plotted. The minimum voltage value in each of the scans which represents the temperature of the thermocouple was averaged over several scans. The voltage measured by the computer and the temperature measured by the thermocouple were then recorded and their relationship determined.

A disadvantage of the calibration is that data must be retrieved manually making the procedure quite time consuming, approximately 2 hrs/calibration. There are two main reasons for the unusual time needed to perform this calibration: 1) since the radiometer's scanning process is continuous and not synchronized with the data acquisition, one cannot predict at what time a particular line scan is recorded by the computer so the appropriate voltage values remain inaccessible without a visual display of the acquired data and 2) unwanted data values which come in the form of vertical refresh signals resemble legitimate line scans and can best be omitted through visual examination, see Figure A.2.

*Reproducibility:*

This calibration procedure was performed six times over a five day period. A plot of all six runs can be seen in Figure A.3. The standard deviation between the six individual calibration runs and the average represents a reproducibility within 0.65 °C. The emissivity which was determined for each individual calibration varied between 0.82

and 0.84.

*Temporal Resolution:*

The sample interval for the data acquisition system was set to its fastest rate of 227 kHz. The sample rate for the radiometer in the fast line scan mode is, however, much greater at 8 kHz/line with a horizontal resolution of 256 pixels/line. This results in a sample rate (pixels/sec) of approximately 2,048 kHz. The ratio between the radiometer sample rate and the data acquisition sample rate of nearly 10:1 results in a resolution of 10 voltage values per line scan as seen in Figure A.4.

*Thermal Resolution:*

The thermal resolution represents the smallest recognizable temperature increment. The smallest voltage increment detectable by the computer was found to be approximately 0.0024 volts. The calibrations represent an average sensitivity (slope) of 0.01 volts/°C, see Figure A.2. From this we can calculate the system's thermal resolution over a 50 °C span to be 0.24 °C.

*Relative Accuracy:*

In light of the fact that the radiometer was calibrated using the Omega thermometer as the temperature standard, we must base the success and usefulness of this calibration on a relative scale where the temperature measured by the thermocouple is treated as the accurate standard temperature. The relative accuracy which is defined here by the standard deviation between the six runs and the quadratic curve fit describing the

average was calculated to be approximately 0.55 °C. The curve of best fit calculated by *PLOTIT* was determined to be

$$T = -33.65742 * V^2 + 130.6025 * V - 2.446104,$$

where T is the calculated temperature and V is the measured voltage. The relative accuracy of ± 0.55 °C represents an error of approximately 1.4% (0.55/40) in this particular calibration.

Once the temperature versus voltage relationship has been determined, it can be entered into the PC data acquisition software allowing for voltage to temperature conversion and ultimately transient temperature measurement capability.

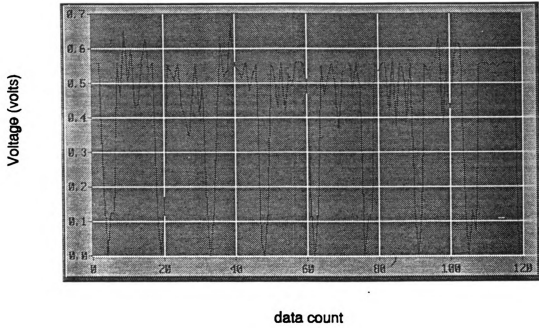
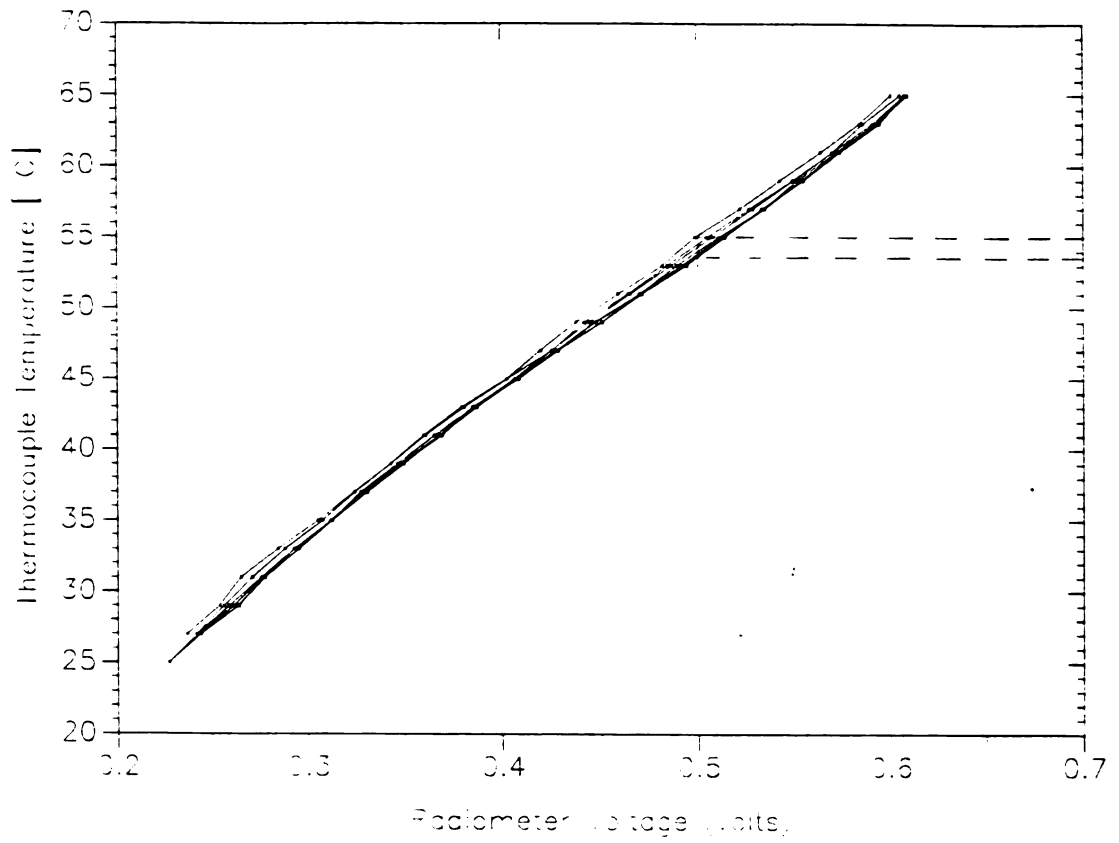


Figure A.2. Vertical refresh signals resembling legitimate line scans.



**Figure A.3.** Calibration of the 600L IR Radiometer for rapid transient thermal events.

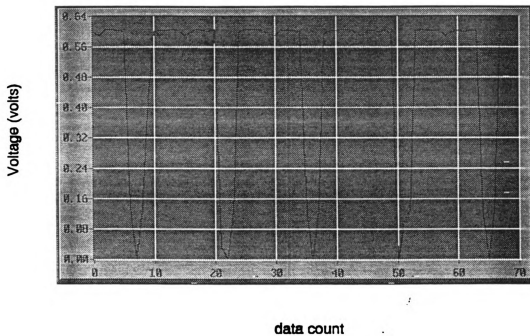


Figure A.4. Voltage output of radiometer during calibration.

## Appendix B.

## Temperature Distribution for Experiments 1-5

## Experiment #1

<u>r/b</u>	<u>Temp. (°C)</u>	<u>r/b</u>	<u>Temp. (°C)</u>	<u>r/b</u>	<u>Temp. (°C)</u>
-1.00000	25.33664	-.28302	26.65674	.43396	26.68793
-.98113	25.36899	-.26415	26.75034	.45283	26.78156
-.96226	25.27191	-.24528	26.78156	.47170	26.71915
-.94340	25.36899	-.22642	26.78156	.49057	26.56314
-.92453	25.36899	-.20755	26.78156	.50943	26.53192
-.90566	25.49594	-.18868	26.68793	.52830	26.59436
-.88679	25.52704	-.16981	26.53192	.54717	26.68793
-.86792	25.55817	-.15094	26.43680	.56604	26.56314
-.84906	25.58927	-.13208	26.37207	.58491	26.50073
-.83019	25.58927	-.11321	26.62555	.60377	26.53192
-.81132	25.65149	-.09434	26.87515	.62264	26.43680
-.79245	25.71372	-.07547	27.06235	.64151	26.37207
-.77359	25.71372	-.05660	27.12479	.66038	26.21155
-.75472	25.80707	-.03774	27.12479	.67925	26.18042
-.73585	25.83817	-.01887	27.03116	.69811	26.11820
-.71698	25.77594	.00000	27.06235	.71698	26.02484
-.69811	25.96262	.01887	26.90637	.73585	25.96262
-.67925	26.14929	.03774	26.78156	.75472	25.86929
-.66038	26.21155	.05660	26.81275	.77359	25.83817
-.64151	26.11820	.07547	26.78156	.79245	25.83817
-.62264	26.02484	.09434	26.71915	.81132	25.77594
-.60377	25.96262	.11321	26.71915	.83019	25.74484
-.58491	25.99375	.13208	26.75034	.84906	25.65149
-.56604	26.11820	.15094	26.84396	.86792	25.49594
-.54717	26.24265	.16981	26.87515	.88679	25.40134
-.52830	26.37207	.18868	26.90637	.90566	25.40134
-.50943	26.33972	.20755	26.87515	.92453	25.40134
-.49057	26.33972	.22642	26.84396	.94340	25.46481
-.47170	26.37207	.24528	26.81275	.96226	25.55817
-.45283	26.30734	.26415	26.65674	.98113	25.58927
-.43396	26.27500	.28302	26.46915	1.00000	25.55817
-.41509	26.21155	.30189	26.50073		
-.39623	26.05597	.32076	26.59436		
-.37736	26.18042	.33962	26.71915		
-.35849	26.30734	.35849	26.71915		
-.33962	26.40442	.37736	26.71915		
-.32076	26.46915	.39623	26.78156		
-.30189	26.56314	.41509	26.78156		

## Experiment #2

<u>r/b</u>	<u>Temp. (°C)</u>	<u>r/b</u>	<u>Temp. (°C)</u>	<u>r/b</u>	<u>Temp. (°C)</u>
-1.00000	25.55258	-.07547	28.36267	.84906	25.97327
-.98113	25.90854	-.05660	28.39389	.86792	26.00559
-.96226	26.03797	-.03774	28.48749	.88679	26.03797
-.94340	26.13504	-.01887	28.51868	.90566	26.07031
-.92453	26.03797	.00000	28.51868	.92453	26.10266
-.90566	26.00559	.01887	28.51868	.94340	26.16739
-.88679	26.00559	.03774	28.48749	.96226	26.00559
-.86792	26.16739	.05660	28.48749	.98113	25.87619
-.84906	26.26074	.07547	28.61621	1.00000	25.77908
-.83019	26.35407	.09434	28.61621		
-.81132	26.44742	.11321	28.51868		
-.79245	26.59857	.13208	28.17548		
-.77359	26.74860	.15094	27.92584		
-.75472	26.83859	.16981	27.67365		
-.73585	26.89862	.18868	27.80106		
-.71698	26.99109	.20755	27.98825		
-.69811	26.99109	.22642	28.20667		
-.67925	26.99109	.24528	28.30029		
-.66038	26.89862	.26415	28.23789		
-.64151	27.02362	.28302	28.08188		
-.62264	26.95862	.30189	27.86347		
-.60377	27.15360	.32076	27.80106		
-.58491	27.31613	.33962	27.92584		
-.56604	27.41364	.35849	28.05066		
-.54717	27.51114	.37736	28.11307		
-.52830	27.60864	.39623	28.05066		
-.50943	27.57614	.41509	27.95706		
-.49057	27.44614	.43396	27.89465		
-.47170	27.54364	.45283	27.80106		
-.45283	27.28363	.47170	27.73865		
-.43396	27.28363	.49057	27.73865		
-.41509	27.57614	.50943	27.64115		
-.39623	27.67365	.52830	27.67365		
-.37736	27.80106	.54717	27.51114		
-.35849	27.89465	.56604	27.34863		
-.33962	27.92584	.58491	27.28363		
-.32076	27.98825	.60377	27.21860		
-.30189	27.95706	.62264	27.25113		
-.28302	27.92584	.64151	27.28363		
-.26415	27.76987	.66038	27.28363		
-.24528	27.76987	.67925	27.15360		
-.22642	27.89465	.69811	27.12110		
-.20755	28.05066	.71698	27.12110		
-.18868	28.08188	.73585	27.05609		
-.16981	28.05066	.75472	26.99109		
-.15094	28.11307	.77359	26.89862		
-.13208	28.20667	.79245	26.53858		
-.11321	28.30029	.81132	26.26074		
-.09434	28.26907	.83019	26.10266		

## Experiment #3

<u>r/b</u>	<u>Temp. (°C)</u>	<u>r/b</u>	<u>Temp. (°C)</u>	<u>r/b</u>	<u>Temp. (°C)</u>
-1.00000	28.84396	-.07547	31.33441	.84906	29.13147
-.98113	28.90839	-.05660	31.14081	.86792	29.00507
-.96226	29.00507	-.03774	31.43247	.88679	28.90839
-.94340	29.03729	-.01887	31.62787	.90566	28.84396
-.92453	29.06873	.00000	31.75525	.92453	28.90839
-.90566	29.22559	.01887	31.94641	.94340	28.90839
-.88679	29.22559	.03774	31.97696	.96226	28.90839
-.86792	29.31973	.05660	32.00754	.98113	28.78076
-.84906	29.47662	.07547	31.78714	1.00000	28.59491
-.83019	29.53937	.09434	31.49783		
-.81132	29.63229	.11321	31.72342		
-.79245	29.75299	.13208	31.97696		
-.77359	29.84348	.15094	32.06870		
-.75472	29.96420	.16981	32.03812		
-.73585	30.08487	.18868	32.00754		
-.71698	30.17539	.20755	31.94641		
-.69811	30.11502	.22642	32.03812		
-.67925	30.17539	.24528	31.81897		
-.66038	30.20554	.26415	31.43247		
-.64151	30.14520	.28302	31.59589		
-.62264	30.35639	.30189	31.62787		
-.60377	30.50723	.32076	31.33441		
-.58491	30.68826	.33962	31.53052		
-.56604	30.56757	.35849	31.56320		
-.54717	30.56757	.37736	31.49783		
-.52830	30.86929	.39623	31.36710		
-.50943	31.08048	.41509	31.20368		
-.49057	31.20368	.43396	31.17099		
-.47170	31.14081	.45283	31.17099		
-.45283	31.23636	.47170	31.08048		
-.43396	31.33441	.49057	31.05029		
-.41509	31.43247	.50943	30.95981		
-.39623	31.39978	.52830	30.92963		
-.37736	31.30176	.54717	30.86929		
-.35849	31.26904	.56604	30.77878		
-.33962	31.39978	.58491	30.56757		
-.32076	31.43247	.60377	30.50723		
-.30189	31.43247	.62264	30.47705		
-.28302	31.56320	.64151	30.38657		
-.26415	31.72342	.66038	30.32623		
-.24528	31.65970	.67925	30.29605		
-.22642	31.56320	.69811	30.29605		
-.20755	31.46518	.71698	30.26590		
-.18868	31.43247	.73585	30.11502		
-.16981	31.56320	.75472	30.02454		
-.15094	31.75525	.77359	29.87366		
-.13208	31.72342	.79245	29.66248		
-.11321	31.56320	.81132	29.44525		
-.09434	31.30176	.83019	29.28836		

## Experiment #4

<u>r/b</u>	<u>Temp. (°C)</u>	<u>r/b</u>	<u>Temp. (°C)</u>	<u>r/b</u>	<u>Temp. (°C)</u>
-1.00000	24.45111	-.18333	26.22455	.63333	25.31482
-.98333	24.48221	-.16667	26.19345	.65000	25.28244
-.96667	24.45111	-.15000	26.00678	.66667	25.25012
-.95000	24.35779	-.13333	25.85120	.68333	25.44425
-.93333	24.26444	-.11667	25.85120	.70000	25.34717
-.91667	24.23334	-.10000	25.85120	.71667	25.25012
-.90000	24.23334	-.08333	25.69565	.73333	25.02362
-.88333	24.38889	-.06667	25.66452	.75000	24.82944
-.86667	24.57556	-.05000	25.63342	.76667	24.86182
-.85000	24.76474	-.03333	25.72675	.78333	24.99124
-.83333	24.99124	-.01667	25.82010	.80000	25.15302
-.81667	25.21774	.00000	25.69565	.81667	25.12067
-.80000	25.31482	.01667	25.66452	.83333	24.95886
-.78333	25.21774	.03333	25.72675	.85000	24.82944
-.76667	25.02362	.05000	25.85120	.86667	24.70001
-.75000	24.92655	.06667	26.06897	.88333	24.66892
-.73333	24.99124	.08333	26.25568	.90000	24.82944
-.71667	25.02362	.10000	26.25568	.91667	24.82944
-.70000	25.02362	.11667	26.10010	.93333	24.66892
-.68333	24.89417	.13333	25.97565	.95000	24.73236
-.66667	24.92655	.15000	25.88233	.96667	24.76474
-.65000	24.95886	.16667	25.94455	.98333	24.73236
-.63333	25.05594	.18333	26.03787	1.00000	24.70001
-.61667	25.25012	.20000	26.22455		
-.60000	25.31482	.21667	26.19345		
-.58333	25.31482	.23333	26.19345		
-.56667	25.34717	.25000	26.16232		
-.55000	25.37952	.26667	26.19345		
-.53333	25.37952	.28333	26.22455		
-.51667	25.37952	.30000	26.13123		
-.50000	25.31482	.31667	25.94455		
-.48333	25.34717	.33333	25.78897		
-.46667	25.41190	.35000	25.69565		
-.45000	25.50897	.36667	25.72675		
-.43333	25.66452	.38333	25.85120		
-.41667	25.75787	.40000	25.94455		
-.40000	25.78897	.41667	25.91342		
-.38333	25.85120	.43333	25.88233		
-.36667	25.78897	.45000	25.66452		
-.35000	25.57117	.46667	25.50897		
-.33333	25.50897	.48333	25.54007		
-.31667	25.66452	.50000	25.54007		
-.30000	25.75787	.51667	25.60230		
-.28333	25.72675	.53333	25.54007		
-.26667	25.75787	.55000	25.47659		
-.25000	25.82010	.56667	25.44425		
-.23333	25.88233	.58333	25.47659		
-.21667	26.03787	.60000	25.50897		
-.20000	26.19345	.61667	25.44425		

## Experiment #5

<u>r/b</u>	<u>Temp. (°C)</u>	<u>r/b</u>	<u>Temp. (°C)</u>	<u>r/b</u>	<u>Temp. (°C)</u>
-1.00000	27.55979	-.18333	31.01877	.63333	29.74909
-.98333	27.55979	-.16667	31.01877	.65000	29.68430
-.96667	27.59168	-.15000	30.86328	.66667	29.61951
-.95000	27.71942	-.13333	30.67676	.68333	29.58844
-.93333	27.81519	-.11667	30.55237	.70000	29.49515
-.91667	28.10010	-.10000	30.58344	.71667	29.37079
-.90000	28.22287	-.08333	30.83222	.73333	29.21530
-.88333	28.28427	-.06667	30.95661	.75000	29.09094
-.86667	28.13077	-.05000	30.86328	.76667	28.86878
-.85000	28.06940	-.03333	30.61453	.78333	28.65268
-.83333	28.19217	-.01667	30.61453	.80000	28.37637
-.81667	28.40708	.00000	30.61453	.81667	28.25357
-.80000	28.56055	.01667	30.67676	.83333	28.22287
-.78333	28.71405	.03333	30.70783	.85000	28.28427
-.76667	28.86878	.05000	30.73892	.86667	28.13077
-.75000	28.93265	.06667	30.83222	.88333	28.03870
-.73333	29.02844	.08333	30.83222	.90000	27.97482
-.71667	29.09094	.10000	30.80112	.91667	28.03870
-.70000	28.99649	.11667	30.64566	.93333	28.10010
-.68333	28.99649	.13333	30.67676	.95000	28.13077
-.66667	29.18421	.15000	30.77002	.96667	27.97482
-.65000	29.33969	.16667	30.89441	.98333	27.75134
-.63333	29.46405	.18333	31.04987	1.00000	27.49591
-.61667	29.52625	.20000	31.04987		
-.60000	29.46405	.21667	30.86328		
-.58333	29.43295	.23333	30.70783		
-.56667	29.49515	.25000	30.61453		
-.55000	29.46405	.26667	30.67676		
-.53333	29.84625	.28333	30.73892		
-.51667	30.23493	.30000	30.73892		
-.50000	30.39688	.31667	30.64566		
-.48333	30.20255	.33333	30.58344		
-.46667	30.04059	.35000	30.45908		
-.45000	29.91104	.36667	30.39688		
-.43333	30.23493	.38333	30.52127		
-.41667	30.42798	.40000	30.55237		
-.40000	30.45908	.41667	30.49017		
-.38333	30.45908	.43333	30.49017		
-.36667	30.52127	.45000	30.13776		
-.35000	30.49017	.46667	29.91104		
-.33333	30.55237	.48333	29.97580		
-.31667	30.67676	.50000	30.10538		
-.30000	30.67676	.51667	30.10538		
-.28333	30.67676	.53333	29.94342		
-.26667	30.67676	.55000	29.81387		
-.25000	30.67676	.56667	29.78146		
-.23333	30.70783	.58333	29.74909		
-.21667	30.77002	.60000	29.71668		
-.20000	30.83222	.61667	29.71668		

## Appendix C.

## PROGRAM NLIN

```

CCCCCCCC      PROGRAM DESCRIPTION      CCCCC
C
C      PROGRAM NLINC
C      WRITTEN BY JAMES V. BECK
C      LAST REVISED JUL. 27, 1993 FOR SCOTT HERR
C*****C
C
CVCCCCCCCC      VARIABLE IDENTIFICATION      CCCCCC
C
C*****C
C
CDCCCCCCCC      DIMENSION BLOCK      BLOCK 0000
C
C      IMPLICIT REAL*8 (A-H,O-Z)
C      DIMENSION T(500,5),Y(500),SIG2(500),B(5),Z(5),A(5),BS(5),
C      1VINV(5,5),BSS(5),CG(5),BSV(5),R(5,5),EXTRA(20),ERR(500)
C      1, PS(5,5),P(5,5),PSV(5,5),
C      1 XTX(5,5),XTY(5),SUM(5),BET(50,2)
C      CHARACTER*40 DFILE,OUTFIL
C
C*****C
C
COCCCCCCCC      COMMON BLOCK      BLOCK 0100
C
C      COMMON T,N,Z,BS,I,ETA,PS,P,B,A,Y,SIG2,MODL,VINV,NP,EXTRA
C      COMMON/ERROR/ERR
C      COMMON/MOD/AA,TL,SUM,BET,IH,CONST
C
C*****C
C
CACCCCCCCC      DATA BLOCK      BLOCK 0200
C
C      DATA EPS,EPSS,IIN,IOUT/1.0D-30,0.0001D+0,5,7/
C
C*****C
C
CICCCCCCCC      INITIALIZATION BLOCK      BLOCK 0400
C
C      WRITE(*,*)'ENTER THE NAME OF THE DATA FILE'
C      READ(*, '(A40)') DFILE
C      OPEN(8,FILE=DFILE)
C      WRITE(*,*)'ENTER THE NAME OF THE OUTPUT FILE'
C      READ(*, '(A40)') OUTFIL
C      OPEN(7,FILE=OUTFIL)
C
C*****C
C
CPCCCCCCCC      PROCESS BLOCK      BLOCK 0500
C
C --- START INPUT
C      BLOCK 1
C      WRITE(7,*)'BEGIN LISTING INPUT QUANTITIES'
200  READ(8,*) N,NP,NT,ITMAX,MODL,IPRINT
C      WRITE(7,*)
C      WRITE(7,*)'BLOCK 1'
C      WRITE(7,*)'N = NO. DATA POINTS, NP = NO. PARAMETERS'
C      WRITE(7,*)'NT = NO. OF INDEPENDENT VARIABLES'
C      WRITE(7,*)'ITMAX = MAXIMUM NO. OF ITERATIONS'
C      WRITE(7,*)'MODEL = MODEL NUMBER, IF SEVERAL MODELS IN SUBROUTINES:
C      1 MODEL AND SENS'
C      WRITE(7,*)'IPRINT = 1 FOR USUAL PRINTOUTS, 0 FOR LESS'
C      WRITE(7,*)
C      IF(N.LE.0) THEN
C          STOP
C      END IF
C      WRITE(*, '(/,9X, ''N'',8X, ''NP'',8X, ''NT'',5X, ''ITMAX'',5X,
C      +''MODEL'',4X, ''IPRINT'')')
C      WRITE(*, '(7I10)') N,NP,NT,ITMAX,MODL,IPRINT

```

```

WRITE(7, '(/, 9X, ''N'', 8X, ''NP'', 8X, ''NT'', 5X, ''ITMAX'', 5X,
+''MODEL'', 4X, ''IPRINT'')')
WRITE(7, '(7I10)') N, NP, NT, ITMAX, MODL, IPRINT
IOPT=0
C --- IF IOPT=0 THEN ON THE 2ND AND SUCCEEDING STACKED CASES, THE DATA IS
C --- NOT REPRINTED.
C --- IF IPRINT=1, EXTRA PRINT OUT OF ETA, RESIDUALS B(1),... ARE GIVEN.
C
C BLOCK 2
WRITE(7, *)
WRITE(7, *) 'BLOCK 2'
WRITE(7, *) 'B(1), B(2), ..., B(NP) ARE INITIAL PARAMETER ESTIMATES'
WRITE(7, *)
READ(8, *) (B(I), I=1, NP)
WRITE(7, '(10X, ''B('', I1, ''') = '', E16.5)') (I, B(I), I=1, NP)
C
DO 150 J1=2, 5
  BS(J1) = 0
150 CONTINUE
C
IF (IOPT.LE.0) THEN
C BLOCK 3
WRITE(7, *)
WRITE(7, *) 'BLOCK 3'
WRITE(7, *) 'J = DATA POINT INDEX, Y(J) = MEASURED VALUE'
WRITE(7, *) 'SIGMA(J) = STANDARD DEVIATION OF Y(J)'
WRITE(7, *) 'T(J,1) = FIRST INDEPENDENT VARIABLE'
WRITE(7, *)
WRITE(7, '(/, 9X, ''J'', 6X, ''Y(J)'', 3X, ''SIGMA(J)'', 6X, ''T(J,1)'',
+ , 6X, ''T(J,2)'')')
DO 10 I2=1, N
  READ(8, *) J, Y(J), SIG2(J), (T(J, KT), KT=1, NT)
  WRITE(7, '(I10, 7F10.5)') J, Y(J), SIG2(J), (T(J, KT), KT=1, NT)
  SIG2(J) = SIG2(J)*SIG2(J)
10 CONTINUE
END IF
C
C 313 DO 2 IP=1, NP
DO 2 KP=1, NP
  PS(KP, IP) = 0
  P(KP, IP) = 0
2 CONTINUE
C
WRITE(7, '(/, 5X, ''P(1, KP)'', 9X, ''P(2, KP)'', 9X, ''P(3, KP)'', 9X,
+ ''P(4, KP)'', 9X, ''P(5, KP)'')')
C
DO 6 IP=1, NP
C
  READ(8, *) (PS(IP, KP), KP=1, NP)
  WRITE(7, '(5D16.5)') (PS(IP, KP), KP=1, NP)
6 CONTINUE
C
C BLOCK 4
DO 88 IP=1, NP
  PS(IP, IP) = B(IP)*B(IP)
88 READ(8, *) IEXTRA
C
IEXTRA=0 FOR NO EXTRA INPUT WHICH COULD BE FOR CONSTANTS
C
IN MODELS
C
=1 FOR ONE INPUT, NAMELY: EXTRA(1), ETC.
WRITE(7, *)
WRITE(7, *) 'BLOCK 4'
WRITE(7, *) 'IEXTRA = NO. OF EXTRA(I) PARAMETERS, 0 IF NONE'
WRITE(7, *)
WRITE(7, '(10X, ''IEXTRA = '', I10)') IEXTRA
IF (IEXTRA .LT. 1) GOTO 21
WRITE(7, *)
WRITE(7, *) 'BLOCK 5'
WRITE(7, *) 'EXTRA(1), ... ARE EXTRA CONSTANTS USED AS DESIRED'
WRITE(7, *)
READ(8, *) (EXTRA(IE), IE=1, IEXTRA)
WRITE(7, '( ''EXTRA('', I2, ''') = '', F16.5)') (IE, EXTRA(IE), IE=1
1, IEXTRA)
21 CONTINUE
C
C --- ADD BLANK CARD AFTER LAST INPUT CARD
C ---END INPUT
WRITE(7, *) 'END INPUT QUANTITIES - - BEGIN OUTPUT CALCULATIONS'
WRITE(7, *)
WRITE(7, *) 'SY = SUM OF SQUARES FOR PRESENT PARAMETER VALUES'
WRITE(7, *) 'SYP = SUM OF SQUARES FOR GAUSS PARAMETER VALUES, SHOULD
1 BE SMALLER THAN SY'
WRITE(7, *) 'SYP DECREASES TOWARD A POSITIVE CONSTANT'
WRITE(7, *) 'G = MEASURE OF THE SLOPE, SHOULD BECOME SMALLER AS
1 ITERATIONS PROCEED'

```

```

WRITE(7,*)'      G SHOULD APPROACH ZERO AT CONVERGENCE'
WRITE(7,*)'H =   FRACTION OF THE GAUSS STEP, AS GIVEN BY THE
1BOX-KANEMASU METHOD'
WRITE(7,*)
WRITE(7,*)
DO 18 IL=1,NP
  BS(IL)=B(IL)
  CG(IL) = 0
18  CONTINUE
DO 19 IP=1,NP
  XTY(IP)=0.0D+0
  DO 19 KP=1,NP
    P(KP,IP) = PS(KP,IP)
    XTX(IP,KP)=0.0D+0
19  CONTINUE
  I = 0
  MAX = 0
C
99  MAX = MAX + 1
C --- START BASIC LOOP GIVES B(I) AND SY
C
  SY = 0.0D+0
  DO 100 I3=1,N
    I = I3
    CALL MODEL
    CALL SENS
CCCC  CALL MODEL
    RISD = Y(I)-ETA
    SY = SY + RISD*RISD/SIG2(I)
    SUMX= 0.0D+0
    DO 20 K=1,NP
      XTY(K)=XTY(K)+Z(K)*RISD/SIG2(I)
      DO 20 L=1,NP
        SUMX= SUMX+ Z(L)*P(K,L)*Z(K)
        XTX(K,L)= XTX(K,L) + Z(L)*Z(K)/SIG2(I)
20    CONTINUE
      DELTA = SIG2(I) + SUMX
      DO 29 JJ=1,NP
        A(JJ) = 0.0D+0
29    CONTINUE
      DO 30 JA=1,NP
        DO 30 KA=1,NP
          A(JA) = A(JA) + Z(KA)*P(JA,KA)
30    CONTINUE
      CS = 0.0D+0
      DO 40 JC=1,NP
        CS = CS + Z(JC)*(B(JC)-BS(JC))
        CG(JC) = CG(JC) + Z(JC)*RISD/SIG2(I)
40    CONTINUE
      C = Y(I) - CS - ETA
      DO 50 IB=1,NP
        B(IB) = B(IB) + (A(IB)*C)/DELTA
50    CONTINUE
      DO 41 ISV=1,NP
        DO 41 JSV=1,NP
          PSV(JSV,ISV) = P(JSV,ISV)
41    CONTINUE
      DO 52 IV=1,NP
        DO 52 IU=IV,NP
          SUMP = 0.0D+0
          DO 51 KP=1,NP
            DO 51 JP=1,NP
              IF (KP-IV.EQ.0.OR.JP-IU.EQ.0) GOTO 51
              PSQ1 = PSV(KP,JP)*PSV(IU,IV)
              PSQ2 = PSV(IU,KP)*PSV(IV,JP)
              PSQ = PSQ1 - PSQ2
              IF (DABS(PSQ1)+DABS(PSQ2).LT.1.D-15) THEN
                RP = PSQ * 1.D15
              ELSE
                RP = PSQ / (DABS(PSQ1)+DABS(PSQ2))
              END IF
              RP = ABS(RP)
              RPP = RP - 1.0D-12
              IF (RPP.LE.0.0D+0) THEN
                PSQ = 0.0D+0
              END IF
              SUMP = SUMP + Z(JP)*Z(KP)*PSQ
51    CONTINUE
          P(IU,IV) = (PSV(IU,IV)*SIG2(I)+SUMP)/DELTA
52    CONTINUE

```

```

DO 53 IV=2,NP
  IVM = IV - 1
  DO 53 IU = 1,IVM
    P(IU,IV)= P(IV,IU)
53  CONTINUE
    IF(IPRINT.GT.0) THEN
      IF(I.EQ.1) THEN
        WRITE(7,*)
        WRITE(7,*)'SEQUENTIAL ESTIMATES OF THE PARAMETERS GIVEN BELOW'
        WRITE(7,'(//,3X,'I'',6X,'ETA'',3X,'RES.'',2X,
1'B(1)'',7X,'B(2)'',7X,'B(3)'',7X,'B(4)'')')
        END IF
C      WRITE(7,'(I4,6E12.5')I,ETA,RISD,(B(JC),JC=1,NP)
        WRITE(7,'(I3,F10.2,F8.3,5E11.4')I,ETA,RISD,(B(JC),JC=1,NP)
        END IF
100  CONTINUE
C --- END BASIC LOOP, GIVES B(I) AND SY
C --- START BOX-KANEMASU MODIFICATION
C
C      START BOX-KANEMASU MODIFICATION
      IF(MAX-1)104,104,103
      SS=SY/2.0D+0
103  IF(SS-SYP)104,104,105
105  DO 210 IBS=1,NP
        B(IBS)= BSV(IBS)
210  CONTINUE
        WRITE(IOUT,212)
212  FORMAT(7X,'USE BSV(IBS)')
        GOTO 211
104  CONTINUE
      DO 102 IBS=1,NP
        BSS(IBS)= BS(IBS)
102  CONTINUE
        ALPHA= 2.0D+0
        AA= 1.1D+0
110  ALPHA= ALPHA/2.0D+0
      DO 116 IBS=1,NP
        BS(IBS)= BSS(IBS) + ALPHA*( B(IBS)-BSS(IBS) )
        BSV(IBS)= BS(IBS)
116  CONTINUE
        INDEX=0
        G= 0.0D+0
      DO 115 IP=1,NP
        DELB= BS(IP)-BSS(IP)
        G= G + DELB*CG(IP)
        RATIO= DELB/( BSS(IP)+EPS )
        RATIO= ABS(RATIO)
        IF(RATIO-EPSS)113,113,114
113  INDEX= INDEX+1
        WRITE(IOUT,314)
314  FORMAT(7X,'MAX',8X,'NP',5X,'INDEX',8X,'IP')
        WRITE(7,'(7I10)') MAX,NP,INDEX,IP
114  CONTINUE
C      WRITE(7,122) I,Y(I),ETA,RISD,Z(IP),XYP,DELB,SIG2(I)
115  CONTINUE
        SYP= 0.0D+0
      DO 117 I3=1,N
        I=I3
        CALL MODEL
        RISD= Y(I)-ETA
        SYP= SYP + RISD*RISD/SIG2(I)
117  CONTINUE
      IF(NP-INDEX)106,106,107
106  H=1.0D+0
      GOTO 132
107  CONTINUE
        SYN= SYP*0.999D+0
        IF(SYN-SY)112,112,111
111  IF(ALPHA-0.01D+0)109,109,110
109  WRITE(7,108) ALPHA,SYP,SY
108  FORMAT(3X,'ALPHA TOO SMALL,ALPHA=',F12.6,2X,'SYP=',E15.6,2X,
1'SY',E15.6)
        WRITE(7,1001)
1001  FORMAT(8X,'Z(1)',10X,'Z(2)',10X,'Z(3)',10X,'Z(4)',10X,'Z(5)')
1002  FORMAT(6E13.4)
      DO 1003 I=1,N
        CALL SENS
        WRITE(7,1002) (Z(IBB),IBB=1,NP)
1003  CONTINUE
      GOTO 1000

```

```

112 CONTINUE
    SKSUM= SY - ALPHA*G*( 2.0D+0-1.0D+0/AA )
    IF (SYP-SKSUM) 131,131,130
130 H= ALPHA * ALPHA*G/( SYP-SY+2.0D+0*ALPHA*G )
    GOTO 132
131 CONTINUE
    H= ALPHA*AA
132 CONTINUE
    DO 118 IBN= 1,NP
        B(IBN)= BSS(IBN) + H * ( B(IBN)-BSS(IBN) )
118 CONTINUE
211 CONTINUE
    WRITE(IOUT,121)
    WRITE(*,121)
121 FORMAT(5X,'MAX',10X,'H',13X,'G',12X,
1'SY',11X,'SYP')
    WRITE(7,122) MAX,H,G,SY,SYP
    WRITE(*,122) MAX,H,G,SY,SYP
122 FORMAT(I8,1F13.6,4E14.6)
    WRITE(7,'(10X,'B('',I1,'') = '',E16.6)') (I,B(I),I=1,NP)
    WRITE(*,'(10X,'B('',I1,'') = '',E16.6)') (I,B(I),I=1,NP)
C     END     BOX-KANEMASU MODIFICATION
    WRITE(7,'(/,5X,'P(1,KP)',9X,'P(2,KP)',9X,'P(3,KP)',9X,
1'P(4,KP)',9X,'P(5,KP)')')
    DO 206 IP=1,NP
        WRITE(7,207) (P(IP,KP),KP=1,NP)
206 CONTINUE
207 FORMAT(5D15.7)
    WRITE(7,135)
135 FORMAT(5X,'CORRELATION MATRIX')
    DO 136 IR=1,NP
        DO 136 IR2=1,IR
            AR= P(IR,IR) * P(IR2,IR2)
            R(IR,IR2)= P(IR,IR2)/SQRT(AR)
136 CONTINUE
    DO 137 IR=1,NP
        WRITE(7,'(5E15.7)') (R(IR,III),III=1,IR)
137 CONTINUE
    DO 126 IPS=1,NP
        PS(IPS,IPS)= (1.0E+7) * P(IPS,IPS)
126 CONTINUE
    WRITE(7,*)'XTX(I,K),K=1,NP'
    DO 220 K=1,NP
220 WRITE(7,'(5E15.7)') (XTX(K,III),III=1,NP)
    WRITE(7,*)'XTY(I),I=1,NP, WHERE Y IS RESID'
    WRITE(7,'(5E15.7)') (XTY(I),I=1,NP)
127 FORMAT(3X,'IPS=',I4,3X,'PS(IPS,IPS)=' ,D15.8)
    WRITE(7,*)'XTY(I),I=1,NP, Y IS Y, NOT RESID'
    WRITE(7,'(5E15.7)') (SUM(I),I=1,NP)
    DO 119 IP=1,NP
        XTY(IP)=0.0D+0
        DO 119 KP=1,NP
            P(IP,KP)= PS(IP,KP)
            XTX(IP,KP)=0.0D+0
119 CONTINUE
    DO 120 IP=1,NP
        BS(IP)= B(IP)
        CG(IP)= 0.0D+0
120 CONTINUE
    WRITE(7,314)
    WRITE(7,'(7I10,4F10.4)') MAX,NP,INDEX,IP
    IF (NP-INDEX) 101,101,123
123 CONTINUE
    M=ITMAX
    IF (MAX-M) 99,99,101
101 CONTINUE
    IF (IPRINT) 133,133,134
133 IPRINT=IPRINT+1
    GOTO 99
134 CONTINUE
C
1000 CONTINUE
    CLOSE(IIN)
    CLOSE(IOUT)
C
C*****
C
C     CECCCCCCC          ERROR MESSAGES          BLOCK 0900
C
C
C

```

```

C*****C
C
CFCCCCCCCC          FORMAT STATEMENTS          BLOCK 9000
C
C
C*****C
C
      STOP
      END
      SUBROUTINE MODEL
C   THIS SUBROUTINE IS FOR CALCULATING ETA, THE MODEL VALUE
      IMPLICIT REAL*8 (A-H,O-Z)
      DIMENSION T(500,5),Y(500),SIG2(500),B(5),Z(5),BET(50,2),
+A(5),BS(5),VINV(5,5),EXTRA(20)
      DIMENSION P(5,5),PS(5,5),SUM(5)
      COMMON T,N,Z,BS,I,ETA,PS,P,B,A,Y,SIG2,MODL,VINV,NP,EXTRA
      COMMON/MOD/AA,TL,SUM,BET,IH,CONST
C   WRITTEN BY JAMES V. BECK
      PI=4.0D+0*DATAN(1.0D+0)
C   IF(MODL .EQ. 1) GOTO 800
800   CONTINUE
      TR=T(I,1)/EXTRA(2)
      ETA=BS(1)+BS(2)*EXTRA(1)*(1.0D+0-TR*TR)
1000  CONTINUE
C   WRITE(*,*)'I,T(I,1),ETA,Z(1)',I,T(I,1),ETA,Z(1)
      RETURN
      END
      SUBROUTINE SENS
C   THIS SUBROUTINE IS FOR CALCULATING THE SENSITIVITY COEFFICIENTS
      IMPLICIT REAL*8 (A-H,O-Z)
      DIMENSION T(500,5),Y(500),SIG2(500),B(5),BET(50,2),
+Z(5),A(5),BS(5),VINV(5,5),EXTRA(20)
      DIMENSION P(5,5),PS(5,5),SUM(5)
      COMMON T,N,Z,BS,I,ETA,PS,P,B,A,Y,SIG2,MODL,VINV,NP,EXTRA
      COMMON/MOD/AA,TL,SUM,BET,IH,CONST
      PI=4.0D+0*DATAN(1.0D+0)
      Z(1)=1.0D+0
      TR=T(I,1)/EXTRA(2)
      Z(2)=EXTRA(1)*(1.0D+0-TR*TR)
      DO 312 IPP=1,NP
312   SUM(IPP)=0.0D+0
313   CONTINUE
800   CONTINUE
C   IF(I .LT. N)GOTO 2000
      DO 1001 JPP=1,NP
C   TZ=? TRY ETA FOR NOW
      TZ=ETA
1001  SUM(JPP)=SUM(JPP)+Z(JPP)*(Y(I)-TZ)/SIG2(I)
2000  CONTINUE
      RETURN
      END

```

## Appendix D.

## NLIN Output File for Experiment #5

BEGIN LISTING INPUT QUANTITIES

BLOCK 1

N = NO. DATA POINTS, NP = NO. PARAMETERS  
 NT = NO. OF INDEPENDENT VARIABLES  
 ITMAX = MAXIMUM NO. OF ITERATIONS  
 MODEL = MODEL NUMBER, IF SEVERAL MODELS IN SUBROUTINES: MODEL AND SENS  
 IPRINT = 1 FOR USUAL PRINTOUTS, 0 FOR LESS

N	NP	NT	ITMAX	MODEL	IPRINT
121	2	1	5	1	1

BLOCK 2

B(1),B(2),...,B(NP) ARE INITIAL PARAMETER ESTIMATES

B(1) =	.27500E+02
B(2) =	.40000E-02

BLOCK 3

J = DATA POINT INDEX, Y(J) = MEASURED VALUE  
 SIGMA(J) = STANDARD DEVIATION OF Y(J)  
 T(J,1) = FIRST INDEPENDENT VARIABLE

J	Y(J)	SIGMA(J)	T(J,1)	T(J,2)
1	27.55979	1.00000	-1.00000	
2	27.55979	1.00000	-.98333	
3	27.59168	1.00000	-.96667	
4	27.71942	1.00000	-.95000	
5	27.81519	1.00000	-.93333	
6	28.10010	1.00000	-.91667	
7	28.22287	1.00000	-.90000	
8	28.28427	1.00000	-.88333	
9	28.13077	1.00000	-.86667	
10	28.06940	1.00000	-.85000	
11	28.19217	1.00000	-.83333	
12	28.40708	1.00000	-.81667	
13	28.56055	1.00000	-.80000	
14	28.71405	1.00000	-.78333	
15	28.86878	1.00000	-.76667	
16	28.93265	1.00000	-.75000	
17	29.02844	1.00000	-.73333	
18	29.09094	1.00000	-.71667	
19	28.99649	1.00000	-.70000	
20	28.99649	1.00000	-.68333	
21	29.18421	1.00000	-.66667	
22	29.33969	1.00000	-.65000	
23	29.46405	1.00000	-.63333	
24	29.52625	1.00000	-.61667	
25	29.46405	1.00000	-.60000	
26	29.43295	1.00000	-.58333	
27	29.49515	1.00000	-.56667	
28	29.46405	1.00000	-.55000	
29	29.84625	1.00000	-.53333	
30	30.23493	1.00000	-.51667	
31	30.39688	1.00000	-.50000	
32	30.20255	1.00000	-.48333	
33	30.04059	1.00000	-.46667	
34	29.91104	1.00000	-.45000	
35	30.23493	1.00000	-.43333	
36	30.42798	1.00000	-.41667	
37	30.45908	1.00000	-.40000	
38	30.45908	1.00000	-.38333	
39	30.52127	1.00000	-.36667	
40	30.49017	1.00000	-.35000	
41	30.55237	1.00000	-.33333	
42	30.67676	1.00000	-.31667	
43	30.67676	1.00000	-.30000	
44	30.67676	1.00000	-.28333	

45	30.67676	1.00000	-.26667
46	30.67676	1.00000	-.25000
47	30.70783	1.00000	-.23333
48	30.77002	1.00000	-.21667
49	30.83222	1.00000	-.20000
50	31.01877	1.00000	-.18333
51	31.01877	1.00000	-.16667
52	30.86328	1.00000	-.15000
53	30.67676	1.00000	-.13333
54	30.55237	1.00000	-.11667
55	30.58344	1.00000	-.10000
56	30.83222	1.00000	-.08333
57	30.95661	1.00000	-.06667
58	30.86328	1.00000	-.05000
59	30.61453	1.00000	-.03333
60	30.61453	1.00000	-.01667
61	30.61453	1.00000	.00000
62	30.67676	1.00000	.01667
63	30.70783	1.00000	.03333
64	30.73892	1.00000	.05000
65	30.83222	1.00000	.06667
66	30.83222	1.00000	.08333
67	30.80112	1.00000	.10000
68	30.64566	1.00000	.11667
69	30.67676	1.00000	.13333
70	30.77002	1.00000	.15000
71	30.89441	1.00000	.16667
72	31.04987	1.00000	.18333
73	31.04987	1.00000	.20000
74	30.86328	1.00000	.21667
75	30.70783	1.00000	.23333
76	30.61453	1.00000	.25000
77	30.67676	1.00000	.26667
78	30.73892	1.00000	.28333
79	30.73892	1.00000	.30000
80	30.64566	1.00000	.31667
81	30.58344	1.00000	.33333
82	30.45908	1.00000	.35000
83	30.39688	1.00000	.36667
84	30.52127	1.00000	.38333
85	30.55237	1.00000	.40000
86	30.49017	1.00000	.41667
87	30.49017	1.00000	.43333
88	30.13776	1.00000	.45000
89	29.91104	1.00000	.46667
90	29.97580	1.00000	.48333
91	30.10538	1.00000	.50000
92	30.10538	1.00000	.51667
93	29.94342	1.00000	.53333
94	29.81387	1.00000	.55000
95	29.78146	1.00000	.56667
96	29.74909	1.00000	.58333
97	29.71668	1.00000	.60000
98	29.71668	1.00000	.61667
99	29.74909	1.00000	.63333
100	29.68430	1.00000	.65000
101	29.61951	1.00000	.66667
102	29.58844	1.00000	.68333
103	29.49515	1.00000	.70000
104	29.37079	1.00000	.71667
105	29.21530	1.00000	.73333
106	29.09094	1.00000	.75000
107	28.86878	1.00000	.76667
108	28.65268	1.00000	.78333
109	28.37637	1.00000	.80000
110	28.25357	1.00000	.81667
111	28.22287	1.00000	.83333
112	28.28427	1.00000	.85000
113	28.13077	1.00000	.86667
114	28.03870	1.00000	.88333
115	27.97482	1.00000	.90000
116	28.03870	1.00000	.91667
117	28.10010	1.00000	.93333
118	28.13077	1.00000	.95000
119	27.97482	1.00000	.96667
120	27.75134	1.00000	.98333
121	27.49591	1.00000	1.00000

BLOCK 4

IEXTRA = NO. OF EXTRA(I) PARAMETERS, 0 IF NONE

IEXTRA = 2

BLOCK 5  
EXTRA(1),... ARE EXTRA CONSTANTS USED AS DESIRED

EXTRA( 1) = 831.86000  
EXTRA( 2) = 1.00000  
END INPUT QUANTITIES - - BEGIN OUTPUT CALCULATIONS

SY = SUM OF SQUARES FOR PRESENT PARAMETER VALUES  
SYP = SUM OF SQUARES FOR GAUSS PARAMETER VALUES, SHOULD BE SMALLER THAN SY  
SYP DECREASES TOWARD A POSITIVE CONSTANT  
G = MEASURE OF THE SLOPE, SHOULD BECOME SMALLER AS ITERATIONS PROCEED  
G SHOULD APPROACH ZERO AT CONVERGENCE  
H = FRACTION OF THE GAUSS STEP, AS GIVEN BY THE BOX-KANEMASU METHOD

SEQUENTIAL ESTIMATES OF THE PARAMETERS GIVEN BELOW

I	ETA	RES.	B(1)	B(2)	B(3)	B(4)
1	27.50	.060	.2756E+02	.4000E-02		
2	27.61	-.050	.2751E+02	.3976E-02		
3	27.72	-.126	.2746E+02	.3921E-02		
4	27.82	-.105	.2745E+02	.3883E-02		
5	27.93	-.114	.2744E+02	.3844E-02		
6	28.03	.069	.2746E+02	.3974E-02		
7	28.13	.091	.2747E+02	.4105E-02		
8	28.23	.053	.2747E+02	.4171E-02		
9	28.33	-.197	.2747E+02	.3973E-02		
10	28.42	-.354	.2747E+02	.3669E-02		
11	28.52	-.325	.2748E+02	.3473E-02		
12	28.61	-.201	.2748E+02	.3444E-02		
13	28.70	-.137	.2748E+02	.3485E-02		
14	28.79	-.072	.2747E+02	.3574E-02		
15	28.87	-.003	.2746E+02	.3698E-02		
16	28.96	-.023	.2745E+02	.3782E-02		
17	29.04	-.010	.2744E+02	.3857E-02		
18	29.12	-.027	.2744E+02	.3906E-02		
19	29.20	-.201	.2744E+02	.3854E-02		
20	29.27	-.277	.2745E+02	.3777E-02		
21	29.35	-.164	.2746E+02	.3770E-02		
22	29.42	-.082	.2745E+02	.3800E-02		
23	29.49	-.029	.2744E+02	.3848E-02		
24	29.56	-.036	.2744E+02	.3884E-02		
25	29.63	-.166	.2744E+02	.3870E-02		
26	29.70	-.262	.2745E+02	.3827E-02		
27	29.76	-.264	.2745E+02	.3792E-02		
28	29.82	-.357	.2747E+02	.3737E-02		
29	29.88	-.035	.2746E+02	.3780E-02		
30	29.94	.296	.2743E+02	.3901E-02		
31	30.00	.401	.2740E+02	.4031E-02		
32	30.05	.152	.2739E+02	.4084E-02		
33	30.10	-.062	.2739E+02	.4082E-02		
34	30.15	-.243	.2740E+02	.4042E-02		
35	30.20	.032	.2740E+02	.4062E-02		
36	30.25	.178	.2739E+02	.4107E-02		
37	30.30	.164	.2738E+02	.4144E-02		
38	30.34	.121	.2737E+02	.4168E-02		
39	30.38	.141	.2736E+02	.4192E-02		
40	30.42	.070	.2736E+02	.4203E-02		
41	30.46	.095	.2736E+02	.4215E-02		
42	30.49	.183	.2735E+02	.4239E-02		
43	30.53	.149	.2735E+02	.4255E-02		
44	30.56	.116	.2735E+02	.4264E-02		
45	30.59	.086	.2734E+02	.4269E-02		
46	30.62	.057	.2734E+02	.4270E-02		
47	30.65	.062	.2734E+02	.4270E-02		
48	30.67	.099	.2734E+02	.4275E-02		
49	30.69	.138	.2734E+02	.4283E-02		
50	30.72	.303	.2733E+02	.4308E-02		
51	30.74	.284	.2733E+02	.4329E-02		
52	30.75	.111	.2733E+02	.4330E-02		
53	30.77	-.092	.2733E+02	.4313E-02		
54	30.78	-.230	.2734E+02	.4284E-02		
55	30.79	-.211	.2735E+02	.4259E-02		
56	30.80	.028	.2735E+02	.4256E-02		
57	30.81	.144	.2735E+02	.4263E-02		

58	30.82	.044	.2735E+02	.4261E-02
59	30.82	-.209	.2735E+02	.4240E-02
60	30.83	-.212	.2736E+02	.4221E-02
61	30.83	-.213	.2737E+02	.4203E-02
62	30.83	-.150	.2737E+02	.4190E-02
63	30.82	-.116	.2737E+02	.4181E-02
64	30.82	-.080	.2737E+02	.4174E-02
65	30.81	.020	.2737E+02	.4174E-02
66	30.80	.028	.2737E+02	.4175E-02
67	30.79	.007	.2737E+02	.4174E-02
68	30.78	-.136	.2738E+02	.4166E-02
69	30.77	-.092	.2738E+02	.4160E-02
70	30.75	.017	.2738E+02	.4161E-02
71	30.74	.159	.2738E+02	.4168E-02
72	30.72	.334	.2737E+02	.4183E-02
73	30.69	.356	.2737E+02	.4197E-02
74	30.67	.192	.2737E+02	.4204E-02
75	30.65	.062	.2737E+02	.4205E-02
76	30.62	-.005	.2737E+02	.4204E-02
77	30.59	.086	.2737E+02	.4206E-02
78	30.56	.179	.2737E+02	.4211E-02
79	30.53	.211	.2736E+02	.4217E-02
80	30.49	.152	.2736E+02	.4221E-02
81	30.46	.126	.2736E+02	.4223E-02
82	30.42	.039	.2736E+02	.4223E-02
83	30.38	.017	.2736E+02	.4223E-02
84	30.34	.183	.2736E+02	.4226E-02
85	30.30	.257	.2736E+02	.4230E-02
86	30.25	.240	.2736E+02	.4233E-02
87	30.20	.288	.2737E+02	.4236E-02
88	30.15	-.016	.2737E+02	.4236E-02
89	30.10	-.192	.2736E+02	.4235E-02
90	30.05	-.074	.2736E+02	.4234E-02
91	30.00	.110	.2736E+02	.4234E-02
92	29.94	.166	.2737E+02	.4234E-02
93	29.88	.062	.2737E+02	.4234E-02
94	29.82	-.007	.2737E+02	.4234E-02
95	29.76	.022	.2737E+02	.4234E-02
96	29.70	.054	.2737E+02	.4233E-02
97	29.63	.087	.2737E+02	.4231E-02
98	29.56	.155	.2737E+02	.4228E-02
99	29.49	.256	.2738E+02	.4221E-02
100	29.42	.263	.2739E+02	.4214E-02
101	29.35	.271	.2740E+02	.4206E-02
102	29.27	.315	.2741E+02	.4195E-02
103	29.20	.298	.2742E+02	.4183E-02
104	29.12	.252	.2742E+02	.4173E-02
105	29.04	.177	.2743E+02	.4165E-02
106	28.96	.135	.2744E+02	.4158E-02
107	28.87	-.003	.2744E+02	.4158E-02
108	28.79	-.133	.2743E+02	.4164E-02
109	28.70	-.322	.2742E+02	.4181E-02
110	28.61	-.355	.2741E+02	.4199E-02
111	28.52	-.294	.2739E+02	.4214E-02
112	28.42	-.139	.2739E+02	.4219E-02
113	28.33	-.197	.2738E+02	.4227E-02
114	28.23	-.192	.2738E+02	.4235E-02
115	28.13	-.157	.2738E+02	.4240E-02
116	28.03	.007	.2738E+02	.4233E-02
117	27.93	.171	.2739E+02	.4215E-02
118	27.82	.306	.2741E+02	.4187E-02
119	27.72	.257	.2743E+02	.4164E-02
120	27.61	.141	.2744E+02	.4149E-02
121	27.50	-.004	.2744E+02	.4145E-02

MAX	H	G	SY	SYP
1	1.006253	.211317E+00	.387968E+01	.366705E+01
	B (1) =	.274402E+02		
	B (2) =	.414560E-02		

P (1, KP)	P (2, KP)	P (3, KP)	P (4, KP)	P (5, KP)
.4726766D-01	-.7092205D-04			
-.7092205D-04	.1289619D-06			
CORRELATION MATRIX				
.1000000E+01				
-.9083821E+00	.1000000E+01			
XTX (I, K), K=1, NP				
.1210000E+03	.6654418E+05			
.6654418E+05	.4428743E+08			
XTY (I), I=1, NP, WHERE Y IS RESID				
.2434174E+01	.2460668E+04			

XTY(I), I=1, NP, Y IS Y, NOT RESID  
 -.4090000E-02 .0000000E+00  
 MAX NP INDEX IP  
 1 2 0 3

SEQUENTIAL ESTIMATES OF THE PARAMETERS GIVEN BELOW

I	ETA	RES.	B(1)	B(2)	B(3)	B(4)
1	27.44	.120	.2756E+02	.4146E-02		
2	27.55	.006	.2756E+02	.8494E-05		
3	27.67	-.075	.2755E+02	.5850E-03		
4	27.78	-.057	.2753E+02	.1882E-02		
5	27.88	-.069	.2751E+02	.2492E-02		
6	27.99	.109	.2747E+02	.3844E-02		
7	28.10	.127	.2744E+02	.4442E-02		
8	28.20	.086	.2743E+02	.4546E-02		
9	28.30	-.168	.2747E+02	.3930E-02		
10	28.40	-.328	.2752E+02	.3288E-02		
11	28.49	-.302	.2754E+02	.3009E-02		
12	28.59	-.182	.2753E+02	.3061E-02		
13	28.68	-.121	.2752E+02	.3201E-02		
14	28.77	-.059	.2750E+02	.3383E-02		
15	28.86	.007	.2748E+02	.3585E-02		
16	28.95	-.016	.2746E+02	.3714E-02		
17	29.03	-.006	.2745E+02	.3819E-02		
18	29.12	-.027	.2744E+02	.3885E-02		
19	29.20	-.202	.2745E+02	.3825E-02		
20	29.28	-.282	.2746E+02	.3739E-02		
21	29.36	-.172	.2746E+02	.3735E-02		
22	29.43	-.092	.2746E+02	.3774E-02		
23	29.51	-.041	.2745E+02	.3830E-02		
24	29.58	-.051	.2744E+02	.3872E-02		
25	29.65	-.183	.2744E+02	.3857E-02		
26	29.72	-.282	.2745E+02	.3812E-02		
27	29.78	-.286	.2746E+02	.3775E-02		
28	29.85	-.381	.2747E+02	.3718E-02		
29	29.91	-.062	.2746E+02	.3765E-02		
30	29.97	.267	.2743E+02	.3895E-02		
31	30.03	.370	.2740E+02	.4033E-02		
32	30.08	.119	.2739E+02	.4088E-02		
33	30.14	-.097	.2739E+02	.4086E-02		
34	30.19	-.279	.2740E+02	.4044E-02		
35	30.24	-.006	.2740E+02	.4065E-02		
36	30.29	.138	.2738E+02	.4112E-02		
37	30.34	.122	.2738E+02	.4149E-02		
38	30.38	.077	.2737E+02	.4174E-02		
39	30.43	.096	.2736E+02	.4199E-02		
40	30.47	.024	.2736E+02	.4209E-02		
41	30.51	.047	.2736E+02	.4222E-02		
42	30.54	.134	.2735E+02	.4246E-02		
43	30.58	.098	.2734E+02	.4262E-02		
44	30.61	.065	.2734E+02	.4272E-02		
45	30.64	.033	.2734E+02	.4276E-02		
46	30.67	.004	.2734E+02	.4276E-02		
47	30.70	.007	.2734E+02	.4277E-02		
48	30.73	.043	.2734E+02	.4281E-02		
49	30.75	.081	.2734E+02	.4290E-02		
50	30.77	.246	.2733E+02	.4315E-02		
51	30.79	.226	.2732E+02	.4335E-02		
52	30.81	.052	.2732E+02	.4337E-02		
53	30.83	-.151	.2733E+02	.4319E-02		
54	30.84	-.289	.2734E+02	.4289E-02		
55	30.85	-.271	.2735E+02	.4264E-02		
56	30.86	-.033	.2735E+02	.4261E-02		
57	30.87	.083	.2734E+02	.4267E-02		
58	30.88	-.017	.2734E+02	.4266E-02		
59	30.88	-.270	.2735E+02	.4244E-02		
60	30.89	-.273	.2736E+02	.4225E-02		
61	30.89	-.274	.2736E+02	.4206E-02		
62	30.89	-.211	.2737E+02	.4193E-02		
63	30.88	-.177	.2737E+02	.4183E-02		
64	30.88	-.141	.2737E+02	.4177E-02		
65	30.87	-.041	.2737E+02	.4177E-02		
66	30.86	-.033	.2737E+02	.4177E-02		
67	30.85	-.053	.2737E+02	.4177E-02		
68	30.84	-.196	.2738E+02	.4168E-02		
69	30.83	-.151	.2738E+02	.4163E-02		
70	30.81	-.041	.2738E+02	.4163E-02		
71	30.79	.101	.2738E+02	.4170E-02		

72	30.77	.277	.2737E+02	.4185E-02	
73	30.75	.299	.2737E+02	.4200E-02	
74	30.73	.136	.2737E+02	.4207E-02	
75	30.70	.007	.2736E+02	.4208E-02	
76	30.67	-.059	.2737E+02	.4207E-02	
77	30.64	.033	.2736E+02	.4209E-02	
78	30.61	.127	.2736E+02	.4214E-02	
79	30.58	.161	.2736E+02	.4220E-02	
80	30.54	.103	.2736E+02	.4223E-02	
81	30.51	.078	.2736E+02	.4226E-02	
82	30.47	-.007	.2736E+02	.4226E-02	
83	30.43	-.028	.2736E+02	.4226E-02	
84	30.38	.139	.2736E+02	.4229E-02	
85	30.34	.215	.2736E+02	.4233E-02	
86	30.29	.200	.2736E+02	.4236E-02	
87	30.24	.249	.2736E+02	.4239E-02	
88	30.19	-.053	.2736E+02	.4239E-02	
89	30.14	-.227	.2736E+02	.4238E-02	
90	30.08	-.107	.2736E+02	.4237E-02	
91	30.03	.079	.2736E+02	.4237E-02	
92	29.97	.137	.2736E+02	.4237E-02	
93	29.91	.036	.2736E+02	.4237E-02	
94	29.85	-.032	.2736E+02	.4237E-02	
95	29.78	.000	.2736E+02	.4237E-02	
96	29.72	.034	.2737E+02	.4236E-02	
97	29.65	.069	.2737E+02	.4234E-02	
98	29.58	.139	.2737E+02	.4231E-02	
99	29.51	.244	.2738E+02	.4224E-02	
100	29.43	.253	.2739E+02	.4217E-02	
101	29.36	.263	.2739E+02	.4208E-02	
102	29.28	.310	.2740E+02	.4197E-02	
103	29.20	.296	.2741E+02	.4186E-02	
104	29.12	.253	.2742E+02	.4175E-02	
105	29.03	.181	.2743E+02	.4167E-02	
106	28.95	.142	.2743E+02	.4160E-02	
107	28.86	.007	.2744E+02	.4160E-02	
108	28.77	-.120	.2743E+02	.4166E-02	
109	28.68	-.305	.2742E+02	.4183E-02	
110	28.59	-.335	.2740E+02	.4201E-02	
111	28.49	-.271	.2739E+02	.4216E-02	
112	28.40	-.113	.2739E+02	.4221E-02	
113	28.30	-.168	.2738E+02	.4230E-02	
114	28.20	-.159	.2738E+02	.4237E-02	
115	28.10	-.121	.2737E+02	.4242E-02	
116	27.99	.048	.2738E+02	.4235E-02	
117	27.88	.215	.2739E+02	.4217E-02	
118	27.78	.354	.2741E+02	.4189E-02	
119	27.67	.309	.2743E+02	.4165E-02	
120	27.55	.197	.2744E+02	.4150E-02	
121	27.44	.056	.2744E+02	.4146E-02	
	MAX	NP	INDEX	IP	
	2	2	1	1	
	MAX	NP	INDEX	IP	
	2	2	2	2	
	MAX	H	G	SY	SY
	2	1.000000	.252325E-05	.366704E+01	.366704E+01
		B(1) =	.274399E+02		
		B(2) =	.414588E-02		

P (1, KP)	P (2, KP)	P (3, KP)	P (4, KP)	P (5, KP)
.4758757D-01	-.7150281D-04			
-.7150281D-04	.1300165D-06			
CORRELATION MATRIX				
.1000000E+01				
-.9090278E+00	.1000000E+01			
XTX (I, K), K=1, NP				
.1210000E+03	.6654418E+05			
.6654418E+05	.4428743E+08			
XTY (I), I=1, NP, WHERE Y IS RESID				
-.1530085E-01	-.6287375E+01			
XTY (I), I=1, NP, Y IS Y, NOT RESID				
.5573971E-01	.0000000E+00			
MAX	NP	INDEX	IP	
2	2	2	3	